Three-dimensional optical lithography beyond the diffraction limit

Zur Erlangung des akademischen Grades eines
DOKTORS DER NATURWISSENSCHAFTEN
von der Fakultät für Physik des
Karlsruher Instituts für Technologie (KIT)

genehmigte

Dissertation

von

Dipl.-Phys. Joachim Fischer
aus Achern

Tag der mündlichen Prüfung:	27.4.2012
Referent:	Prof. Dr. Martin Wegener
Korreferent:	Prof. Dr. Kurt Busch

Contents

Publications

Parts of this thesis have already been published in peer-reviewed scientific journals:

- J. Fischer, G. von Freymann, and M. Wegener, "The materials challenge in diffraction-unlimited direct-laser-writing optical lithography," Advanced Materials **22**, 3578–3582 (2010).
- T. Wolf, J. Fischer, M. Wegener, and A. Unterreiner, "Pump–probe spectroscopy on photoinitiators for stimulated-emission-depletion optical lithography," Optics Letters **36**, 3188–3190 (2011).
- J. Fischer, T. Ergin, and M. Wegener, "Three-dimensional polarization-independent visible-frequency carpet invisibility cloak," Optics Letters **36**, 2059–2061 (2011).
- J. Fischer and M. Wegener, "Three-dimensional direct laser writing inspired by stimulated-emission-depletion microscopy," Optical Materials Express **1**, 614–624 (2011).
- J. Fischer and M. Wegener, "Ultrafast polymerization inhibition by stimulated emission depletion for three-dimensional nano lithography," Advanced Materials **24**, OP65–OP69 (2012).
- J. Fischer and M. Wegener, "Three-dimensional optical laser lithography beyond the diffraction limit," Laser & Photonics Reviews (2012). http://dx.doi.org/10.1002/lpor.201100046

Parts of this thesis have been presented at scientific conferences (only own presentations):

- J. Fischer, G. von Freymann, and M. Wegener, "Towards diffraction-unlimited 3D laser lithography," **contributed talk, SPIE Photonics West 2010,** San Francisco, USA, January 2010.
- J. Fischer, G. von Freymann, and M. Wegener, "Towards diffraction-unlimited 3D Direct-Laser-Writing lithography," **invited talk, Micro & Nano Engineering 2010,** Genoa, Italy, September 2010.
- J. Fischer, G. von Freymann, and M. Wegener, "Diffraction-unlimited 3D laser lithography with improved lateral and axial resolution," **contributed talk, SPIE Photonics West 2011,** San Francisco, USA, January 2011.

- J. Fischer, T. Ergin, G. von Freymann, and M. Wegener, "Three-Dimensional Laser Lithography with Conceptually Diffraction-Unlimited Lateral and Axial Resolution," **contributed talk, CLEO 2011,** Baltimore, USA, May 2011.
- T. Ergin, J. Fischer, and M. Wegener, "Three-dimensional invisibility carpet cloak at 700 nm wavelength," **invited talk, CLEO 2011,** Baltimore, USA, May 2011.
- J. Fischer, T. Wolf, A.-N. Unterreiner, and M. Wegener, "Time-resolved experiments on diffraction-unlimited 3D laser lithography," **contributed talk, SPIE Photonics West 2012,** San Francisco, USA, January 2012.

Additional work on related topics has been published in peer-reviewed scientific journals:

- F. Klein, T. Striebel, J. Fischer, Z. Jiang, C. Franz, G. von Freymann, M. Wegener, and M. Bastmeyer, "Elastic Fully Three-dimensional Microstructure Scaffolds for Cell Force Measurements," Advanced Materials **22**, 868–871 (2010).
- M. Thiel, J. Fischer, G. Von Freymann, and M. Wegener, "Direct laser writing of three-dimensional submicron structures using a continuous-wave laser at 532 nm," Applied Physics Letters **97**, 221 102 (2010).
- T. Ergin, J. Fischer, and M. Wegener, "Optical phase cloaking of 700 nm light waves in the far field by a three-dimensional carpet cloak," Physical Review Letters **107**, 173 901 (2011).
- T. Ergin, J. Fischer, and M. Wegener, "Detailed optical characterization of three-dimensional visible-frequency polarization-independent carpet invisibility cloak," Physica B: Condensed Matter (2011).
  http://dx.doi.org/10.1016/j.physb.2011.11.035

Abbreviations

ALD	atomic layer deposition
AOM	acousto-optic modulator
AR	aspect ratio
CCD	charge-coupled device
cw	continuous wave
DETC	7-diethylamino-3-thenoylcoumarin
DLW	direct laser writing
EOM	electro-optic modulator
ESA	excited-state absorption
fcc	face-centered cubic
FIB	focused ion beam
FFT	fast Fourier transform
FTIR	Fourier-transform infrared
FWHM	full width at half maximum
GBA	γ-butyrolactone
ISC	intersystem crossing
ITX	isopropyl thioxanthone
LED	light-emitting diode
MGCB	malachite green carbinol base

MGC-HCl	malachite green carbinol hydrochloride
MPB	"MIT Photonic-Bands" (free software package)
NA	numerical aperture
OD	optical density
OPO	optical parametric oscillator
PETA	pentaerythritol triacrylate
PETTA	pentaerythritol tetraacrylate
RAPID	resolution augmentation through photo-induced deactivation
SE	stimulated emission
SEM	scanning-electron microscope
STED	stimulated-emission depletion
TCSPC	time-correlated single photon counting
TTA	triplet-triplet absorption
UV	ultraviolet
voxel	volume element
1PA	one-photon absorption
2D	two-dimensional
2PA	two-photon absorption
2PII	two-color photo-initiation/inhibition
3D	three-dimensional

1. Introduction

The maturing field of nanotechnology is so wide and multi-faceted that even finding a common definition of this notion seems to be difficult. Among some possible definitions published in the first issue of Nature Nanotechnology [1], I like the one of Prof. Mauro Ferrari best. He states,

> "At the nanoscale there is no difference between chemistry and physics, engineering, mathematics, biology or any subset thereof. An operational definition of nanotechnology involves three ingredients: (1) nanoscale sizes in the device or its crucial components; (2) the man-made nature; and (3) having properties that only arise because of the nanoscopic dimensions."

The term "nanoscale" is commonly used for sizes below 100 nm [1]. For experimentalists, the biggest challenge in nanotechnology is not developing new ideas and designs but bringing these designs to reality by fabricating such man-made nanoscale objects.

While bottom-up approaches based on self-assembly were long expected to eventually prevail over top-down lithography approaches, the latter are still dominant in many important areas such as computer-chip or photonic-circuitry fabrication. However, all top-down nanofabrication methods available today, such as electron-beam lithography, are restricted to planar two-dimensional (2D) structures. A true three-dimensional (3D) nanofabrication method is missing so far. Topographies with varying heights may be accessible *via* so-called gray-tone lithography, but such geometries are commonly not considered to be truly 3D. Current nanofabrication approaches can only enter the third dimension by combining many processing steps to create layer-by-layer objects composed of several two-dimensionally structured layers. These procedures are usually very time-consuming and error-prone which limits the feasible number of layers to typical values on the order of ten. Moreover, the final 3D structures will always exhibit a layered nature. Consequently, the availability of a true 3D nanofabrication method could open new avenues in nanotechnology.

In contrast to planar nanofabrication approaches, 3D direct-laser-writing (DLW) optical lithography allows for the fabrication of arbitrary 3D structures in a single processing step. Like in most optical technologies, the resolution in DLW is limited by diffraction. With minimum lateral (axial) feature sizes around 100 nm (250 nm) and with even larger minimum line spacings, DLW is not a real nanotechnology yet. In order to enable new applications in 3D nanoscience, it is therefore highly desirable to improve the resolution of 3D DLW.

The diffraction limit: The concepts and developments in lithography and microscopy are often closely related and sometimes even interchangeable. Thus, many forms of microscopy have a lithographic counterpart relying on similar principles. Moreover, optical microscopy and optical lithography share a common restriction, namely the diffraction barrier. Ernst Abbe described this problem in his famous resolution formula [2] for the minimum lateral distance a_{xy} between two features that are resolvable with a microscope:

$$a_{xy} = \frac{\lambda}{2\,n \sin\alpha}\,,$$

where λ is the free-space wavelength of light, n is the refractive index of an embedding medium, and α is the maximum half-opening angle collected by the lens. Along these lines, the resolution of a corresponding lithography system is equally limited.

As can be seen in Abbe's formula, increasing the aperture angle α, using immersion media with higher refractive indices n, and decreasing the used wavelength λ will increase the resolution of an optical system. In optical microscopy, when using modern objective lenses and visible light, the Abbe formula returns minimum resolvable distances between 150 nm and 400 nm.

In optical lithography, the industrial demand for ever smaller transistors on computer chips has driven technologies to deep ultraviolet (UV) wavelengths down to $\lambda = 157\,\text{nm}$ and will probably bring them to extreme UV wavelengths around $\lambda = 13.5\,\text{nm}$ in the near future. This ongoing reduction in wavelength comes along with ever increasing challenges for the optical design. On the microscopy side, the Abbe limit is pushed to resolutions below 1 nm by utilizing the even shorter de Broglie wavelength of accelerated electrons instead of electromagnetic radiation.

Could such small wavelengths be used to likewise push the diffraction barrier in 3D DLW down to the nanoscale? Commmonly, visible exposure wavelengths between 500 nm and 800 nm are used in 3D DLW. The use of much shorter wavelengths is not possible while maintaining the 3D capabilities: We will see in Section 2.1.2 that 3D DLW only works at wavelengths where the used photoresist is highly transparent. Unfortunately, all potential photoresist materials will likely absorb UV light to some extent. Regarding accelerated electrons, we have already implied that such beams can indeed be used for nanoscale lithography. Minimum linewidths below 10 nm [3, 4] are accessible – yet only in two dimensions.

Breaking the diffraction limit: Fluorescence microscopy using visible light, is – despite its resolution being inferior to that of electron microscopy – dominating the important field of life sciences. The possibility to place different fluorescent markers within a single cell allows scientists to access detailed structural and functional information from the interior of living matter. Most importantly, optical microscopy can deeply penetrate the sample volume and gather 3D information while electron-beam microscopy can only "scratch the surface".

Given these advantages of optical microscopy, many approaches that can circumvent the diffraction problem and break Abbe's resolution barrier have been developed. In 1994,

Stefan Hell presented a far-field resolution-enhancing approach called stimulated-emission-depletion (STED) microscopy [5]. This method is an extension of confocal laser-scanning fluorescence microscopy that preserves all positive aspects of optical microscopy. Most importantly, the capability for 3D imaging is not affected at all. In STED microscopy, the diffraction barrier has been overcome by a large margin. Record resolutions down to 5.6 nm have been demonstrated using $\lambda = 532\,\text{nm}$ visible light [6].

Breaking the resolution limit in 3D DLW in a similar fashion could bring this technology to the nanoscale and at the same time bring top-down nanofabrication to the third dimension. While STED microscopy has demonstrated up to 40-fold improved resolution, a factor of 2–5 in lithography would already enable various new applications for DLW lithography.

Therefore, the aim of this thesis is to improve the resolution of 3D DLW by translating STED or related concepts from optical microscopy to optical lithography.

Outline of this thesis

In Chapter 2, we will lay out the basic concepts of DLW lithography, introduce a numerical method to calculate focal intensity distributions, and finally build a framework to estimate the resolution limits of common DLW. We will emphasize the difference between "linewidth" and "resolution" in lithography, two terms that are often used in confusing ways.

In Chapter 3, we will give a detailed motivation for the combination of DLW with a STED-like effect and discuss anticipated improvements. We will also describe alternative depletion effects distinct from STED that have been discovered by other groups in parallel to this thesis. We will discuss distinct advantages and disadvantages of all mechanisms.

In Chapter 4, we will describe the experimental methods used. After introducing the experimental setup, a method to characterize and optimize the focal intensity distributions is explained.

In Chapter 5, we will describe the challenges and solutions in finding photoinitiators suitable for STED. Having found two photoresist formulations for STED-like lithography, we will examine the underlying processes by means of pump-probe experiments and time-resolved lithography experiments.

In Chapter 6, we will demonstrate improvements in lateral linewidth, in lateral resolution, in axial lineheight, and in axial resolution using different depletion foci. The presented resolutions exceed the capabilities of common DLW and break the diffraction limit in the lateral as well as in the axial direction for the first time. Finally, we apply the enhanced resolution of our new lithography approach to realize a polarization-independent 3D carpet invisibility cloak operating at visible frequencies. Such a device could neither have been fabricated using common DLW nor (most probably) with any other available micro-/nanofabrication approach.

We will conclude on the presented work in Chapter 7 and give a brief outlook on future challenges and possibilities.

2. Fundamentals

The scope of this thesis is to combine 3D DLW optical lithography with the idea of STED optical microscopy to improve the attainable resolution of the former. In this chapter, we will review the fundamentals of conventional DLW. We will also discuss the limitations of diffraction-limited optical lithography in general and the resolution of DLW in particular. The notions and concepts presented in this chapter are paramount for the understanding of the new improved approach to be introduced in Chapter 3.

2.1. Direct-laser-writing (DLW) optical lithography

In a nutshell, DLW optical lithography [7–14] is a technique that allows for the fabrication of nearly arbitrary 3D polymer structures in a single processing step. Like guiding a paintbrush over a piece of paper, a focused laser spot is moved along pre-programmed trajectories in three dimensions within a photoresist volume. For a common negative-tone photoresist, unexposed regions are washed out while exposed regions withstand a solvent wash. In the end, a freestanding 3D structure resembling the written trajectories remains.

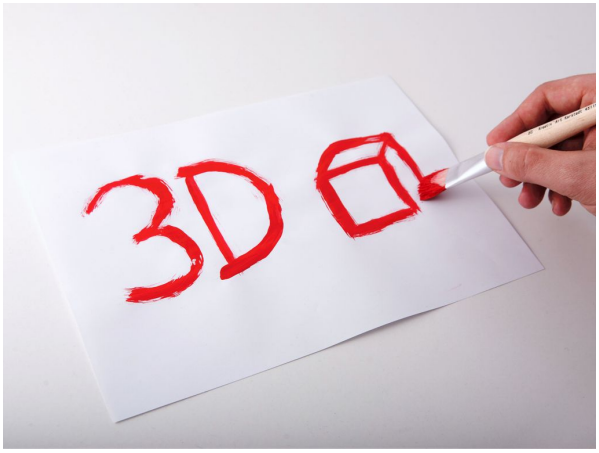

Other nano-fabrication approaches like electron beam lithography are usually restricted to planar lithography. Thin layers of resists can be structured at very high resolution. However, 3D structures can only be achieved by either stacking several layers on top of each other [20] or by performing alternating lithography, evaporation, and planarization steps [21]. The attainable number of layers is usually around ten and limited by the reproducibility of the alignment and by the time needed for each fabrication step.

In sharp contrast, a nearly unlimited number of shapes is attainable in 3D DLW with reasonable fabrication time and effort. The minimum feature sizes and spatial periods, however, are governed by the shape of the focus and the photoresist properties. Usually, lateral (axial) feature sizes down to 100 nm (250 nm) are feasible. This lateral extent is roughly ten times larger than that attainable in electron-beam lithography [3, 4].

The 3D structures fabricated with DLW can be very complex and can even contain free-form surfaces. Some examples for 3D structures written with DLW are depicted in Fig. 2.1.

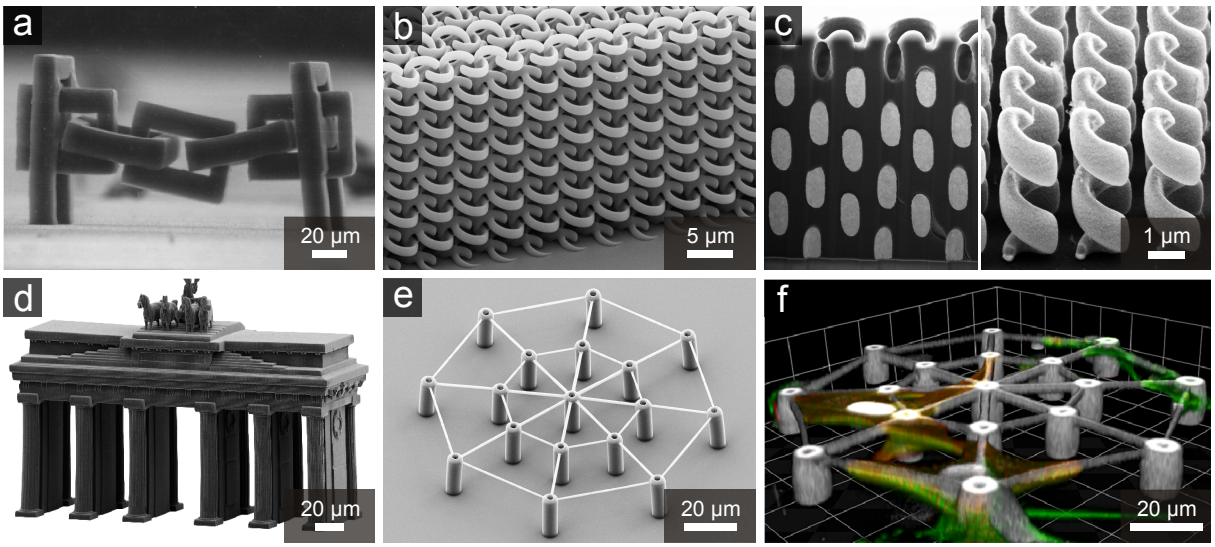

Figure 2.1.: (a–e) Scanning-electron micrographs of exemplary structures fabricated *via* 3D DLW. (a) Intermeshing links of a micro chain fabricated *via* 3D DLW. Taken from Ref. [15]. (b) Bi-chiral photonic crystal consisting of intermeshing helices along all three cartesian axes. Taken from Ref. [16]. (c) Helices written in a positive-tone photoresist and filled with gold. Left side: Focused-ion-beam cut of the polymer-gold composite. Right side: Free standing gold helices with the surrounding polymer removed. Taken from Ref. [17]. (d) Model of the Brandenburg Gate. (The substrate background has been removed from the image.) A Courtesy of Nanoscribe GmbH [18]. (e) A 3D polymer structure designed for biological cell-culture experiments. (f) Confocal fluorescence micrograph of a similar structure occupied by a beating chicken heart cell. Previously published in Ref. [19].

Even intermeshing structures like the links of a chain can be fabricated [15] because the laser can be focused through material that has already been exposed (see Fig. 2.1 (a)).

The materials that can be directly patterned *via* DLW are rather limited and include mainly polymers and few other materials like, *e.g.*, chalcogenide glasses [22, 23]. However, the polymer structures can be used as templates to be coated with other materials like, *e.g.*, silver [24, 25]. Using so-called "double-inversion" [26] or "single-inversion" [27, 28] processes, the template structure or its inverse can be transferred to materials like silica glass [26–28], silicon [26–28], zinc oxide [29], or even gold [17].

DLW has emerged from the nanophotonics community and has found various applications therein, like the fabrication 3D photonic crystals [7, 8, 10, 30], chiral optical materials [16, 17, 31, 32], 3D photonic quasi-crystals [27, 33], 3D photonic metamaterials [17, 24, 34], 3D gradient-index devices for transformation optics [35], microdisk resonators [36], structures including optical emitters [36, 37], and 3D chip-to-chip optical interconnects [38, 39]. Not only nanophotonics, but many other scientific fields can profit from tailored 3D structures on the micro- to nanoscale. For example, mechanical metamaterials with tailored mechanical properties not found in nature can be fabricated with direct laser writing [40, 41]. Special 3D photonic crystals may serve as particle accelerators driven

by optical electric fields [42]. Three-dimensional scaffolds for cell-culture experiments are promising candidates for next-generation "designer Petri dishes" [19, 43] (see, *e.g.*, Fig. 2.1 (e, f)). DLW using biodegradable polymers has been demonstrated [44] and can enable 3D micro-structured scaffolds for tissue engineering. Moreover, the imitation and modification of surface microstructures found in nature (like, *e.g.*, the feet of a gecko [45]) is possible with 3D DLW.

Especially optimizations and other systematic parameter variations are very convenient in DLW, as there is no need for the design and fabrication of masks or masters, which would come along with a long process chain and possibly with the dependence on external facilities. In 3D DLW, a design can be changed on the computer and be fabricated one minute later. This leads to extremely short iteration cycles.

2.1.1. DLW workflow and exposure mechanism

Let us first get a quick impression of the workflow in DLW lithography. The common DLW workflow is illustrated schematically in Fig. 2.2.

First, a photoresist is placed on a glass substrate *via* drop casting or spin coating. Usually, a microscope coverslip serves as substrate. A focused laser beam is used to locally expose the photoresist volume. The exposure occurs only within a small three-dimensionally confined volume around the geometrical focus. We will refer to this exposed volume element as a "voxel".[1] By translating the sample with respect to the focus, 3D exposure patterns can be formed out of these voxels (Fig. 2.2 (b, c)) within a single processing step. For a so-called "negative-tone" photoresist, the exposed regions undergo a chemical reaction that increases their resistance against solvents.

When the exposure is completed, the sample is put in a solvent bath during the development step. Unexposed regions are dissolved while exposed parts withstand the solvent. After removing the solvent *via* blow-drying with nitrogen gas, a free-standing polymer structure remains on the substrate (Fig. 2.2 (d)). Fig. 2.1 (e) shows a SEM of the final developed structure corresponding to the cartoon in Fig. 2.2.

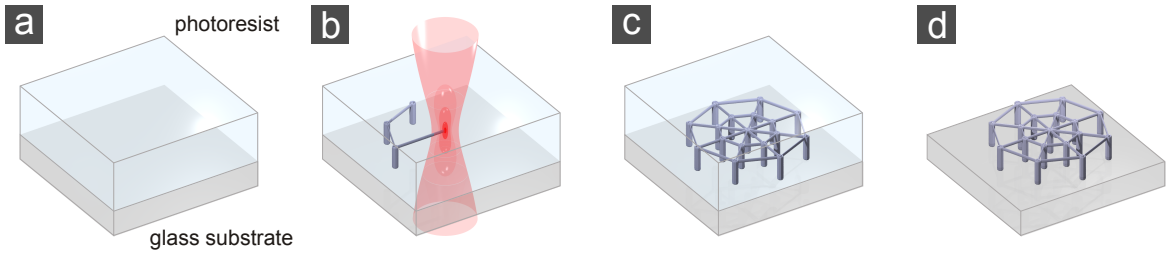

Figure 2.2.: Illustration of the workflow in DLW optical lithography (not to scale). (a) Photoresist on glass substrate. (b) Exposure with a focused laser beam. (c) Exposed structure embedded in unexposed photoresist. (d) Free-standing structure after removal of the unexposed resist. Previously published in Ref. [19].

[1] The word "voxel" is chosen in analogy to the picture element commonly referred to as pixel.

The exposure mechanisms and the involved chemical reactions depend on the resist system used. A commonly used class of photoresists is based on free radical polymerization.[2] Such photoresists typically consist of at least two components: A substance to be cross-linked (*e.g.*, a monomer) and a photoinitiator. The former is usually transparent at relevant optical frequencies whereas the latter is supposed to absorb light and initiate a chemical reaction.

After photoinitiator molecules are excited *via* light absorption, a certain fraction of the molecules will generate radicals (*e.g.*, *via* cleavage or charge transfer to other molecules). These radicals initiate a polymerization reaction, which proceeds in acquiring monomer molecules until the propagating radical chains are terminated or until no monomer is left. Monomers with multiple polymerizable groups (*e.g.*, multiple acryloyl groups) can not only form chains but also cross-linked polymer networks. When the molecular weight of this network has reached a certain threshold value, it becomes insoluble.

As the dynamics of the reaction described above can be very complex in detail, the underlying mechanism is often neglected and it is assumed that the photoresist will withstand the solvent wash in case the local exposure dose D has exceeded a certain threshold value D_{th}. We will refer to this model as the "threshold model".

However, defining a local exposure dose is non-trivial as well. We will usually assume that the local exposure dose is simply proportional to the number of radicals that have been generated within a volume element. This number is proportional to the number of photoinitiator molecules excited within the same volume element and to the number of absorbed photons. Moreover, we will assume that exposure doses of sequential exposures do completely add up. This means, a photoresist "remembers" all below-threshold exposures. If the accumulated exposure dose finally exceeds the threshold dose, the resist will solidify.

2.1.2. Two-photon absorption for three-dimensional exposure

Three-dimensional DLW is usually based on two-photon absorption (2PA). This process demands for high peak intensities and therefore rather expensive pulsed laser sources. Let us quickly explain why the use of 2PA is necessary and why one-photon absorption (1PA) can in general not be used for arbitrary 3D structuring.

In everyday life, light is nearly exclusively absorbed *via* 1PA. This means that, *e.g.*, a single atom or molecule undergoes an electronic transition induced by the absorption of a single photon. The probability of the absorption process is proportional to the local light intensity at the absorber. Loosely speaking, the 1PA probability is proportional to the probability of finding a photon at the absorber's position, hence, proportional to the photon density, and, therefore, to the light intensity.

As usual photoinitiator molecules have electric-dipole-allowed transitions, it is actually not the light intensity I (*i.e.*, the time average of the modulus of the poynting vector

[2] Other prominent 3D-DLW photoresists are SU-8 (a negative-tone photoresist based on cationic polymerization) and the positive-tone photoresist AZ 9260.

$\langle|\vec{S}|\rangle = \langle|\vec{E} \times \vec{H}|\rangle = I$) but the electric field $\vec{E}$ alone that is relevant for the absorption. More specifically, the absorption probability is $\propto |\vec{E}|^2$ and the exposure dose is $D \propto |\vec{E}|^2\, T$, where T is a fixed exposure time. For the sake of simplicity, we will often use the inaccurate term intensity instead of $|\vec{E}|^2$, as these quantities are usually proportional to each other in good approximation (see Section 2.2.2 for a counterexample). We can neglect the orientation of the electric field relative to the transition dipole of the molecules, assuming the molecule axes to be randomly distributed within the ensemble.

In case a photoresist absorbs light *via* 1PA, the beam is indeed significantly attenuated on its way towards the focal point. For a plane wave, the attenuation caused by 1PA follows

$$\frac{\mathrm{d}I}{\mathrm{d}z} = -\sigma_{1\mathrm{PA}} \cdot N \cdot I(z) \tag{2.1}$$

and leads to the Beer-Lambert law

$$I(z) = I_0 \cdot \mathrm{e}^{-\sigma_{1\mathrm{PA}} N z}\,, \tag{2.2}$$

where I is the light intensity, z is the spatial coordinate along the direction of light propagation, $\sigma_{1\mathrm{PA}}$ is the linear absorption cross-section of the absorbing photoinitiator molecule, and N is the number of photoinitiator molecules per unit volume. The situation for a Gaussian beam profile impinging from bottom up is illustrated in Fig. 2.3 (a). The intensity integrated over the lateral coordinates x and y (right sub-panel of Fig. 2.3 (a)) shows that most of the light is absorbed before the focal volume is reached. Clearly, this situation is inconvenient for three-dimensional exposure.[3]

To get rid of this intensity gradient, one will likely choose the concentration of the photoinitiator (and hence, the resist's optical density) to be very low, at the expense of the photoresist's sensitivity. When focusing a laser beam into such a photoresist (see Fig. 2.3 (b)), the light deeply penetrates the sample. However, the light is not only absorbed inside the focal volume, but also within the complete laser cone. Clearly, the light intensity is highest within the focus and lower within the cone. The number of absorbed photons per volume is proportional to these intensity values. However, if we calculate the number of photons absorbed within a thin z-slice of this cone (*i.e.*, integrate the intensity over x and y), we see that the this quantity is independent of z (Fig. 2.3 (b), right plot). This can immediately be understood, as $\int \mathrm{d}x\, \mathrm{d}y\, I(x, y, z) = P(z)$, where P is the power transmitted in z-direction, which is supposed to be z-independent due to the negligible absorbance and due to energy conservation.

The fact that the number of photons absorbed per z-slice is the same for all z-positions is no issue for the exposure of a single voxel. The exposure dose per volume is highest within the focal volume. If the photoresist exhibits a threshold behavior, the focal volume can be effectively exposed while the remaining cone stays effectively unexposed (because the exposure dose is below the threshold value). After development, a three-dimensionally confined polymer volume would result. However, the situation is different if the exposure

[3] Consider a numerical example: A photoresist composition containing a typical concentration (0.05 mol/L) of a common photoinitiator (extinction coefficient $100\,000\,\mathrm{L\,mol^{-1}\,cm^{-1}}$) attenuates an incoming beam down to 10% intensity within 2 µm pathlength.

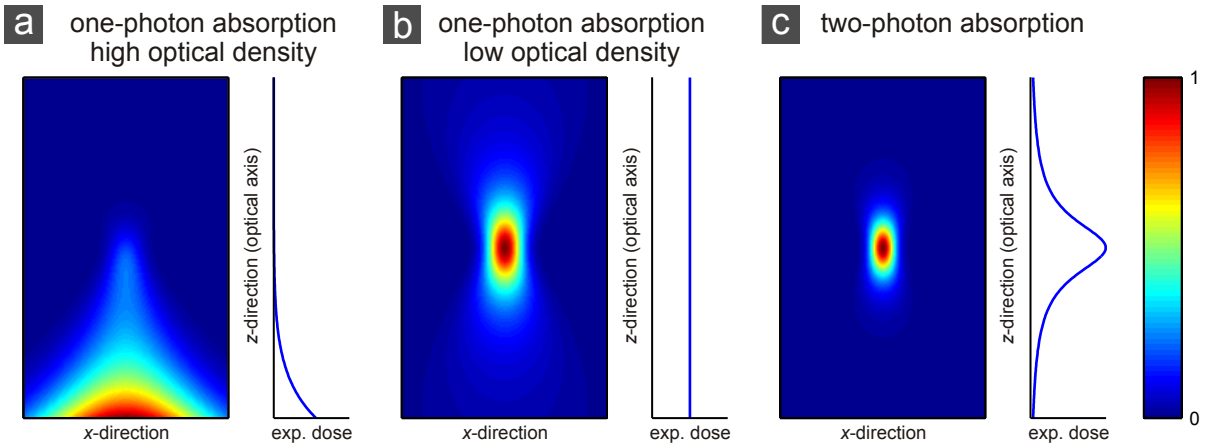

Figure 2.3.: Illustration of the different exposure dose distributions for one-photon absorption (1PA) and two-photon absorption (2PA) when focusing a Gaussian beam from below into a photoresist volume. (a) Strongly absorbing photoresist attenuating the incoming beam *via* 1PA. The normalized intensity is plotted. (b) Weakly absorbing photoresist where the beam can penetrate the resist volume and is absorbed at all z-positions *via* 1PA. Again, the intensity is plotted. (c) Photoresist absorbing the beam *via* 2PA. The squared intensity (which is proportional to the 2PA probability) is plotted. The beam can easily penetrate the volume and the absorption is confined along z-direction. The right sub-panels show line plots corresponding to the exposure dose integrated over x and y.

of a whole plane is aimed for. In this case, one will raster scan the exposure volume within the anticipated 2D plane. This raster scanning leads to an accumulation of the number of absorbed photons above and below the focal plane. If we assume the plane's lateral extent to be very large and the raster pitch to be very small, we can account for the 2D raster scanning by integrating over x and y. Again, we end up with an exposure dose that is independent of the z-position. Hence, after development, we would expect to see a block of polymer where only a plane was desired. Consequently, such a 1PA-approach is not suitable for arbitrary 3D structuring.

In contrast, two-photon absorption is a non-linear optical process where two photons are absorbed simultaneously to drive an electronic transition of a single absorber (*e.g.*, a photoinitiator molecule). As two photons are needed for this process, the probability of the absorption now scales with the squared intensity. Loosely speaking, the probability for 2PA is proportional to the probability of finding a first photon ($P_{1\mathrm{st}} \propto I$) and then finding a second photon ($P_{2\mathrm{nd}} \propto I$) at the absorbers position, hence, $P = P_{1\mathrm{st}} \cdot P_{2\mathrm{nd}} \propto I^2$. For a plane wave and in absence of 1PA, the attenuation caused by 2PA follows

$$\frac{\mathrm{d}I}{\mathrm{d}z} = -\sigma_{2\mathrm{PA}} \cdot N \cdot I(z)^2 \,, \tag{2.3}$$

where $\sigma_{2\mathrm{PA}}$ is the molecular 2PA cross-section. We will see that this non-linearity is crucial for achieving arbitrary 3D structures when assuming an accumulating exposure dose.

The values of this cross-section are usually very small. As 2PA is very improbable, it can only be utilized at optical frequencies where the 1PA cross-section vanishes. Otherwise,

1PA would dominate over 2PA. This situation is usually given when the fundamental electronic transition of a molecule requires an energy higher than that of a single photon but smaller than the combined energy of two photons. Due to the small cross-sections, negligible attenuation of the beam is expected. To drive efficient 2PA, however, high field intensities are required, so that the correspondingly high photon flux density can compensate for the small 2PA cross-sections. This can be achieved by using femtosecond laser pulses with high peak powers combined with tight focusing of the laser beam. Under these conditions, efficient 2PA occurs within the focal volume while the adjacent regions remain effectively unexposed: Due to the quadratic dependence on the light intensity, the absorption probability above and below the focal plane decreases rapidly.

Figure 2.3 (c) illustrates a beam that is exclusively absorbed *via* 2PA. In this panel, the squared intensity is plotted as a measure of the exposure dose ($D \propto |\vec{E}|^4\, T \approx I^2\, T$). Note that this distribution is somewhat tighter than the distribution in (b) due to the squaring. Moreover, the exposure dose integrated over x and y (which is $\propto \int \mathrm{d}x\, \mathrm{d}y\, I(x,y,z)^2 \neq \text{const}$) shows a clear confinement around the z-position of the focus. Consequently, unlike for 1PA, exposing a plane parallel to the substrate surface with 2PA is possible without losing the confinement in z-direction.

Finally, we can conclude that non-linearity is not just beneficial but paramount to access 3D geometries. Utilizing 2PA as non-linear process is very convenient. It should be noted that it is also possible to achieve simple 3D geometries with linear 1PA when the photoresist offers a special chemical non-linearity [46]. If the photoresist after some time tends to "forget" any exposures that did not exceed the polymerization threshold (*e.g.*, due to diffusion exchange of the insufficiently converted monomer) the accumulation of the exposure dose is less pronounced. In this case, integrating over x and y is not adequate to describe the accumulation and 3D capability cannot be ruled out by the above reasoning. However, to the best of our knowledge, no sophisticated 3D structures have yet been achieved using 1PA.

2.2. Theory of the focus shapes

Like the paint brushes in painting, the focal intensity distribution is of critical importance in DLW. Before we can predict the attainable resolution in DLW we need to gather detailed knowledge about the shape of the writing spot used. This information is accessible through numerical calculations or through direct experimental measurements. The numerical method will be used throughout the remainder of this thesis to predict the resolution in regular DLW and to design phase masks for the depletion patterns needed for STED-inspired lithography.

As a rule of thumb, the lateral extent of the focal intensity distribution scales with λ/NA, where λ is the vacuum wavelength of the used laser light, $\mathrm{NA} = n \sin\alpha$ is the numerical aperture, n is the refractive index of the immersion medium or the photoresist, and α is the maximum angle towards the optical axis of the focused rays within the respective medium. Consequently, for very tight focusing, objective lenses supporting large opening angles α and large refractive indices n are necessary. Numerical apertures of $\mathrm{NA} = 1.4$ are very common in DLW and also used throughout this work. Nowadays, objective lenses with even higher numerical apertures such as $\mathrm{NA} = 1.57$ are commercially available (*e.g.*, ZEISS Plan-Apochromat $100\times/\,1.57\,\mathrm{NA}$). Such objectives come along with significant drawbacks like, *e.g.*, very high investment costs, the need for high-index immersion fluids, and small working distances. Furthermore, the photoresist refractive-index n (usually $n \approx 1.52$) sets an upper bound for the applicable NA: In case $\mathrm{NA} > n$ holds, the outermost rays of the laser cone will not even propagate to the focus but undergo total internal reflection at the interfaces from the immersion medium or substrate (with $n > \mathrm{NA}$) to the photoresist (with $n < \mathrm{NA}$), leading to an effective decrease in NA.

2.2.1. Numerical calculation of the vectorial field distribution in the focus

When focusing a laser beam under large opening angles, the focal intensity distribution significantly deviates from simple analytic forms like the so-called Gaussian beam. In this case, the focus formation can no longer be described by a scalar formalism, since the polarization of light has to be considered. The resulting focal intensity distributions are commonly calculated numerically. In our implementation, we follow the work of A. van de Nes *et al.* [47]. This method is based on the diffraction integrals by Richards and Wolf [48, 49] and allows to account for several interfaces between the objective lens and the focus. In this way, the different refractive indices of glass substrate and photoresist can be considered and the effect of resulting aberrations can be predicted. Moreover, this method allows for the description of the focus of an arbitrary laser beam. In particular, arbitrary

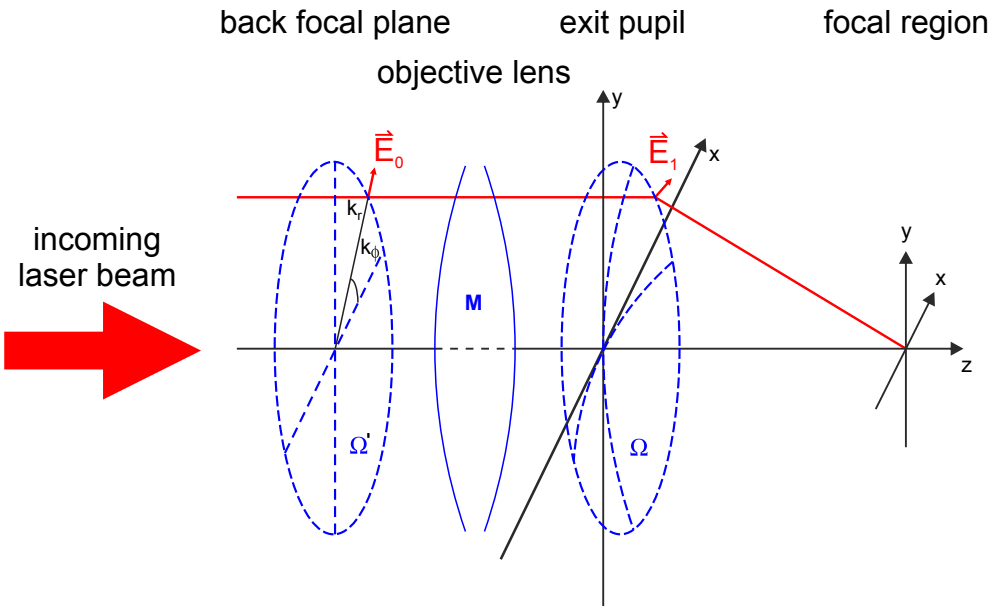

Figure 2.4.: Schematic illustration of an imaging system, representing the microscope objective lens used in DLW to focus the writing laser beam. An incoming laser beam is described by its complex electric field distribution $\vec{E}_0(k_r, k_\phi)$ on the back focal plane Ω'. The operator $\mathbf{M}$ corresponds to the objective lens and maps the incoming fields to the outgoing electric field $\vec{E}_1$ on the exit pupil Ω. Substrate, photoresist, and the corresponding interfaces are not depicted for simplicity. Adapted from Ref. [47].

amplitude, phase, and polarization distributions of the electric field can be specified at the objective's back focal plane. Consequently, focus shaping with phase masks or amplitude masks can easily be explored and optimized.

The approach for the calculation of the electric field inside the focal region is illustrated in Fig. 2.4. First, the spatial electric-field distribution $\vec{E}_0(k_r, k_\phi)$ at the back focal plane Ω' of the objective lens and the vacuum wavelength of the light source used is defined. This distribution $\vec{E}_0(k_r, k_\phi)$ is the spatial profile of the incoming laser beam to be focused. For the beam profile, k_r and k_ϕ are lateral spatial polar coordinates on Ω'. The coordinates x, y, and z are later used within the focal volume. The quantity $\vec{E}_0(k_r, k_\phi)$ is defined as the complex vectorial amplitude of the oscillating electric field $\vec{E}_0(k_r, k_\phi, t) = \mathrm{Re}[\vec{E}_0(k_r, k_\phi) \cdot \mathrm{e}^{-i\omega t}]$, where ω is the angular frequency of the electric field corresponding to the chosen vacuum wavelength.

Next, an operator $\mathbf{M}$ describes the objective lens and maps the field distribution from Ω' onto a spherical shell Ω yielding $\vec{E}_1(k_r, k_\phi) = \mathbf{M}\vec{E}_0(k_r, k_\phi)$. The center of this sphere is the geometrical focus. In absence of material interfaces, this operator $\mathbf{M}$ is a simple 3×3 matrix depending on k_r and k_ϕ, where the three components correspond to the electric field components of $\vec{E}_0(k_r, k_\phi)$ and $\vec{E}_1(k_r, k_\phi)$. This operation simply rotates the electric field vectors as expected for the focusing element. For example, while the electric-field vectors $\vec{E}_0$ at the back focal plane are usually purely lateral (*e.g.*, for an impinging plane

wave), the rotated electric-field vectors $\vec{E}_1$ can have non-zero z-components (see Fig. 2.4, rotated components of $\vec{E}_1$).

To obtain the focal field distribution, the values of $\vec{E}_1$ on Ω are now used as amplitudes of plane waves with wave vectors $\vec{k}$. Now, k_r and k_ϕ, which were used as spatial coordinates on Ω' are reinterpreted as lateral wave-vectors components. The Cartesian wave-vector components k_x and k_y on the sample side are derived from the given k_r and k_ϕ. Furthermore, k_z is given by $k_z(k_x, k_y) = \sqrt{k^2 - k_r^2} = \sqrt{k^2 - k_x^2 - k_y^2}$ with $k = |\vec{k}| = n \cdot k_0 = n \cdot \frac{2\pi}{\lambda}$. Here, n is the refractive index of the embedding medium and λ is the vacuum wavelength of light. All these $\vec{k}$-vectors point from their origin on Ω towards the geometrical focus, where the corresponding plane waves will then superimpose. If the incoming laser beam has a spatially constant phase ($\vec{E}_1(k_x, k_y) = |\vec{E}_1(k_x, k_y)| \exp(i \cdot \text{const})$), the plane waves superimpose in phase at the geometrical focus.

The electric field near the focus is then given by

$$\vec{E}(\vec{r}) = \frac{-iR}{2\pi} \iint_\Omega \frac{\vec{E}_1(k_x, k_y)}{\sqrt{k_z\, k}}\, \mathrm{e}^{i\vec{k}\vec{r}}\, \mathrm{d}k_x\, \mathrm{d}k_y\,, \tag{2.4}$$

where $\vec{r} = (x,\, y,\, z)$ is the position vector relative to the geometrical focus [49].

For the numerical implementation it is convenient to interpret the integration over $\mathrm{d}k_x$ and $\mathrm{d}k_y$ as inverse Fourier transform and use the fast Fourier transform (FFT) algorithm for the evaluation:

$$\vec{E}(\vec{r}) \propto \mathrm{FFT}^{-1}\left[\frac{\mathbf{M}\vec{E}_0(k_x, k_y)}{\sqrt{k_z}}\, \mathrm{e}^{ik_z z}\right]. \tag{2.5}$$

While a conventional numerical integration would have to be performed once for each point within the three-dimensional focus volume, a single FFT is performed on an entire x-y-plane, such that only one FFT per z-coordinate is necessary. Using a standard desktop PC and for simple illumination geometries (*e.g.*, a Gaussian beam), the FFT result for the complete focal volume is evaluated within seconds while point-wise numerical integration can take hours.

Up to now, the matrix $\mathbf{M}$ only describes the rotation and mixing of the electric-field vectors due to the focusing by the objective lens. This matrix can be extended in a straight-forward fashion to also account for different media with different refractive indices along the optical axis [47]. Now, there is such a matrix for every medium m that we call $\mathbf{M}_m$ which accounts for the lens as well as all relevant interfaces. To also account for reflections at interfaces beyond the position of interest (*i.e.*, with z-values larger than that of the point to be calculated), we also have to take into account backwards traveling waves. Consequently, there is a matrix $\mathbf{M}_m^+$ for the forward propagation waves and a matrix $\mathbf{M}_m^-$ for the backward propagating waves within medium m. For the field distribution $\vec{E}_m(\vec{r})$, where $\vec{r}$ is inside medium m, this leads to the expression

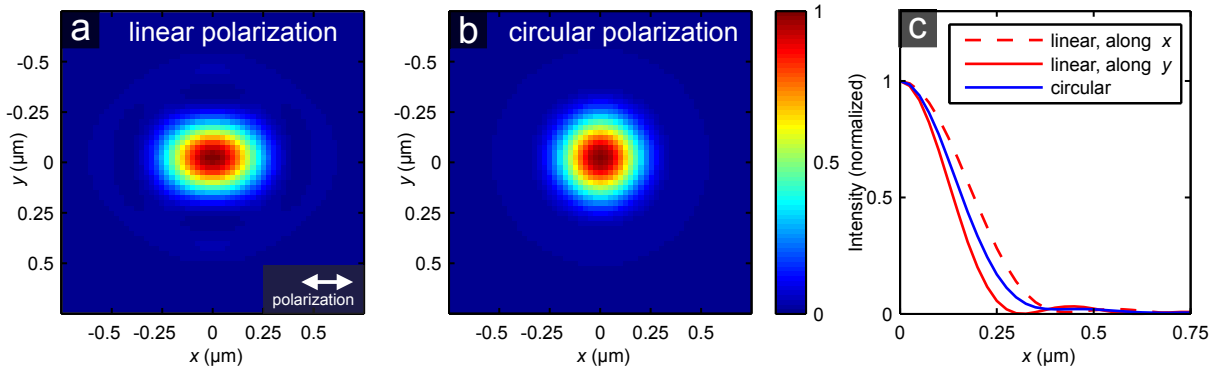

Figure 2.5.: (a) Calculated distribution of $\langle|\vec{E}|^2\rangle$ in the focal plane when focusing a linear polarized beam. (b) Same as (a) but for a circular polarized beam. (c) Line scans through the geometrical focus along x- and y-axis for both polarizations. Parameters used for all panels: $\lambda = 800\,\mathrm{nm}$, NA $= 1.4$, $n = 1.52$.

$$\vec{E}_m(\vec{r}) = -\frac{iR}{2\pi}\iint_\Omega \frac{e^{i(k_x x + k_y y)}}{\sqrt{k_{z1}\,k_1}}\left(e^{ik_{zm}z}\mathbf{M}_m^+ + e^{-ik_{zm}z}\mathbf{M}_m^-\right)\vec{E}_0(k_x,k_y)\mathrm{d}k_x\mathrm{d}k_y\,, \tag{2.6}$$

where k_m and k_{zm} correspond to the quantities k and k_z for the current medium m. Accordingly, k_1 and k_{z1} correspond to k and k_z for the medium $m = 1$.

For further details on the explicit form of $\mathbf{M}_m^+$ and $\mathbf{M}_m^-$ see Ref. [47]. Through these matrices, the fields inside any medium can be directly computed without the need to compute the complete field propagation from the lens to the point of interest.

2.2.2. Basic examples: Polarization and beam diameter

Before we begin with resolution considerations and think about shaping complex donut modes, let us "sharpen our pencils" and calculate the shape of a common writing focus in conventional DLW. For the experimental implementation, the experimenter has to decide on two basic parameters of the writing beam: the polarization state and the beam diameter. As a finger exercise, we examine these parameters using the code described above.

Beam polarization:

It has already been mentioned that for focusing laser beams with high-numerical-aperture objective-lenses the field distribution is affected by the polarization state used. All common laser sources with polarized output deliver light of one linear polarization. This first polarization state can be easily converted into circular polarization using an appropriate quarter-wave plate inserted into the laser beam. A third possible polarization state is radial polarization [50–52]. This polarization state leads to a very sharp laterally confined focus and has already been applied to DLW [53]. However, the preparation of this

polarization state (out of a linearly polarized beam) is rather complicated and involves holograms, non-commercial segmented wave plates or interferometers [51]. Therefore, we will restrict our considerations to linear and circular polarization here.

When focusing a linearly polarized beam, the quantities $\langle|\vec{E}|^2\rangle$, $\langle|\vec{B}|^2\rangle$, and I have distinct spatial distributions. As described in Sect. 2.1.2, $\langle|\vec{E}|^2\rangle$ is the time-averaged squared modulus of the electric field, $\langle|\vec{B}|^2\rangle$ is the time-averaged squared modulus of the magnetic field, and the intensity I is the time-averaged Poynting vector. As already mentioned in Sect. 2.1.2, the electric field component alone is relevant for the absorption processes of interest. While the I-distribution within the focus is rotationally symmetric with respect to the optical axis (not depicted), the $\langle|\vec{E}|^2\rangle$-distribution is not. Instead, the latter is rather elongated along the direction of the beam polarization before focusing (see Fig. 2.5 (a) for corresponding numerical results). For circular polarization, the $\langle|\vec{E}|^2\rangle$-distribution is rotationally symmetric as well (Fig. 2.5 (b)). When we compare the linear and circular-polarized cases (Fig. 2.5 (c)), the $\langle|\vec{E}|^2\rangle$-focus for linear polarization is wider along the x-direction but sharper along the y-direction. The anisotropy in the focal field distribution will likely lead to an anisotropic voxel. However, except for some special applications, the building block in DLW should generally be as isotropic as possible. Therefore, we choose the circular polarization in our setup and stick to it throughout the remainder of this thesis.

Beam diameter:

We have already mentioned the fact that the lateral size of a focus spot is proportional to λ/NA. Another rule of thumb states that the axial size even scales like λ/NA^2. As a consequence, high numerical apertures are necessary for tight focusing in the lateral direction and of critical importance for tight focusing in the axial direction. To ensure optimal focusing, the entire NA of the objective lens has to be utilized. The intuitively best situation is to illuminate the objective's entrance pupil with a constant intensity. In this way, beam components impinging under all opening angles (that correspond to positions on the entrance pupil) would be equally weighted. The resulting $\langle|\vec{E}|^2\rangle$-distributions are shown in Fig. 2.6 (a). Figures 2.6 (d, e) display line scans through the data (green lines). The full width at half maximum (FWHM) is 322 nm (786 nm) along the lateral (axial) direction. This situation of a constant illumination intensity would, however, correspond to an incoming Gaussian beam of infinite beam diameter and should therefore rather be seen as a limit for very large beam diameters.

If the incoming laser beam's diameter is much smaller than the entrance pupil of the objective lens, only the inner part of its aperture is illuminated and the NA is effectively decreased below the nominal value. Out of the box, common laser sources often have beam diameters[1] between 1 mm and 2.5 mm, whereas the entrance pupils of common oil immersion lenses are in the range of $4 - 6$ mm. When using such beams directly, a focus like shown in Fig. 2.6 (b) results, where the beam diameter has been chosen to be 40%

[1]Beam diameters of Gaussian beams are commonly measured between the points in space where the beam intensity drops to e^{-2} of the maximum value.

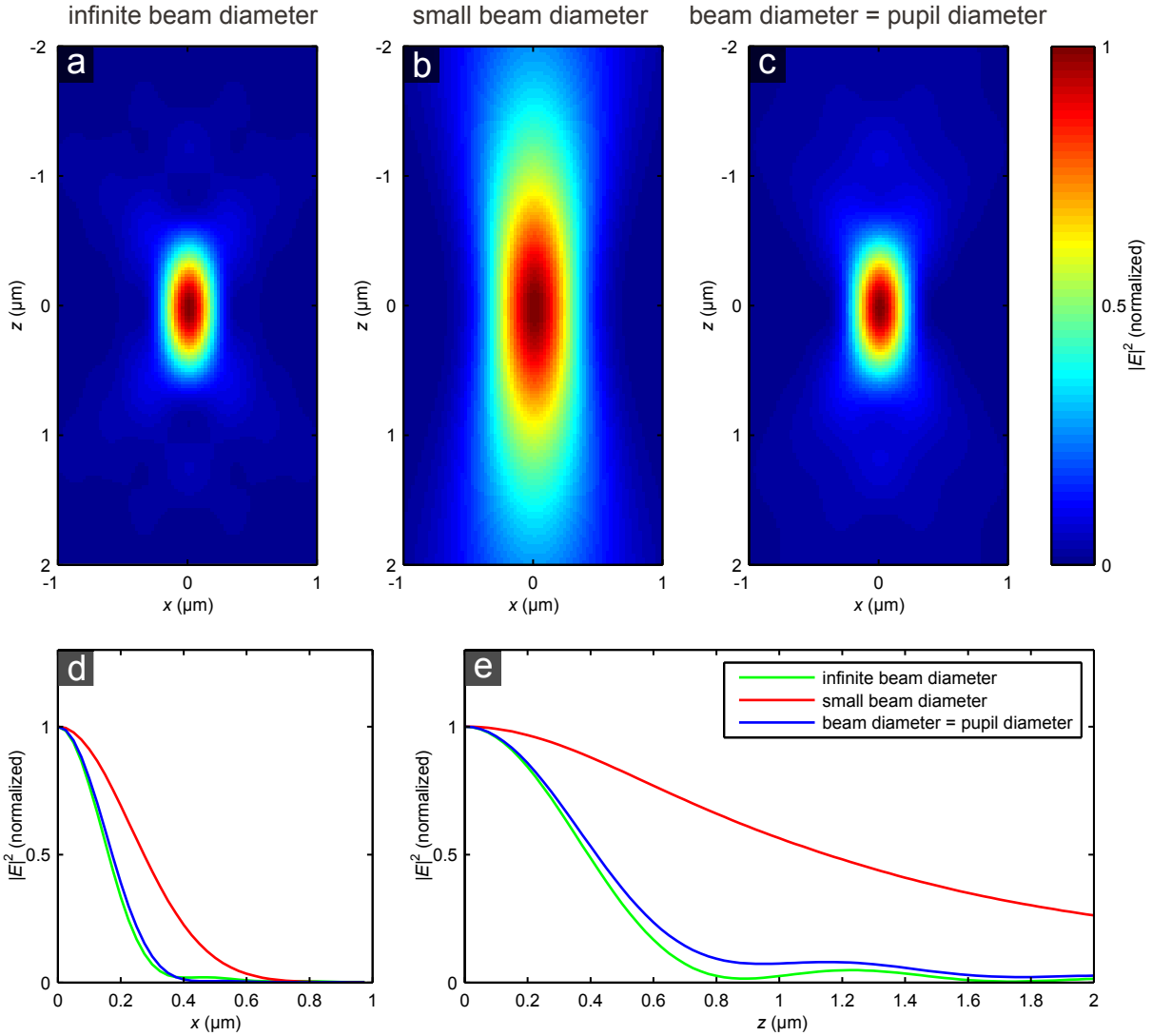

Figure 2.6.: Calculated distributions of $\langle|\vec{E}|^2\rangle$ in the focus for different beam diameters and circular polarized light. (a) x-z-slice for an infinite beam diameter (*i.e.*, the objective is illuminated by a plane wave). (b) x-z-slice for a beam diameter of 40% the pupil diameter. (c) x-z-slice for a beam diameter that equals the pupil diameter. (d, e) Line scans from the origin along the lateral and axial direction, respectively. Negative r and z values are not plotted due to the symmetry of the distribution with respect to the origin. Furthermore, all distributions are rotationally symmetric around the z-axis.

of the pupil diameter. Clearly, the lateral and especially the axial extent are massively enlarged (Fig. 2.6 (d, e)).

For a large laser beam, only a part of the beam's power is entering the finite objective aperture whereas the rest of the beam is blocked and therefore lost. Here, a trade-off between tightness of the focus and transmitted laser power arises. A commonly used compromise is to choose the beam diameter equal to the entrance pupil diameter. For this configuration, a focus like depicted in Fig. 2.6 (c) results. The lateral and axial FWHM are

both increased by only 7% with respect to a homogeneous illumination. While 86% of the beam contribute to the focus, only 14% are lost in the Gaussian tails. This configuration is a good compromise with close to perfect focusing and efficient power usage.

In our experimental setup the power of the writing laser is not a limiting factor. Thus, we will choose the beam diameter to be roughly twice the entrance-pupil diameter. In STED microscopy, the depletion-laser power is very often limiting the attainable resolution. Along the lines of the above considerations, the diameter of this STED beam is often chosen to be equal to the entrance-pupil diameter. For the depletion beam of our experimental setup, we will also choose the beam diameter accordingly (see Sect. 4.1).

2.3. Resolution in optical lithography

In this chapter, we will elaborate on the term resolution for different exposure conditions in lithography. The Oxford dictionary online [54] states that "to resolve" in the context of optical or photographic equipment is synonymous with "to separate or distinguish between (closely adjacent objects)". Along these lines, we will use the term resolution in lithography for the minimum attainable distance between two objects that are still separated. As we will argue below, the size of a single exposed feature is not necessarily related to the resolution of the lithographic system used.

We will start the chapter by recalling the considerations of Ernst Abbe related to his famous diffraction-limit formula. We will see that this formula only applies to single parallel exposures, *e.g.*, to planar interference lithography or 3D holographic lithography. Nevertheless, it will become clear that resolution can fundamentally differ from linewidth for such exposure schemes. Next, we will turn to the Sparrow criterion, which (under certain assumptions) allows to describe serial exposures schemes like DLW optical lithography. Again, resolution and linewidth can differ tremendously.

Major parts of the following Sections 2.3.1 and 2.3.2 have already been published in Ref. [55] during the course of this thesis and have partly been taken over verbatim.

2.3.1. The Abbe diffraction limit

In the late 19th century, Ernst Abbe systematically investigated the resolving power of optical microscopes leading to his famous formula [2, 56]. He considered a grating with period a_{xy} in the x-y-plane inspected using an objective lens. The optical axis is along z and a plane wave impinging along this direction serves for illumination. He argued that at least the zeroth and both first diffraction orders of the grating need to be collected by

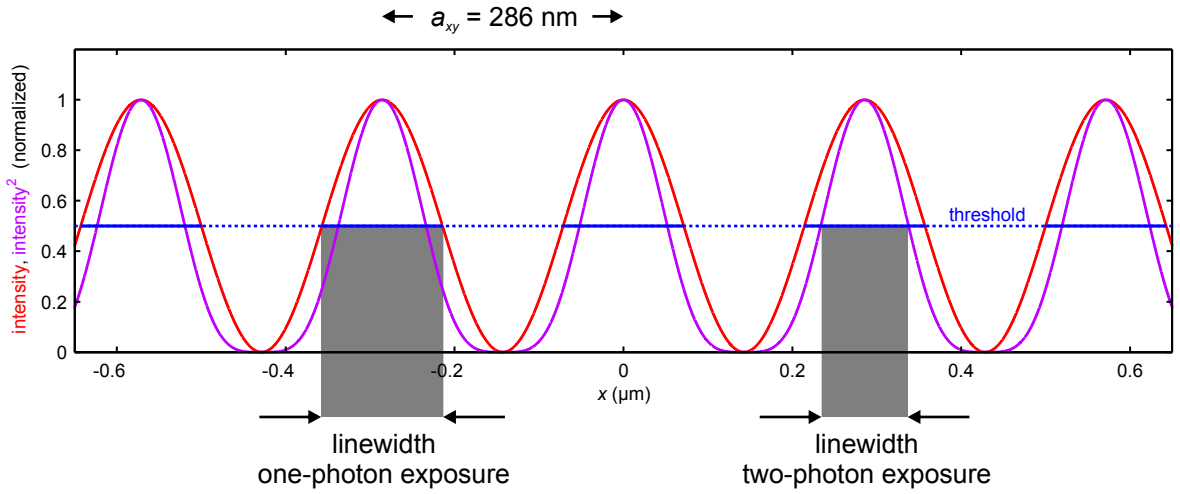

Figure 2.7.: Diffraction-limited intensity grating (red) applicable to parallel exposures of photoresist films. The squared intensity (purple) is relevant for a parallel two-photon exposure. For a fixed exposure time, the threshold dose translates into a threshold intensity (blue line), which determines the width of the exposed lines. The incident vacuum wavelength is 800 nm and the numerical aperture NA = 1.4. Previously published in Ref. [55].

the lens' aperture in order to retain the information on the grating period. By using the usual Fraunhofer diffraction formula for a grating, it is straightforward to arrive at the Abbe condition

$$a_{xy} \geq \frac{\lambda}{2n \sin \alpha} = \frac{\lambda}{2\,\mathrm{NA}}\,, \tag{2.7}$$

where λ is the vacuum wavelength of light, n the refractive index of the material in which the grating and the lens are embedded, α is the half-opening angle of the microscope-lens aperture, and NA is the numerical aperture.

If we now time-invert the scenery, we have three plane waves (zeroth and both first diffraction orders) entering the objective lens and traveling backwards to the focal plane where they interfere and form an intensity grating of the same critical period (see Fig. 2.7 for an example). This grating can then be used for a parallel "single-shot" exposure of a photoresist film. In this way, a grating of the critical period can be created *via* lithography. As mentioned in Section 2.1.1, we define the exposure dose to be proportional to the number of absorbed photons, hence $D \propto |\vec{E}|^2 \cdot T$ for 1PA and $D \propto |\vec{E}|^4 \cdot T$ for 2PA, where T is the exposure time.[4]

So far, we have only examined the light propagation and its diffractive nature. We have already mentioned in Section 2.1.2 that a non-linear optical or chemical response of the photoresist on the exposure light is required in 3D DLW. Would such a non-linearity also help to improve the resolution of a parallel exposure defined along the lines of Abbe's considerations? One could for example exploit 2PA instead of 1PA. However, the above reasoning would not change at all. The exposure pattern with grating period a_{xy} would only change its shape (see Fig. 2.7, purple line). While the intensity of the interference

[4]For simplicity, we will further assume $I \propto |\vec{E}|^2$ within this subsection.

grating relevant for 1PA is given by $\cos^2(\pi x/a_{xy})$, the square of the intensity relevant for 2PA follows $\cos^4(\pi x/a_{xy})$. While the maxima of the one-photon exposure dose have a FWHM given by

$$\mathrm{FWHM}_{1\mathrm{PA}} = a_{xy} \cdot \frac{2\,\mathrm{acos}(\sqrt[2]{0.5})}{\pi} = \frac{a_{xy}}{2} = \frac{\lambda}{4\,\mathrm{NA}}\,, \tag{2.8}$$

the FWHM of the two-photon exposure maxima is given by

$$\mathrm{FWHM}_{2\mathrm{PA}} = a_{xy} \cdot \frac{2\,\mathrm{acos}(\sqrt[4]{0.5})}{\pi} \approx \frac{a_{xy}}{2.75} = \frac{\lambda}{5.5\,\mathrm{NA}}\,. \tag{2.9}$$

Indeed, squaring the pattern does reduce the FWHM of the maxima by roughly a factor of 1.4 . However, the attainable grating period is not affected and, hence, the resolution in a single parallel exposure is not improved by the introduction of 2PA.

Another type of non-linear behavior can be introduced by the photoresist. Independent of whether the exposure photons are absorbed *via* 1PA or 2PA, the photoresist can respond non-linearly to the resulting exposure dose. One example is the polymerization threshold that is commonly observed in photoresists. While the photochemistry leading to such a threshold behavior is quite complex it can usually be described within the digital model mentioned in Section 2.1.1. Within this threshold model, the photoresist is only sufficiently exposed where the local exposure dose exceeds a certain threshold value (see Fig. 2.7). Like the use of 2PA, this kind of chemical non-linearity can also lead to decreased feature sizes. Reducing the exposure dose towards the threshold dose by decreasing either exposure intensity or exposure time leads to smaller linewidths. In this fashion, arbitrarily small linewidths could be achieved – in principle. However, exactly as in the case of the optical non-linearity, the minimum period is still limited by the above Abbe formula and, hence, the resolution is not improved by the chemical non-linearity.

The example of a single-shot parallel exposure with an interference grating has shown that linewidth and resolution are generally not the same. In fact, in this example the resolution is fundamentally limited by the Abbe limit, whereas the linewidth is not limited at all. Consequently, in order to claim a certain resolution experimentally, we have to fabricate a grating with the corresponding period. Two adjacent features separated by the corresponding distance would still deserve the term “resolved” in the literal sense. The extent of a single feature, however, is not a convenient measure for the resolution in the literal sense or in the sense of Abbe. Although, in practice, achieving small feature sizes is very challenging as well, we should try not to confuse these two notions.

When aiming at 3D structures, we also have to carefully distinguish between lateral resolution (a_{xy}) and axial resolution (a_z). Abbe’s original formula does not make a statement on the axial resolution. We can, however, extend Abbe’s reasoning in a straightforward fashion by considering four (or more) laser beams with different wave vectors $\vec{k}$ that are sent through the microscope objective towards the sample and form a 3D interference pattern which can be used for a parallel exposure of a thick photoresist film [57, 58]. The accessible bandwidth of k_z-components determines the axial resolution. Clearly, two beams counter-propagating on the optical axis would span the largest bandwidth $\Delta k_z = 2|\vec{k}| = 4\pi n/\lambda$, where $\vec{k}$ is the wave vector

inside a medium of refractive index n and λ is the vacuum wavelength. However, an imaging geometry with a single objective lens does not allow for positive and negative k_z-components at the same time. Furthermore, the finite NA of the objective only permits wave vectors with certain directions, leading to further limited axial bandwidth $\Delta k_z = |\vec{k}| - |\vec{k}| \cdot \cos\alpha = (1 - \cos\alpha) \cdot 2\pi n/\lambda$. The minimum axial period of the hologram is finally given by

$$a_z \geq \frac{2\pi}{\Delta k_z} = \frac{\lambda}{n(1-\cos\alpha)} = \frac{\lambda}{n - \sqrt{n^2 - (\mathrm{NA})^2}}\,. \tag{2.10}$$

The smallest possible a_z is obtained for $n = \mathrm{NA}$, where the full half-space contributes to the k_z-bandwidth. In this case, the axial resolution is a factor of two worse than the lateral one. For realistic numerical apertures, the ratio a_z/a_{xy} further increases. For the common DLW parameters $n = 1.5$ and $\mathrm{NA} = 1.4$, this ratio becomes 2.92. For a smaller numerical aperture $\mathrm{NA} = 1.0$ (which corresponds to the maximum NA for objectives without an immersion medium), the resolution ratio increases to 5.26. These numbers clearly indicate that for a single lens approach achieving good axial resolution is even more of a challenge than achieving good lateral resolution.

In contrast to this Gedankenexperiment of parallel interference exposure, DLW is a serial process. In a serial process, nonlinearities can be fully exploited. As we assume that doses of sequential exposures simply accumulate linearly (which is a conservative assumption), the reduced width of a single exposure (*e.g.*, a line) can indeed translate to enhanced resolution. The use of 2PA in a serial scheme therefore improves the resolution by roughly a factor of $\sqrt{2}$, as we will argue in Section 2.3.2.

In contrast to our usual assumption of accumulating exposure doses, one might even be tempted to assume that the photoresist "forgets" any below-threshold contributions of a first line's exposure, *e.g.*, due to diffusion exchange.[5] In this case, a second line could indeed be located within one linewidth (center-to-center) next to the first line. The gap between the two lines could even be smaller. In fact, nothing would fundamentally limit this gap. Hence, resolution (*i.e.*, minimum period) and linewidth would essentially be the same.

The experimental findings of this thesis to be discussed in Chapter 6 are indeed consistent with a $\sqrt{2}$-fold resolution improvement by two-photon absorption. We will also see, however, that the reasoning regarding the threshold and the "forgetting photoresist" is highly oversimplified: First, a perfect threshold could allow for arbitrarily small linewidths. In reality, the smallest accessible linewidths are roughly 40% of the 2PA FWHM. Second, an ideal "forgetting" photoresist would allow for arbitrarily small gaps (*i.e.*, linewidth would equal resolution). However, photoresist's usually seem to "remember" a lot. In other words, our definition of the exposure dose, *i.e.*, the assumption of a linear accumulation of sequential exposures, is often meaningful indeed.

[5] The Schwarzschild effect found in photographic plates is a similar example for a "forgetting" photosensitive medium and, hence, a deviation from our above simple exposure-dose definition with purely linear accumulation. The Schwarzschild effect corresponds to no darkening of the photographic plate if the incident light intensity is below a certain value – no matter how long the plate is illuminated.

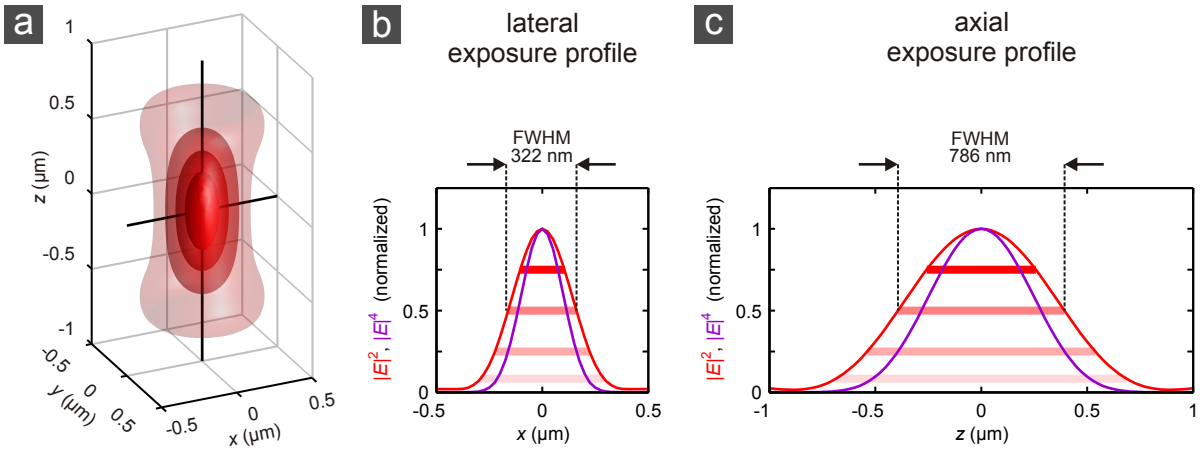

Figure 2.8.: Calculated $|\vec{E}|^2$-distribution of a typical writing spot. (a) Iso-surfaces of $|\vec{E}|^2$. The profiles along the two black lines are depicted in (b) and (c). (b) Lateral profiles of $|\vec{E}|^2$ (red) and $|\vec{E}|^4$ (purple) correspond to one-photon exposure and two-photon exposure, respectively. (c) Axial profiles of $|\vec{E}|^2$ (red) and $|\vec{E}|^4$ (purple). The horizontal lines in (b) and (c) correspond to the iso-intensity values of the surfaces in (a). Previously published in Ref. [55].

2.3.2. The Sparrow criterion

As in optical microscopy, one can arrive at similar definitions of "resolution" in optical lithography by reasonings different from those of Abbe. In fluorescence microscopy, the Abbe criterion nearly coincides with the Sparrow criterion. Sparrow originally investigated the diffraction-limited resolving power of spectroscopes. He found that a spectral line pair (broadened by diffraction) is still resolvable as long as there is a local minimum in the middle of the signal [59].

This so-called "undulation condition" [59] can easily be translated to fluorescence microscopy. Here, two slightly separated point emitters appear broadened by the microscope's point-spread function. In order to be resolvable, the sum of the shifted point-spread functions must still have a local minimum. This criterion is also relevant to serial lithography schemes like DLW, if we assume that the entire doses of sequential exposures just accumulate, *i.e.*, that the photoresist remembers everything. The required local minimum in the sum of two shifted point exposures is then crucial for the separation of the points, even for a perfectly sharp threshold. Translating this criterion to sequential two-photon exposures is achieved by replacing the intensity profiles by their squares.

To evaluate the resolution in this sense, one needs detailed knowledge of the laser focus. Here, we complement the above simple analytic considerations by numerical calculations described in Section 2.2.1. We choose parameters corresponding to typical experiments, in particular an exposure wavelength of 800 nm. The scalability of the Maxwell equations allows for translating these results to other exposure wavelengths. The numerical aperture is NA = 1.4 and the incident laser light is circularly polarized. The objective lens is illuminated homogeneously. The resulting distributions of the squared modulus of the (complex) electric-field vector, $|\vec{E}|^2$, and the square of that, $|\vec{E}|^4$, are depicted in Fig. 2.8.

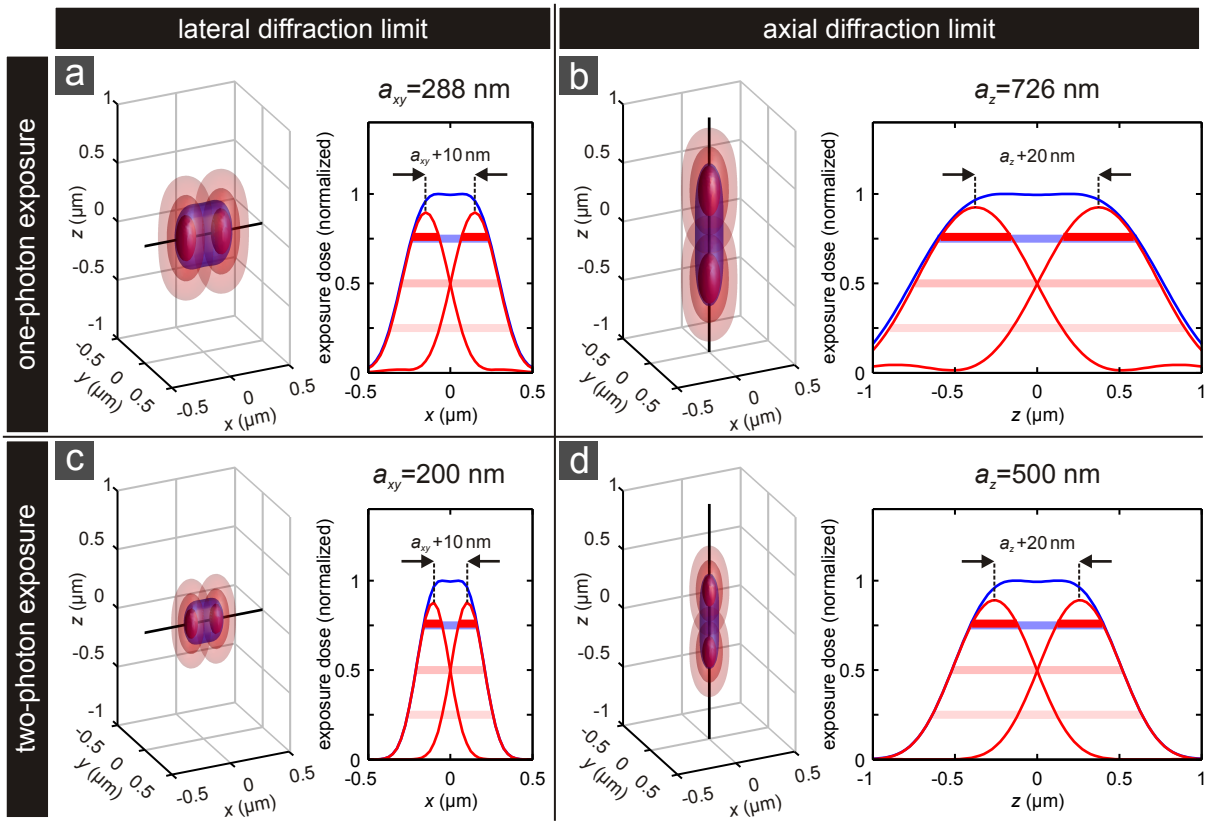

Figure 2.9.: Exposure-dose distributions for two point exposures close to the Sparrow criterion. The critical distances, a_{xy} and a_z, are derived from numerical calculations. All plots shown use slightly larger values as indicated (*i.e.*, $a_{xy} + 10\,\text{nm}$ and $a_z + 20\,\text{nm}$) such that small local minima are still visible. The exposure-dose profiles along the black lines in the iso-intensity plots (left-hand side of each panel) are plotted separately (right-hand side of each panel). The line plots show the contributions of the single exposures (red) and the sum of both (blue). (a) Critical lateral distance, a_{xy}, for one-photon exposure. (b) Critical axial distance, a_z, for one-photon exposure. (c, d) Same as (a, b), but for two-photon exposure. A typical value for the polymerization threshold in lithography (75% of the peak dose) is used as dose value for the blue iso-surfaces, illustrating that the two point exposures are not separated any more. Parameters are: 800 nm free-space wavelength, NA = 1.4, and circular polarization. Previously published in Ref. [55].

To obtain the resolution according to Sparrow, we add two numerically computed exposure profiles that are shifted with respect to each other in either the lateral or the axial direction. We decrease the distance in steps of 1 nm until the local minimum in the sum vanishes. We choose the smallest distance that still yields a local minimum to be the critical distance. Again, we use $D \propto |\vec{E}|^2 \cdot T$ for 1PA, and $D \propto |\vec{E}|^4 \cdot T$ for 2PA and choose a fixed exposure time T. The results are depicted in Figure 2.9. For one-photon exposure, we find the critical distances to be $a_{xy} = 288\,\text{nm}$ in the lateral direction and $a_z = 726\,\text{nm}$ in the axial direction. The lateral value is very close to the analytic Abbe criterion ($a_{xy} = 286\,\text{nm}$). For two-photon exposure, the critical distances are reduced to

$a_{xy} = 200\,\mathrm{nm}$ in the lateral direction and $a_z = 500\,\mathrm{nm}$ in the axial direction. Assuming Gaussian profiles in lateral as well as in axial direction, one would expect that squaring the profiles would reduce their extent, and hence also their critical distance, by a factor of $\sqrt{2}$. For the lateral direction, this simple reasoning leads to a two-photon-modified Abbe formula

$$a_{xy} = \lambda/(2\sqrt{2}\,\mathrm{NA}) = 202\,\mathrm{nm} \tag{2.11}$$

that, indeed, nicely resembles the numerical result for the two-photon Sparrow criterion.

As expected, the numerical calculations show that the critical distances along the axial direction are significantly larger than the lateral ones, just like the FWHM of the exposure-dose profiles along the two axes. The elongation factors of FWHMs and critical distances for one-photon and two-photon exposure profiles range from 2.45 to 2.52. Hence, we suggest a further modified Abbe formula

$$a_z = \lambda\,\mathrm{AR}/(2\sqrt{2}\,\mathrm{NA}) = 505\,\mathrm{nm} \tag{2.12}$$

for the axial direction, where $\mathrm{AR}(\mathrm{NA}, n) = 2.5$ is the aspect ratio of the exposure volume for $\mathrm{NA} = 1.4$ and $n = 1.52$. Again, this intuitive and handy formula nicely approximates the numerical results for the generalized two-photon Sparrow criterion.

To conclude this section, we want to remind the reader of the main points elaborated herein. In the case of a single parallel exposure (*e.g.*, with an interference grating) the resolution is fundamentally limited by Abbes formula – independent of any non-linearities. A non-linear optical behavior or a threshold behavior of the photoresist can, however, lead to very small feature sizes that are not limited by diffraction.

For a sequential exposure scheme like two-photon DLW, we can likewise state that the feature size is not directly limited by diffraction. If we assume that the photoresist "remembers" all previous below-threshold exposures, the Sparrow criterion can be used to describe sequential two-photon exposures. Again, under this assumption, the resolution in the sense of Sparrow is fundamentally limited by diffraction. We will see in Chapter 6 that this assumption is not entirely true, yet a very good approximation.

3. Combining DLW with a depletion mechanism

In this chapter we will describe the potential combination of DLW optical lithography and the core idea from STED optical microscopy. Benefits, challenges, and limitations will be analyzed.

Major parts of this chapter have already been published in Ref. [55] during the course of this thesis and have partly been taken over verbatim.

3.1. The depletion idea – from microscopy to lithography

As described in Chapter 1, it is desirable to effectively decrease the lateral and/or the axial extent of the exposed volume. Diffraction sets fundamental lower limits for this volume. It is Stefan Hell's deceptively simple yet ingenious idea of introducing a depletion laser that enables circumventing this limitation [5, 6, 60–65]. This idea and its derivatives have already revolutionized fluorescence microscopy (see, *e.g.*, the special issue [64] for reviews and state of the art). Let us briefly draw the analogy between laser-scanning fluorescence microscopy and lithography at this point. In this section, we will explain the basic idea of depletion with stimulated emission as an exemplary mechanism. This general depletion concept is, however, not restricted to this depletion mechanism.

In modern laser-scanning fluorescence microscopy, a laser beam is used to excite fluorescent molecules within a specimen. Unlike in wide-field fluorescence microscopy, commonly only parts of the focal plane are illuminated. Standard laser-scanning microscopes use a single focused laser spot that is raster-scanned through the focal plane (see Fig. 3.1 (a) for an abstract illustration of the excitation profile). The molecules within the excitation laser-spot are usually excited *via* 1PA and emit fluorescence photons subsequently. The light is collected through the same objective and guided to a single

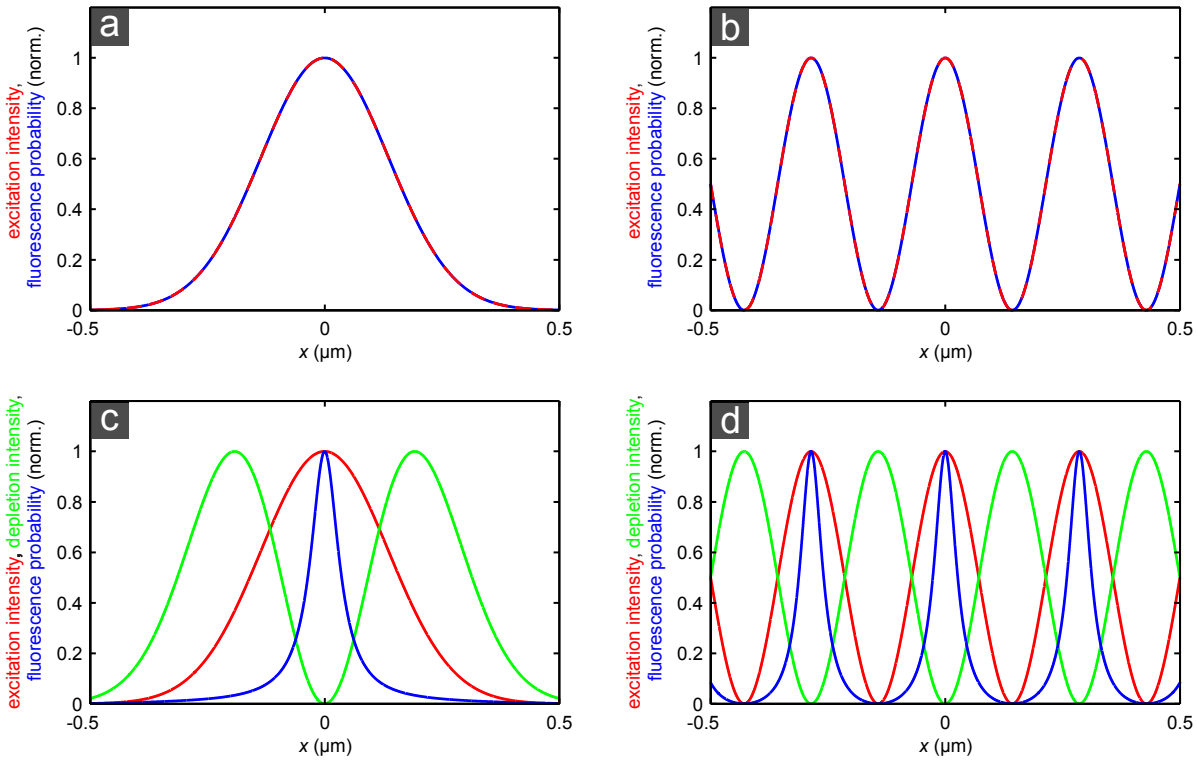

Figure 3.1.: Illustration of the basic idea in STED microscopy. A continuous fluorescing medium is assumed. (a, b) Diffraction-limited excitation patterns (red) usually induce fluorescing patterns of the same shape (blue). (c, d) An additional depletion pattern can reduce the extent of the fluorescing pattern below the initial extent. Increased resolution is obtained by time-sequential spatial scanning of this sharper pattern.

photodetector.[1] During sequential raster-scanning, the detected fluorescence intensities for different positions of the excitation spot are assigned to the pixels of the final image. More parallelized approaches may use moving interference gratings for excitation (see Fig. 3.1 (b)) and cameras for detection.

Clearly, if many fluorescent molecules are within one spatial maximum of the excitation profile, all of them will be excited leading to a rather simultaneous photon emission. In case of a single photodetector, the entire fluorescence is detected and all molecules within the excitation volume will contribute to a single pixel of the final image. In case of a camera-detection scheme, the imaging pathway back to the camera similarly leads to a loss in spatial information, such that the molecules can not be distinguished either.

The solution of this problem is to hinder the molecules within one maximum to emit at the same time. Only a small portion confined to a smaller volume is allowed to actually emit. One way to suppress the emission locally is to use STED. Usually, dye molecules are excited, remain in their first excited singlet (S_1) state for roughly 2 ns, and then fluoresce

[1] Usually, a confocal detection through a pinhole is used to increase the contrast along the axial direction. As the idea of STED also works without a pinhole, we want to assume that the entire fluorescence is collected and eventually contributes to the value of a single pixel of the final picture.

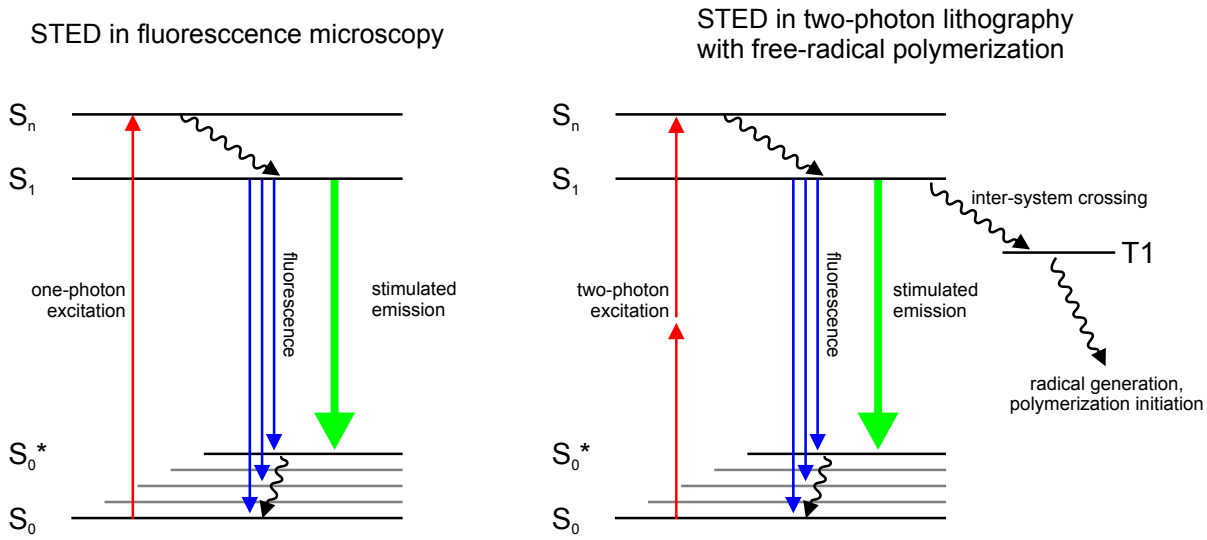

Figure 3.2.: Jablonski diagrams for a fluorescent dye molecule in STED microscopy (left) and a photoinitiator molecule in STED lithography (right). In STED microscopy, dye molecules are excited and then quickly forced to undergo stimulated emission. Through this efficient depopulation of the S_1 state, spontaneous emission can be strongly reduced. In STED lithography, photoinitiator molecules are excited *via* 2PA and also forced to undergo stimulated emission. In this case, the depopulation decreases the intersystem-crossing quantum yield and, hence, the contribution to the polymerization initiation.

(see Fig. 3.2, left side). In the additional presence of an intense STED laser-beam of the appropriate wavelength, however, the molecules will likely undergo stimulated emission while they are in the S_1 state. Every molecule that undergoes stimulated emission does not contribute to the fluorescence signal. Indeed, these molecules emit photons *via* stimulated emission. These photons have exactly the same wavelength as the STED laser (and therefore can be filtered out before the detector) and are also emitted in the direction of the STED laser beam (hence, leave the sample in the wrong direction). In contrast, the fluorescence of undisturbed molecules is broadband and non-directional (and can, hence, be collected in the backward direction). The higher the intensity of the STED beam, the higher is the probability for stimulated emission and the lower is the probability for fluorescence. The vibronic relaxation from S_0^* to S_0 is usually considered to be very fast (often less than 1 ps [60]) such that re-excitation from S_0^* to S_1 by the intense STED beam can be neglected.

Clearly, this on- and off-switching of the molecules' detectable fluorescence only makes sense if the resulting spatial distribution of the remaining fluorescing molecules is sharper than the initial diffraction-limited one. This is achieved by overlaying spatial maxima of the excitation profile (red) with local zero-intensity points in the depletion profile (green) as depicted in Fig. 3.1 (c, d). In this manner, the excited molecules at the positions of the depletion zeros are not affected at all. For all other molecules, the fluorescence yield is decreased and therefore the profile of fluorescing molecules (blue) gets sharper. By further increasing the overall depletion intensity, the fluorescence yield in the spatial tails

of the distribution is further decreased while the molecules at the depletion zeros remain undisturbed. This leads to a further confinement of the fluorescent volume without any fundamental lower limit.

Importantly, a gain in resolution is not attained by decreasing the fluorescent volume alone, as the periods of the excitation and depletion pattern remain unchanged. In addition, a time-sequential readout by scanning of the foci or the gratings is necessary. Therefore, the switching process has to be reversible. In case the depletion laser would irreversibly switch off the molecules, the depleted areas could not be read out later on. For a single-spot laser-scanning approach, a rule of thumb states that an n-fold resolution increase in m dimensions requires at least n^m reversible switching cycles. For a 10-fold increase along all spatial directions of a three-dimensional volume scan this equals 1000 reversible switching cycles.

In principle, the STED idea can be directly transfered from fluorescent dye molecules to the photoinitiator molecules within a photoresist. In conventional DLW, light from a laser excites the photoinitiator molecules *via* 2PA (see Fig. 3.2, right side), commonly using a single focused laser spot. As before, molecules may emit fluorescence photons. Nevertheless, the majority of the molecules will undergo intersystem crossing to a triplet state and eventually generate radicals. These radicals initiate the polymerization reaction that leads to an irreversible solidification of common negative-tone photoresists. If the molecules are forced to undergo efficient stimulated emission while they are still in the S_1 state, they can not contribute to this chemical reaction. In this way, the exposure dose is effectively reduced, as not all absorbed excitation photons and not all excited molecules can likewise contribute to the chemical reaction. We will call this decreased exposure dose the "effective exposure dose". Using appropriate spatial profiles for excitation and depletion, the effective exposure-dose distribution can again be confined towards the zeros of the depletion pattern, just like the distribution of fluorescing molecules in STED microscopy.

As in microscopy, the usage of STED or other depletion mechanisms does not directly improve the resolution, it only reduces the extent of the effective exposure-dose profiles. However, time-sequential exposures with raster-scanned foci then lead to an improved resolution.

Finally, not only STED but also any other light-induced mechanism that disturbs the process chain between excitation and the formation of the final chemical product can reduce the effective exposure dose and, hence, serve as depletion mechanism for STED-like lithography approaches. From now on, we will call this class of approaches "depletion DLW".

While no working mechanisms had been known at the beginning of this thesis, alternative depletion methods have been developed in the meantime [66, 67]. In Section 3.6, we will summarize possible microscopic depletion mechanisms in photoresists suitable for depletion DLW.

To describe a generic depletion mechanism, we assume that the effective exposure dose is given by

$$D_{\text{eff}} = D_0 \cdot \frac{1}{1 + \gamma I_{\text{depl}}}, \tag{3.1}$$

where D_0 is the undisturbed exposure dose, I_{depl} is the local depletion intensity, and γ is a photoresist-specific constant containing, *e.g.*, the cross-section of the depletion mechanism. We will derive this scaling for STED explicitly in Sec. 3.6.1. Nevertheless, the outcome describes any depletion mechanism relying on a single molecular transition properly.

3.2. Depletion foci for lateral and axial resolution enhancement

Fortunately, the know-how for realizing suitable depletion foci can be copied from fluorescence microscopy (see, *e.g.*, Ref.[68]). A well-known and widely used focus is the so-called donut mode which is illustrated in Fig. 3.3 (a–c). It can be realized by introducing a helical phase mask as shown in Fig. 3.3 (d) into the beam. Here, the additionally accumulated optical phase increases from zero to 2π in one turn along the azimuth. Upon using circular polarization of the correct handedness, a wavelength of 532 nm and a numerical aperture of NA = 1.4, the intensity distribution shown in Fig. 3.3 (a–c) results. The optical intensity on the entire optical axis is strictly zero. Thus, depletion will never occur here and the axial distribution essentially remains unaffected. However, this focus nicely allows for reducing the lateral extent of the effective exposure profile. This may be useful for planar optical lithography, but is quite undesirable for truly 3D optical lithography, where the worst spatial resolution (which is usually the z-direction) limits the making of arbitrarily complex 3D structures.

Thus, the bottle-beam focus shown in Fig. 3.3 (f–h) is more attractive for 3D DLW. This focus can be achieved by replacing the helical phase mask by the one shown in Fig. 3.3 (h). Here, a cylindrical disk in the center of the beam introduces a π phase shift. For a homogeneously illuminated objective, the diameter of the cylinder needs to be $1/\sqrt{2}$ of the pupil diameter, such that the cylinder covers half of the relevant beam area. In the resulting bottle-beam focus, the intensity in the center of the focus is strictly zero. In contrast to the donut, however, the intensity not only rises radially but also along the optical axis. In fact, the depletion effect is more pronounced in the axial direction because the depletion-intensity profile rises more steeply along the optical axis and because the initial excitation volume is elongated in this direction. This aspect will lead to a more pronounced axial linewidth improvement compared to the lateral one. The ultimate ratio

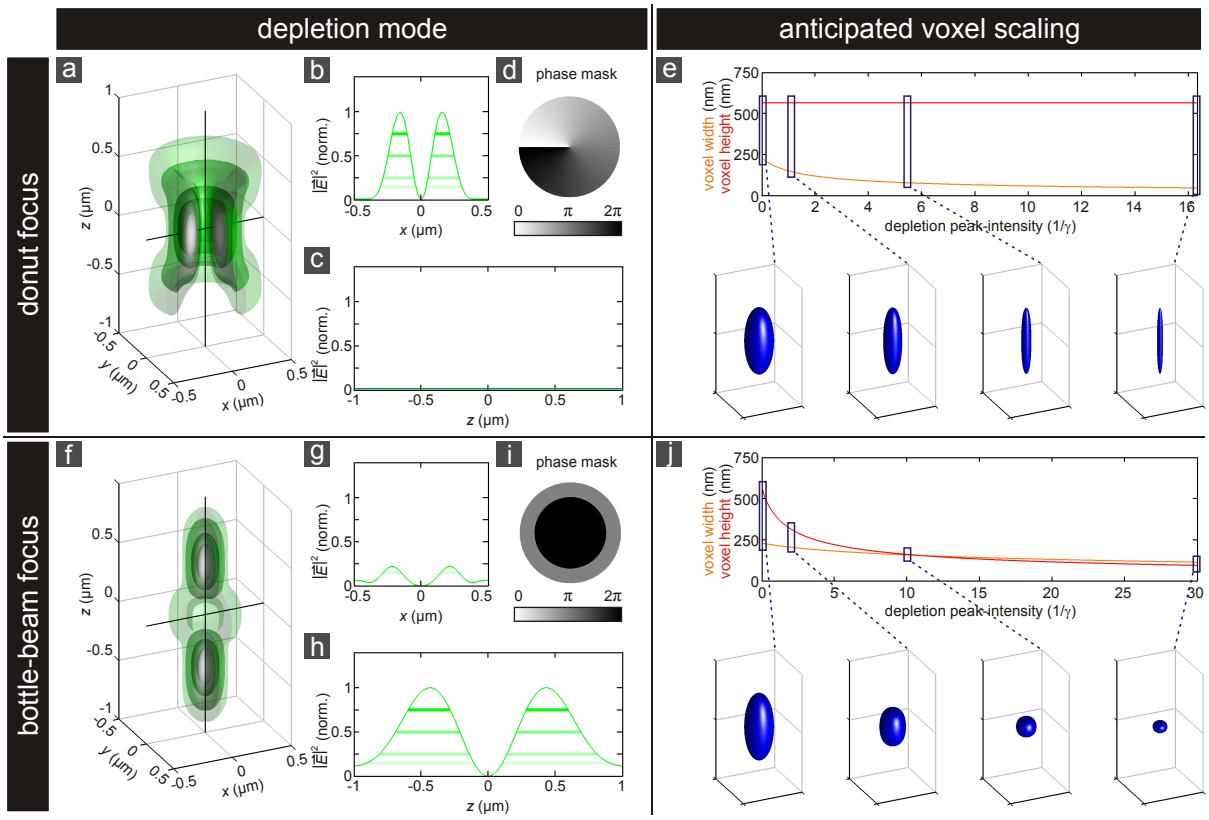

Figure 3.3.: Calculated $|\vec{E}|^2$-profiles for common depletion foci. (a–d) Donut depletion focus. (a) Iso-intensity surfaces of the donut depletion focus. The front x-y-quadrant has been removed to reveal the interior. (b) Lateral intensity profile. (c) Axial intensity profile. (d) Phase mask used for the generation of this focus. (f–h) Same as (a–d), but for a bottle depletion focus rather than a donut. (e, j) The anticipated resolution scaling with increasing depletion power is illustrated with the extent of single voxels for each depletion mode ((e) donut, (j) bottle-beam). Previously published in Ref. [55].

of axial to lateral voxel extent is given by the shape of the inner iso-intensity surfaces of the depletion focus. Equivalently, this ratio is determined by the ratio of the curvatures of the axial and lateral intensity profiles (compare Fig. 3.3 (g) and (h)). For the parameters of Fig. 3.3, the ultimate aspect ratio is 0.7, *i.e.*, the voxels can be smaller along the axial than along the lateral direction.

The two different depletion foci can also be effectively combined by incoherently superimposing two corresponding pulsed depletion-laser beams with a small time delay [69]. Even a coherent superposition of two continuous-wave (cw) beams with circular polarizations of opposite handedness is feasible (calculations not shown). For many applications aiming for complex isotropic 3D nanostructures, the desired voxel aspect ratio is one. The combination of two phase masks allows for controlling the relative steepness of the axial and the lateral intensity minimum *via* the relative phase and amplitude of the two beams. In this way, an aspect ratio of one can be maintained for arbitrarily small voxels.

Anticipated voxel scaling:

Let us get a first impression of the anticipated voxel scaling by using the previously mentioned threshold model. Usually, regions with above-threshold excitation will remain after the development step in a negative-tone photoresist. However, if the depletion factor $1/(1 + \gamma I_{\mathrm{depl}})$ reduces the effective local exposure dose below the threshold, the regions will again wash out in the developer (compare Eq. 3.1). As a result, the anticipated voxels shrink in size. Strictly speaking, not only the voxel (*i.e.*, the above-threshold volume) but also the entire exposure profile shrinks. This also includes the below-threshold regions. Therefore, not only the size of the exposed features but also the resolution in the sense of Sparrow is expected to increase likewise.

For the donut depletion mode, only the lateral width decreases, whereas lateral *and* axial extent decrease for the bottle-beam focus. Exemplary calculations for two-photon excitation and depletion with either of the two depletion profiles are depicted in Fig. 3.3 (e) and (j), respectively. Here, the local effective exposure dose is calculated according to Eq. 3.1, where the squared excitation-intensity profile I_{exc}^2 and the depletion-intensity profile I_{depl} are chosen according to Fig. 2.8 and Fig. 3.3, respectively. The threshold of the photoresist is chosen at 75% of the peak exposure dose. Panels (e) and (j) can directly be compared, as the same depletion-beam power is used. The different depletion modes have different peak intensities and therefore yield different scales on the horizontal axes. Upon continuously increasing the depletion power, the feature sizes converge to zero (see Fig. 3.3 (e, j)). There is no fundamental optics limit for the linewidth and the resolution in optical lithography any more. When taking a close look, one can see that the lateral voxel width is more effectively decreased with the donut mode than with the bottle beam (orange lines in Fig. 3.3 (e, j)).

It is also interesting to study the asymptotic behavior for large depletion powers. Suppose that the feature size is already strongly reduced and entirely limited by the depletion power. The initial shape of the excitation profile is not relevant anymore and we can assume a constant profile instead. The undisturbed exposure dose is $D(x) = D_0 = \mathrm{const}$. In this case, the spatial minimum of the depletion profile can be approximated by a parabola, $I_{\mathrm{depl}} = \mathrm{c}\, P_{\mathrm{depl}}\, x^2$, where c is a proportionality constant. The edge of an exposed feature is given by the condition that the depletion intensity parabola exceeds a certain value I_0, such that the initial (spatially constant) exposure dose is reduced below the polymerization-threshold dose D_{th} (*i.e.*, $D_{\mathrm{eff}}(I_{\mathrm{depl}} \geq I_0) \leq D_{\mathrm{th}}$). Solving the resulting equation $\mathrm{c}\, P_{\mathrm{depl}}\, x^2 = I_0$ for x immediately leads to a feature size that scales like $d = 2x_0 \propto 1/\sqrt{P_{\mathrm{depl}}}$. Note that this reasoning does not involve the above $1/(1 + \gamma I_{\mathrm{depl}})$ depletion factor and should therefore apply to all possible depletion mechanisms alike. Thus, for example, to reduce the feature size by a factor of 10, one needs to increase the depletion power by a factor of 100. This means that undesired but possibly finite 1PA of the depletion beam increases by factor 100, too. Two-photon absorption of the depletion beam increases even by factor 10^4. This unfavorable scaling with depletion power suggests that parasitic processes may at some point overwhelm the desired depletion benefit.

3.3. Reduced noise sensitivity

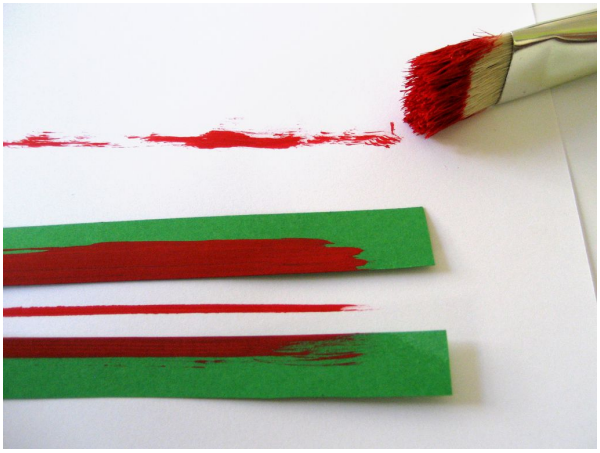

Another anticipated beneficial aspect of depletion DLW is that it can be used to substantially reduce the sensitivity of the critical dimensions (minimum attainable feature size) with respect to errors or fluctuations. For example, lithography industry demands for robustness against power fluctuations as large as 5%. The effect of such fluctuations on DLW is studied in Fig. 3.4. We use the simple threshold model and a hypothetical exposure power with 5% rms noise (Fig. 3.4 (a)). The excitation power fluctuations directly translate into linewidth fluctuations. For these simple calculations, the resulting voxel widths are calculated for each instant value of the excitation power using the numerical data for the focal intensity distribution. The voxel extent along the scan direction was neglected, corresponding to a very fast scan speed (compared to voxel width and noise time-scale). Slower scan speed might lead to averaging along the scan direction, effectively reducing the linewidth fluctuations.

The resulting voxel width and the relative voxel-width fluctuation for conventional DLW and depletion DLW are plotted in Fig. 3.4 (b, c). To decrease the resulting voxel width, one will decrease the excitation power in conventional DLW or increase the depletion power in depletion DLW. The horizontal axes of Fig. 3.4 (b, c) therefore correspond to excitation and depletion power, respectively. While conventional DLW suffers from pronounced fluctuations for small feature sizes, the fluctuations in depletion DLW are nearly independent of the feature size (despite the fact that the depletion laser is assumed to be noisy as well). Three representative examples out of these panels (marked with circles) are selected and explained in the following paragraphs.

When operated at rather high excitation powers (*e.g.*, when the threshold is at the half maximum of the exposure profile), conventional DLW is rather insensitive to noise fluctuations (Fig. 3.4 (d)). Clearly, the resulting feature sizes are rather large. However, when operated close to the threshold (*e.g.*, when aiming for 100 nm linewidth), the noise translates into terrible linewidth fluctuations – the test line even gets disconnected (Fig. 3.4 (e)). Here, the 5% rms power fluctuations (or equivalently about 10% exposure-dose) lead to linewidth fluctuations of 42% rms and peak fluctuations of 100%.

In sharp contrast, depletion DLW allows for having both at the same time, small linewidths and robustness against fluctuations. This fact is illustrated in Fig. 3.4 (f). Here, we again consider 5% fluctuations of the excitation laser, but additionally also 5% (uncorrelated) fluctuations of the depletion laser. As depletion DLW allows to work far away from the polymerization threshold, fairly small edge roughness results.

This increased robustness alone may be a major benefit of depletion DLW for many applications. In many scientific applications, however, the excitation-laser power-

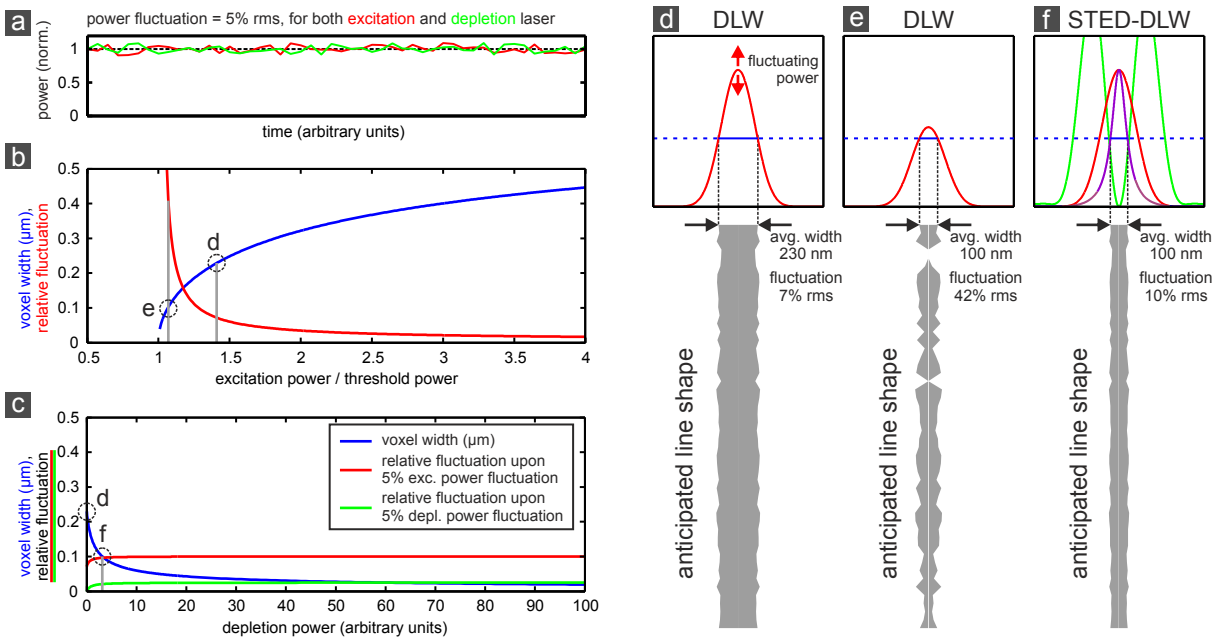

Figure 3.4.: Linewidth fluctuations caused by fluctuating laser power. (a) Fluctuating laser powers for excitation and depletion (uncorrelated random numbers with 5% standard deviation). (b) Voxel width and relative voxel-width fluctuations plotted *vs.* average excitation power for conventional DLW. (c) Voxel width and relative voxel-width fluctuations plotted *vs.* average depletion power in depletion DLW. The excitation power is held constant at 141% of the threshold power. The relative width fluctuations caused by noise of the excitation laser (red) and noise of the depletion laser (green) are plotted separately. Selected working points are marked with circles and illustrated in detail in (d–f). (d) Resulting line shape for conventional DLW where the linewidth equals the FWHM of I_{exc}^2. (e) Shape of a thinner line for conventional DLW. The reduction in linewidth is realized by decreasing the excitation power level to 107% of the threshold power. (f) Shape of a thinner line for depletion DLW. Excitation-power level like in (d), but the depletion power is increased. The depicted line shape accounts for both lasers' fluctuations. The upper panels in (d–f) show calculated I_{exc}^2-distributions of the excitation focus (red), the I_{depl}-distribution of the depletion focus (green), and the anticipated effective exposure profile (purple) along the a lateral axis. The polymerization threshold is indicated in blue. Previously published in Ref. [55].

fluctuations can typically be controlled to nearly 0.1%, in which case this aspect is only of minor importance. We do emphasize, however, that small spatial inhomogeneities of local photoresist properties (*e.g.*, of the local concentration of photoinitiator and/or inhibiting oxygen), which lead to an effective local threshold variation, would have the same effect and may not be avoidable.

It is in general rather disadvantageous to work close to the polymerization threshold [70]. Besides the above linewidth fluctuations due to short term laser fluctuations, any long term change in the excitation power (setup alignment, temperature drift) or in the photoresist properties (oxygen concentration, temperature change) will change the

linewidth by a large margin. This will likely lead to inhomogeneous exposures and irreproducible lithography results. Moreover, as the threshold is not perfectly sharp, exposures close to the threshold will yield a polymer of inferior conversion and cross-linking. Depletion DLW can relax this situation as it allows to work further above the polymerization threshold while maintaining small feature sizes.

3.4. Lithography with low numerical aperture

All considerations have so far assumed a high numerical aperture of NA = 1.4. Such high numerical apertures provide the sharpest focusing and therefore the best attainable spatial resolutions as a starting point. Their drawbacks are relatively high price, small working distances, small fields of view and the need for high-refractive-index immersion liquids. The free working distances (*i.e.*, with substrate thickness subtracted) of such objective lenses are on the order of 100 µm (*e.g.*, 90 µm for the objective Leica HCX PL APO 100×/1.40-0.70 Oil CS used in this work).

Lower-NA lenses are usually less expensive and provide significantly larger free working distances (*e.g.*, 2 mm for a HI PLAN I 40×/0.50 with NA = 0.5). Moreover, these lenses do not need an immersion-liquid and can therefore be used without physical contact to the sample. This can be especially useful, *e.g.*, if a sample is located inside a cryostat. The resolution of lower-NA lenses is of course worse, especially along the axial direction.

For a more quantitative analysis, we calculate the focal intensity distribution of such an objective lens using the numerical code presented in Section 2.2.1. The objective is assumed to be illuminated with circular polarized light of constant intensity. The target refractive-index is still $n = 1.52$, corresponding to the situation that the beam is focused without immersion medium through a substrate into the photoresist. Figure 3.5 (a) displays the calculated $|\vec{E}|^4$-distribution of the excitation focus with an objective lens of NA = 0.5. The exposure profile has a FWHM of 598 nm along the x-direction and 6.1 µm along the z-direction. The resulting aspect ratio is 10.2.

Along the lines of the considerations of Section 3.2, the depletion idea allows to obtain very fine lateral feature sizes with such low numerical apertures by using a donut depletion mode while maintaining the large working distance and field of view.

In contrast, sometimes, large features are even desired. For example, 3D scaffolds [19, 43] for cell-culture often require thick polymer beams. In conventional DLW with high-NA objectives, multiple line exposures have to be combined to achieve a single thick polymer rod. Low-NA objectives allow for larger feature sizes. Usually, the resulting strongly

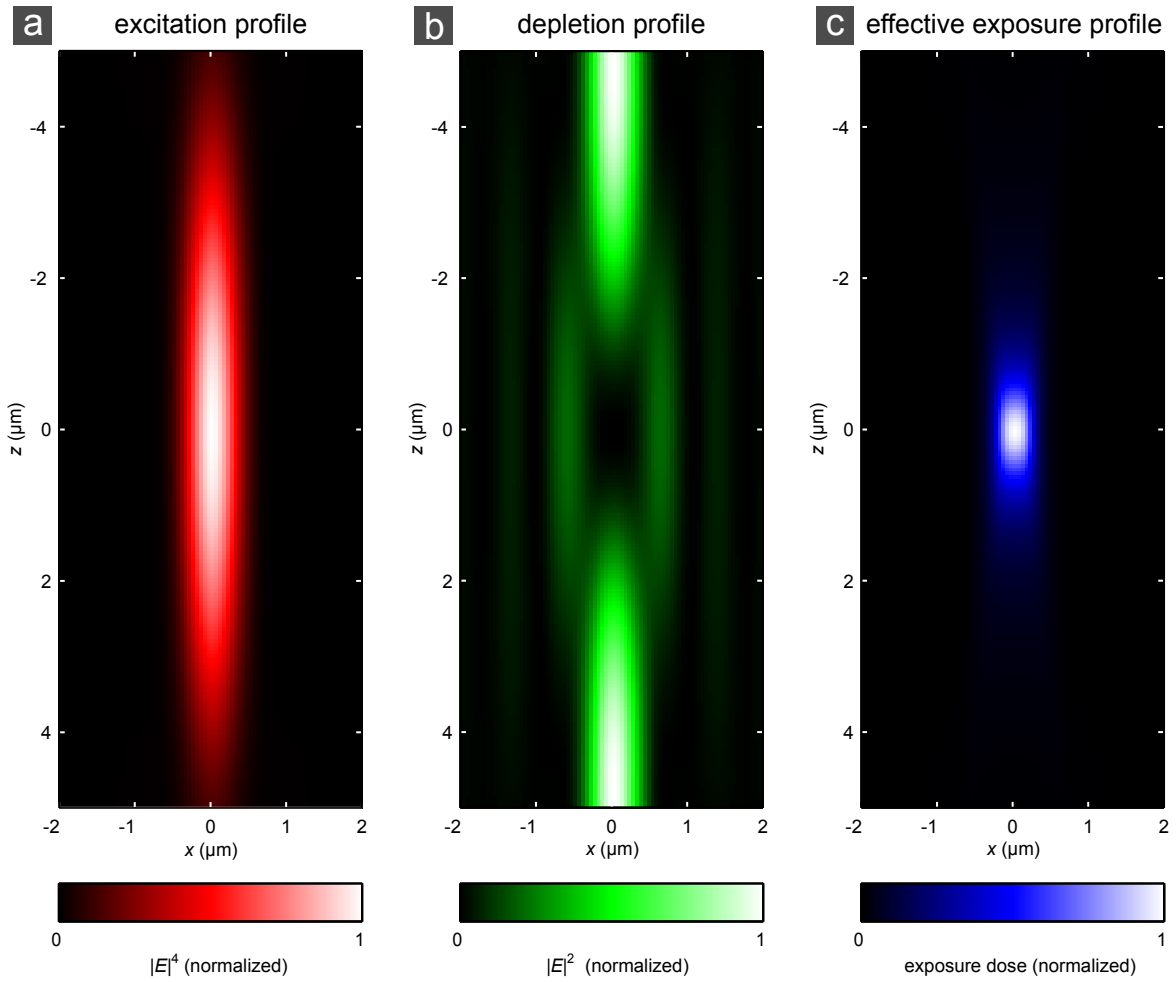

Figure 3.5.: Calculated exposure profiles for a low-numerical aperture objective lens (NA = 0.5). (a) Normalized $|\vec{E}|^4$-profile of the 800 nm excitation-laser relevant for two-photon absorption. (b) Normalized $|\vec{E}|^2$-profile of the 532 nm wavelength depletion-laser. (c) Effective exposure-dose profile calculated as $D_{\mathrm{eff}} \propto |\vec{E_{\mathrm{exc}}}|^4/(1 + 20 \cdot |\vec{E_{\mathrm{depl}}}|^2)$, where E_{exc} and E_{depl} are unit-less and normalized to their respective maximum values.

elongated voxels (see Fig. 3.5 (a)) are undesired and therefore the applicability of low-NA lenses in conventional DLW is rather limited – even when large feature sizes are desired.

Using the depletion idea, the aspect ratio of the fabricated features can be improved. A bottle beam generated through the low-NA objective can help to improve the aspect ratio and to increase the axial resolution as well (see Fig. 3.5 (b)). However, the aspect ratio of the inner iso-intensity surfaces of this depletion focus is larger than one, namely AR ≈ 2. Therefore, even for very effective depletion, the resulting voxel aspect ratio will remain above unity and saturate towards this value. An exemplary resulting exposure dose profile calculated along the lines of Fig. 3.3 (but using low-NA data) is depicted in Fig. 3.5 (c). The aspect ratio of the exposure-dose FWHM is 3.0, the lateral extent of the profile is 419 nm. The extent is roughly twice the value of a conventional DLW exposure with NA = 1.4.

3.5. Time constants of the depletion mechanism

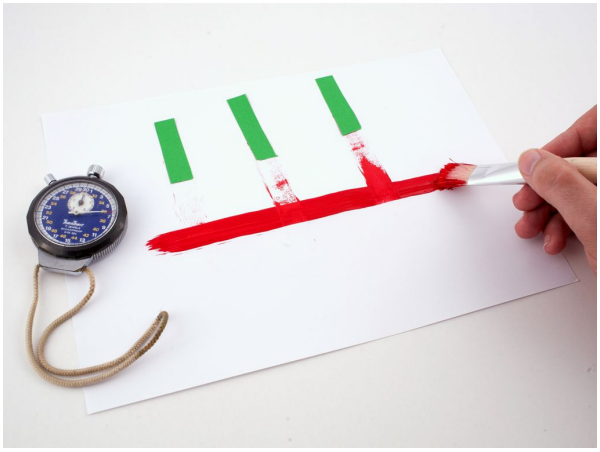

So far, we have not considered the time dependence of our generic depletion mechanism. In reality, depletion will only be possible for a certain time span after the pulsed excitation of the photoresist. For conventional DLW, a photoinitiator can be described abstractly as depicted in Fig. 3.6 (a). The photoinitiator in its initial unexposed state **A** absorbs excitation-laser photons and is eventually transferred to a final state **C** that is irreversibly exposed. To allow for a light-induced depletion process, the photoinitiator has to pass through a vulnerable intermediate state **B** where it can be influenced (see Fig. 3.6 (b)). Upon absorbing at least one depletion photon, the intermediate state should recover to state **A**.[2] This is the criterion for a reversible depletion process.

Directly after excitation, the state **B** is occupied for a lifetime τ. The interruption of the process chain is only possible within this time span. Afterwards, the polymerization process is irreversibly started. This irreversibility is essential as otherwise two crossing lines could not be exposed: During the second line's exposure, the first line would be erased by the co-aligned depletion mode near the crossing point.

The lifetime τ together with the anticipated polymer linewidth imposes a fundamental limitation on the maximum accessible writing speed. Suppose one wants to write lines with $d = 10\,\mathrm{nm}$ feature size with a certain linear scan velocity v using a common donut mode. Clearly, the depletion time-window τ must be closed before the laser foci can be translated by one feature size from a first point written on the line. In case τ had not yet passed, the crest of the translated depletion focus would deplete the exposure of the previous voxel. One may even want a certain safety margin to make sure that the process has really become irreversible. Let us omit this safety margin for now and estimate a very aggressive upper bound for the attainable writing speed v for a certain τ:

$$v \leq \frac{d}{\tau}\,. \tag{3.2}$$

For example, for $\tau = 1\,\mathrm{ms}$ we obtain $v \leq 10\,\mu\mathrm{m/s}$, for $\tau = 1\,\mu\mathrm{s}$ we obtain $v \leq 10\,\mathrm{mm/s}$, and for $\tau = 1\,\mathrm{ns}$ we obtain $v \leq 10\,\mathrm{m/s}$. Today, routine DLW writing speeds are in the range of $100\,\mu\mathrm{m/s}$. The largest speed employed in DLW so far is $190\,\mathrm{mm/s}$ using scanning galvanometer mirrors [71]. Future commercial instruments will likely move towards this value. Thus, depletion time-constants in the ms range are clearly undesired, µs time

[2] To account for all possible depletion mechanisms that we will describe later on, we might need to reinterpret these states as local properties of the whole photoresist system, and not of the photoinitiator alone.

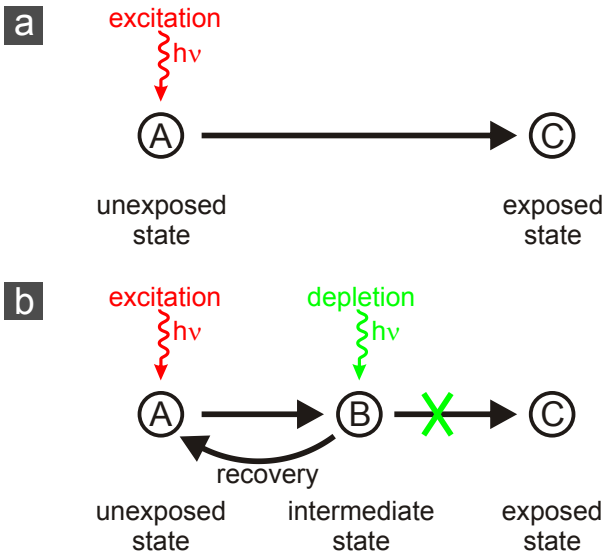

Figure 3.6.: (a) Abstract picture of the states of a photoinitiator/photoresist in conventional DLW. (b) The same, but for depletion DLW approaches. The lifetime τ of the state **B** and the duration τ_{rec} of the "recovery"-transition limit the attainable scan speed.

constants are acceptable but may become borderline in the near future, and ns time constants are compatible with very fast writing.

This discussion seems to favor extremely short depletion time-constants. However, there is a trade-off. The intensity required to deposit a certain energy necessary for the depletion process increases like $I_{\mathrm{depl}} \propto 1/\tau$. Thus, larger intensities are required for small τ, which increases the relative weight of undesired multi-photon absorption of the depletion beam that will likely occur in any photoresist at high intensities. Furthermore, the intensities required for relatively large values of τ may still be accessible with cw depletion lasers, whereas short depletion pulses are required for small τ.

A second important time scale τ_{rec} can arise if the recovery transition from state **B** to state **A** is relatively slow. Actually, not only τ but the sum $\tau + \tau_{\mathrm{rec}}$ truly limits the attainable scan speed. If the two foci would be translated by one feature size before the recovery is completed, the second voxel could not be properly exposed. The unrecovered photoinitiator molecules would not yet be available for a new exposure and the photoresist sensitivity would be decreased.

In case the depletion is mediated by a single electronic transition ($\approx 1\,\mathrm{fs}$) and subsequent vibronic relaxation ($\approx 1\,\mathrm{ps}$), τ_{rec} is of the order of only 1 ps [60]. Some alternative depletion processes to be described in Section 3.6 may, however, have significant values for both τ and τ_{rec}. This may be the case if the recovery itself involves some intermediate states or if the depletion effect is not based on a single molecule but rather on changed local resist properties. The concentrations of competing chemical species (Section 3.6.3) or a local temperature change (Section 3.6.4) are possible examples for slowly-changing resist properties. While the use of large τ can be motivated by inexpensive lasers and little multi-photon absorption of the depletion laser, large τ_{rec} values should be generally avoided.

3.6. Possible depletion mechanisms

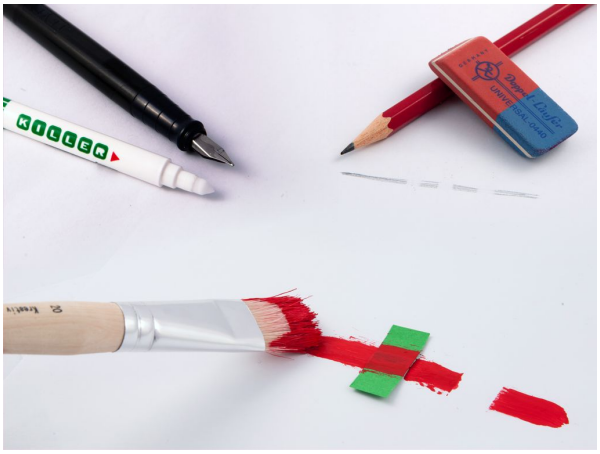

The depletion necessary to enhance the resolution in 3D DLW can be accomplished in different ways. Any photo-induced mechanism that is locally prohibiting the formation of an insoluble cross-linked polymer is suitable at first (see Fig. 3.7 for a list of possibilities). Usually, after photoinitiator molecules are excited by light absorption, a major fraction of the molecules undergoes inter-system crossing (ISC) to a long-lived and reactive triplet state. From this triplet state, initiating radicals are generated that initiate a polymerization reaction. As soon as the polymer is sufficiently cross-linked it becomes insoluble for solvents and the exposure has become irreversible. Any process that disturbs this process chain may serve as a depletion mechanism in 3D DLW.

Figure 3.8 shows photoresist compositions owing a depletion mechanism distinct from STED that have been published by the Fourkas group [66] and the McLeod group [67] in 2009. In the following section, we will elaborate the anticipated properties of different depletion mechanisms. These include STED and the two other mechanisms that have been published meanwhile. We will point out distinct advantages and disadvantages of the different mechanisms and explain why we think STED is still the most promising candidate for future 3D DLW beyond the diffraction limit.

Finally, we will shortly discuss possible alternative mechanisms for an effective polymerization inhibition (Figure 3.7 (d)-(e)). These alternative mechanisms may also interfere with the above intended mechanisms without being recognized and can either amplify or limit their performance.

3.6.1. Stimulated-emission depletion (STED)

In Section 3.1, we have already described the idea of using STED in lithography [60]. In this scheme, photoinitiator molecules are forced to undergo stimulated emission to the ground state after their excitation and before intersystem-crossing takes place (see Fig. 3.7 (a)). This stimulated-emission transition can be induced by the intense light of a depletion laser. The dependence of the depletion efficiency on the depletion power is easily derived when looking at the depopulation channels of the photoinitiator's S_1 state (directly after its population by the excitation pulse). The total depopulation rate constant in absence of a depletion beam is $k_{\mathrm{tot},0} = 1/\tau = k_{\mathrm{fl}} + k_{\mathrm{ISC}} + k_{\mathrm{nr}}$, where τ is the S_1 lifetime state, k_{fl} is the fluorescent rate, k_{ISC} is the intersystem-crossing rate, and k_{nr} is the combined rate of all non-radiative decay channels. The undisturbed intersystem-crossing

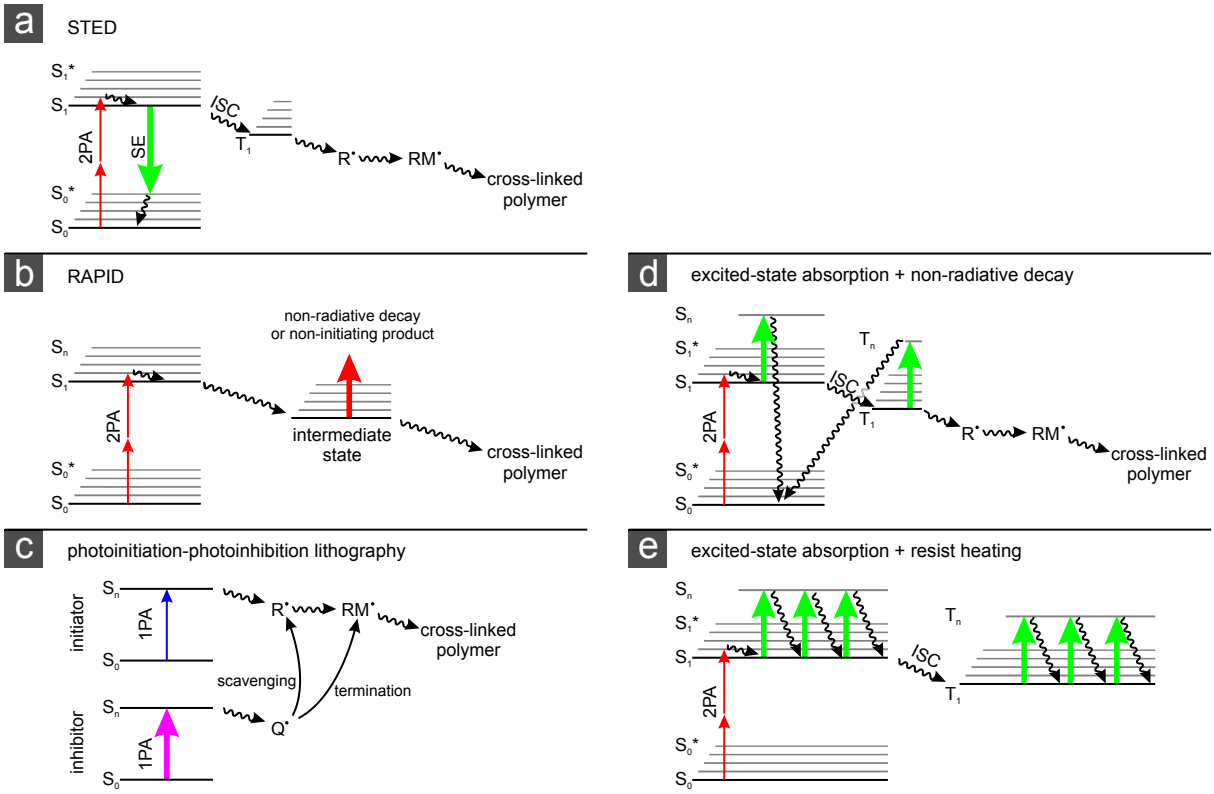

Figure 3.7.: Schematic diagrams of the molecular states and transitions for the different depletion mechanisms in depletion DLW approaches. (a) STED lithography: Photoinitiator (PI) molecules are excited *via* 2PA, relax to the S_1 state and are brought back to the ground state *via* stimulated emission (SE), before they can proceed to the triplet (T_1), generate radicals ($R^{\bullet}$), initiate a propagating polymer chain ($RM^{\bullet}$) and finally yield an irreversibly cross-linked polymer. (b) RAPID: PI molecules are excited *via* 2PA and generate an active species in a long-lived intermediate state. Upon light excitation, the intermediate state is deactivated and does not lead to a cross-linking polymerization. (c) Photoinitiation-photoinhibition lithography: PI molecules are excited *via* 1PA and generate radicals that can initiate the polymerization. Photoinhibitor molecules are activated *via* 1PA at a different wavelength. The generated non-initiating radicals ($Q^{\bullet}$) can scavenge initiating radicals and terminate propagating chains ($RM^{\bullet}$). (d, e) Alternative depletion mechanisms in depletion DLW. (d) Excited-state absorption: After PI excitation, several intermediate states can absorb the depletion light. From such highly excited states, non-radiative decay to the ground state can occur. (e) Resist heating: Through repeated absorption from an excited-state and non-radiative decay to the same state, the resist can be heated and several resist properties can change with the increased temperature, disturbing the excitation, initiation or polymerization process. Previously published in Ref. [55].

quantum-yield is then given by

$$\Phi_{\mathrm{ISC},0} = \frac{k_{\mathrm{ISC}}}{k_{\mathrm{tot},0}} = \frac{k_{\mathrm{ISC}}}{k_{\mathrm{fl}} + k_{\mathrm{ISC}} + k_{\mathrm{nr}}} \,. \tag{3.3}$$

As the chemical reaction proceeds from the triplet state, the effective exposure dose is $D_{\mathrm{eff}} \propto \Phi_{\mathrm{ISC},0}$. When the depletion laser is switched on, stimulated emission k_{STED} is added as depopulation channel for the S_1, and the depopulation now follows $k_{\mathrm{tot}} = k_{\mathrm{fl}} + k_{\mathrm{ISC}} + k_{\mathrm{nr}} + k_{\mathrm{STED}}$. Stimulated emission competes with the intersystem-crossing and the intersystem-crossing yield becomes

$$\Phi_{\mathrm{ISC}} = \frac{k_{\mathrm{ISC}}}{k_{\mathrm{tot}}} = \frac{\Phi_{\mathrm{ISC},0}}{1 + \frac{k_{\mathrm{STED}}}{k_{\mathrm{tot},0}}} = \frac{\Phi_{\mathrm{ISC},0}}{1 + \gamma I_{\mathrm{depl}}} \,, \tag{3.4}$$

where γ is a photoinitiator-specific constant, I_{depl} is the depletion laser intensity, and $k_{\mathrm{STED}} \propto I_{\mathrm{depl}}$ is used. According to this simple model, the intersystem-crossing yield and, hence, the effective exposure dose decreases continuously with increasing depletion intensity. Finally, this leads to an effective exposure dose given by

$$D_{\mathrm{eff}} = D_0 \cdot \frac{\Phi_{\mathrm{ISC}}}{\Phi_{\mathrm{ISC},0}} = D_0 \cdot \frac{1}{1 + \gamma I_{\mathrm{depl}}} \,, \tag{3.5}$$

that we have already introduced in advance (Eq. 3.1). Here, D_0 is the exposure dose for $I_{\mathrm{depl}} = 0$.

Usually, the depletion-laser wavelength is chosen at the red end of the fluorescence spectrum. This is a compromise between moving towards the wavelength of maximum fluorescence (and, hence, towards maximum stimulated-emission cross-section) and avoiding the fundamental absorption band (and, hence, limiting 1PA of the depletion laser).

Advantages and disadvantages:

Compared to other mechanisms to be discussed below, STED offers the fastest time constant, as the lifetime of the S_1 state is typically 0.1 ns - 4 ns [5, 61]. Directly after stimulated emission (and subsequent vibronic relaxation) the photoinitiator molecules are ready for a new exposure. Hence, τ_{rec} is on the order of few ps [5, 60, 61] and therefore $\tau_{\mathrm{rec}} \ll \tau$. This allows for very fast scan speeds in the range of m/s (see Section 3.5), but may require high depletion-laser intensities.

Stimulated emission is also unique among possible depletion mechanisms because it does not inject additional heat into the photoresist, but even ejects energy from the system. Other mechanisms have to be triggered by the absorption of a depletion photon, the energy of which will finally become thermal. In contrast, when using STED, a new photon which contains a major fraction of the initial excitation energy is emitted and leaves the photoresist system.

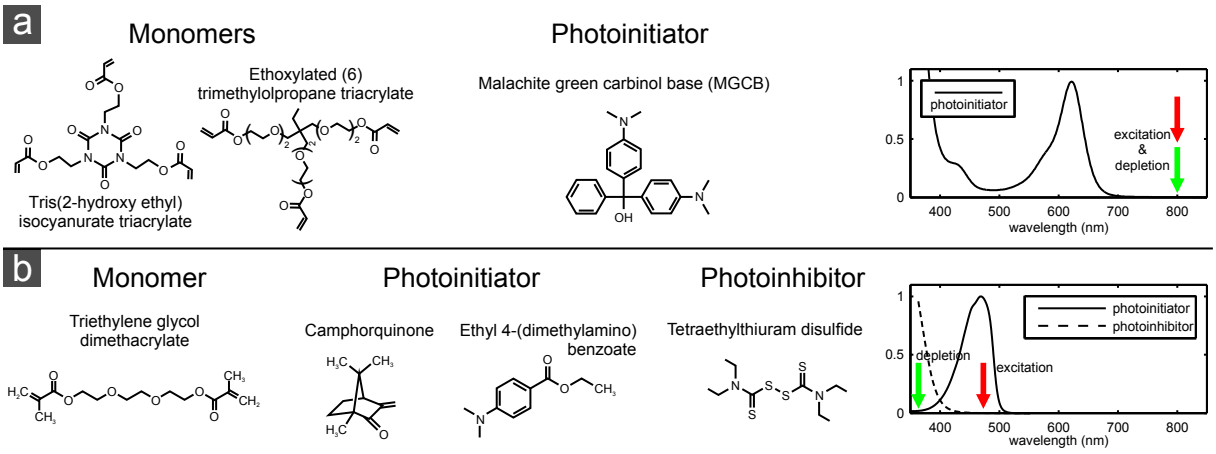

Figure 3.8.: Ingredients of the photoresist systems that provide a photo-deactivation pathway distinct from STED. The resists contain cross-linkable multifunctional monomer(s), a photoinitiator and in one case a photoinhibitor. The relevant (normalized) spectra of the corresponding photoinitiator (and the photoinhibitor) are plotted on the right hand side. The wavelengths used for excitation and depletion used in corresponding lithography experiments are marked with arrows. (a) Resist from Ref. [66] (spectrum for MGCB in ethanol). (b) Resist from Ref. [67] (spectra for photoinitiator and photoinhibitor in $CHCl_3$ [67]). Previously published in Ref. [55].

Although the alternative depletion mechanisms to be described below are less demanding in terms of laser power and pulse timing, we have adhered to the idea of exploiting stimulated emission as depletion mechanism because we feel that it offers the highest future potential and no fundamental limitations.

3.6.2. Resolution augmentation through photo-induced deactivation

In Resolution Augmentation through Photo-Induced Deactivation (RAPID) lithography [66] special cationic dyes (cationic diarylmethanes, cationic triarylmethanes, cationic rhodamines [72]) are used as photoinitiators. The original implementation used malachite green carbinol base (MGCB). Initially, this molecule was expected to support STED and was chosen due to its very high extinction coefficient. MGCB has its fundamental absorption peak at 620 nm, and another shoulder around 430 nm before the absorption rises strongly towards shorter wavelengths (see Fig. 3.8 (a)). Two-photon absorption of femtosecond pulses around 800 nm wavelength is possible and will likely excite the molecule to a higher singlet state S_n followed by non-radiative relaxation to S_1. One would expect further red-shifted fluorescence emission around 700 nm wavelength. Hence, a potential STED depletion could also be performed with 800 nm light. Depletion pulse lengths > 50 ps would ensure that the depletion pulses do not cause efficient 2PA [66]. However, we could not detect any luminescence from MGCB in ethanol solution at the anticipated spectral position for excitation wavelengths between 400 nm and 700 nm.

Indeed, activating the depletion laser can induce an effective polymerization inhibition in MGCB-based photoresists [66]. However, the authors have argued that the observed effect can not be caused by stimulated emission, because the depletion effect is insensitive to pulse delays between excitation and depletion pulses up to 13 ns. They assigned the observed effect to the depletion of an intermediate state with longer lifetime τ (see Fig. 3.7 (b)). This allows for the use of a cw laser for depletion and eliminates the necessity for a precise pulse timing. The exact nature of the intermediate state, however, is yet to be determined [72]. Possibly, these molecules could generate weakly reactive radical pairs [66] or solvated electrons [72] upon excitation. These fragments could recombine to the parent molecules *via* photo-induced electron-backtransfer.

Advantages and disadvantages:

The photoinitiator MGCB absorbs from 400 nm to 700 nm wavelength, *i.e.*, essentially throughout the entire visible spectrum. This fact has to be considered when handling this photoresist to avoid accidental exposures by ambient light. Moreover, remaining unconsumed photoinitiator molecules in the final polymer structures might render these structures absorbing for visible light.

Further investigations have shown that not only MGCB but three broad classes of dyes are capable of being depleted by the RAPID scheme [72]. For example, using malachite green carbinol hydrochloride (MGC-HCl) the depletion effect is so sensitive that even the femtosecond excitation pulses themselves lead to a depletion effect. This manifests itself in an unexpected proportional dependence of the resulting polymer linewidth on the writing speed. Usually, increased scan speeds yield decreased linewidths because the local exposure dose is decreased towards the threshold due to shortened exposure times. In contrast, when using special RAPID photoinitiators, increased scan speeds yield increased linewidths. This is explained as follows [72]: At faster scan speeds, more excited molecules, which are in their vulnerable intermediate state, are left behind the writing spot. These molecules can contribute the chemical reaction undisturbed. At slower scan speeds, the same molecules in the intermediate state would have been partially depleted. This means that for faster scan speed the effective dose increases, because the overall depletion is reduced. This contribution overcompensates the expected decrease in dose due to the smaller exposure time. Combining such photoinitiators (with proportional linewidth scaling) with common photoinitiators can yield a photoresist with nearly scan-speed-independent linewidths [72].

This highly sensitive depletion mechanism allows for low depletion powers and the use of low-cost cw laser diodes as depletion lasers. Low-power depletion is also beneficial because limiting effects (1PA, 2PA, and excited-state-absorption of the depletion laser) are less pronounced. Even wide-field parallel exposures with tailored excitation and depletion patterns to reduce linewidths seem to be in reach [72]. Through multiple exposures, the diffraction limit could again be overcome.

Finally, the proportional linewidth scaling intuitively implies that the lifetime of the vulnerable intermediate state τ and/or the recovery timescale τ_{rec} is at least on the scale

of the effective exposure time used (or even longer). This assumption is in agreement with the numerical modeling in Ref. [72] that implies a depletion time-constant between 15 ms and 350 ms.[3]

This implies that RAPID photoinitiators in general or at least the highly sensitive photoinitiator MGC-HCl in particular are not suitable for fast scanning (see Section 3.5) with confinement along the direction of scanning (*e.g.*, with a lateral donut depletion-focus). However, axial confinement with a bottle beam together with lateral scanning is possible and has been demonstrated [66]. Moreover, a less commonly used depletion focus [61] could be used to only improve the resolution in one lateral direction perpendicular to the scan direction.

3.6.3. Photoinitiation-photoinhibition lithography

A lithography approach based on another depletion mechanism [67] has been named two-color photo-initiation/inhibition (2PII) lithography [73]. 2PII is not based on a direct deactivation of an intermediate excited photoinitiator state but on the activation of a counter-acting photoinhibitor (see Fig. 3.7 (c)) [67]. While the photoinitiator system is allowed to generate initiating radicals upon 1PA, the additional photoinhibitor is activated by 1PA at a different wavelength (see Fig. 3.8 (c)). The latter cleaves into two weakly reactive radicals which can efficiently scavenge the initiating radicals and also terminate propagating radical polymer chains. Ref. [67] has shown that this mechanism can reduce the polymerization rate by up to a factor of 5. Thus, for a fixed exposure time T, the mechanism can prevent the formation of a cross-linked insoluble polymer network.

The spectra of the compounds have to be chosen such that they can be excited separately with little cross-talk. In the original implementation of 2PII, a photoinitiating system consisting of camphorquinone and ethyl 4-(dimethylamino)benzoate is used and excited at 473 nm wavelength near its absorption peak (see Fig. 3.8 (c)). The activation of the photoinhibitor (tetraethylthiuram disulfide) is performed with 364 nm radiation, where the photoinitiator has an absorption minimum (see Fig. 3.8 (c)).

Advantages and disadvantages:

The use of 1PA has distinct advantages and disadvantages. In the original implementation of 2PII, 1PA is used for the excitation of both the initiator and the inhibitor. This results in very low power requirements in the 10 µW range that can easily be delivered by low-cost cw laser diodes. In contrast, two-photon absorption usually demands for 100 fs pulses with < 10 mW average power that can be readily delivered by fs-fiber oscillators, yet at a cost more than ten times higher.

[3] In Ref. [72], a decay time of around 1000 time units and exposure times between 20 and 50 time units (corresponding to 0.05 and 0.02 velocity units) were used to successfully model the observed proportional linewidth scaling. We deduce exposure times of 1–7 ms from Fig. 2 (j) of Ref.[72]. These correspond to the used writing speeds of 30 µm/s to 150 µm/s and a diffraction-limited excitation spot with a lateral intensity FWHM of 310 nm.

One drawback of 1PA is that it is difficult if not impossible to fabricate complex 3D structures – even if the photoresist offers sufficient nonlinearity to provide 3D operation without two-photon absorption (see Section 2.1.2). When focusing deeper into the photoresist volume, both the excitation and depletion light is attenuated on its way through the absorbing material. Hence, the laser powers to be applied are strongly depth-dependent. Furthermore, this can lead to a consumption of the initiator and/or inhibitor and to a continuous heating of the photoresist inside the complete cone of the focused laser beams. In contrast, using 2PA for excitation, the laser light is only absorbed within the focal volume. In addition, using STED, the depletion light is also exclusively absorbed by molecules in their intermediate state (hence, within the focal volume). Thus, the laser powers to be applied are rather depth-independent, the anticipated photoresist heating is much less pronounced, and no consumption of one species is expected.

Applying 2PA to both the photoactivation and the photoinhibition in 2PII would resolve these obstacles and provide full 3D capability. In this case, the depletion laser would likely be centered around 800 nm wavelength (*i.e.*, twice the wavelength of the 1PA maximum). Unfortunately, the shape of the minimum of a donut mode gets much broader (and hence less attractive for depletion DLW) when the intensity profile is squared (see, *e.g.*, the minima in Fig. 2.7 for comparison).

In contrast to the above approaches, 2PII does not only confine the effective excitation but also directly tackles the blurring of the excitation pattern due to diffusion of initiating and propagating radicals. Once those species diffuse out of the anticipated polymerization volume, the probability of their termination increases. Especially in low-viscosity photoresists with pronounced diffusion of the active species, this unique feature can be a major advantage.

To apply the state model presented in Section 3.5 to 2PII we have to reinterpret the states of the photoinitiator molecules as local properties of the photoresist. The lifetime τ of the vulnerable intermediate state between the initial excitation and the final irreversible state can be identified with the time the photoresist needs to form an irreversibly crosslinked polymer network. This time is heavily depending on the photoresist. We estimate a timescale between 1 ms and 100 ms. The time for the recovery of the photoresist τ_{rec} is determined by the lifetime of the activated inhibiting radicals. Once the depletion light is switched off, these can recombine and again form the initial parent molecule. The recombination reaction can be very fast, depending on the viscosity of the photoresist formulation (which affects the diffusion speed) and on the concentration of the activated inhibitor (as the recombination is bimolecular). The concentration and, hence, the time constant, changes throughout the depletion profile. For tetraethylthiuram disulfide in low-viscosity acetonitrile, Plyusnin *et al.* [74] have determined a recombination time-constant around $\tau_{\mathrm{rec}} = 2\,\mu\mathrm{s}$. This value likely provides a lower bound. Kowalski *et al.* [75] have estimated an upper bound of $\tau_{\mathrm{rec}} = 200\,\mathrm{ms}$ for the same photoinhibitor in a higher-viscosity photoresist. As $\tau + \tau_{\mathrm{rec}}$ can obviously reach the ms range, fast scanning with confinement along the direction of scanning may not be possible using 2PII (see Section 3.5).

3.6.4. Alternative depletion pathways

Historically, some authors had speculated that the fluorescence depletion effect in STED microscopy might actually not be caused by stimulated emission but rather be mediated by excited-state absorption [76]. Although it turned out that STED is the far dominating mechanism in STED microscopy, the proposed processes can still play an important role in depletion lithography. The corresponding processes for lithography are illustrated in Fig. 3.7 (d, e). Excited-state absorption might take place directly from the S_1 state or, alternatively, from the triplet. Even the generated radicals might absorb depletion light and contribute (not depicted in Fig. 3.7). Following light absorption, the highly excited molecules might immediately relax non-radiatively to the ground-state (Fig. 3.7 (d)) in which case their contribution to the exposure dose would be effectively lost.

In another conceivable mechanism, molecules are excited several times from an excited state and quickly relax to the same excited state non-radiatively (see Fig. 3.7 (e)). In this case, significant heat might be imposed onto the system and thermal effects could play the dominant role. For example, the 2PA cross-section of a molecule can decrease considerably with increasing temperature (*e.g.*, 50% reduction from 20°C to 110°C for Disperse Red 19 [77]). In this case, the depletion laser might quickly heat up the exposure volume, subsequent excitation pulses would find photoinitiator molecules with reduced 2PA cross-sections, and the effective exposure dose would drop below threshold. Alternatively, the intersystem-crossing quantum-yield might also decrease with increasing temperature due to temperature-dependent non-radiative decay from the S_1 state. Further mechanisms are conceivable as well.

Such temperature-mediated mechanisms might lead to fairly low depletion-power requirements, as the lifetime of the absorbing intermediate states τ can be rather long (in case of T_1 state or a transient radical absorptions). However, the corresponding recovery time-constants τ_{rec} are likely in the range of many µs to ms, which would significantly limit the accessible depletion-DLW writing-speeds (see Section 3.5).

Broadly speaking, when aiming at better and better resolutions, large laser intensities will be required. Any sort of absorptive process will eventually introduce heat into the system and may lead to (unwanted) temperature-dependent effects. In contrast, stimulated emission carries energy out of the system (see Section 3.6.1). This fact alone might render STED superior over alternative mechanisms in the future.

4. Experimental methods

4.1. STED-inspired lithography setup

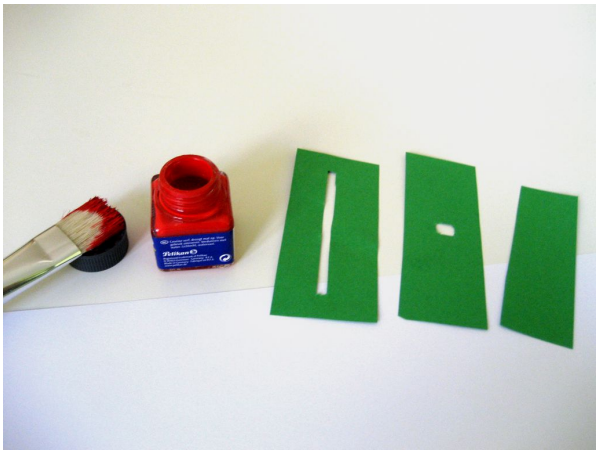

In this section, we will describe the experimental setup that was designed, built, and used throughout this work. It basically consists of a standard DLW setup with an additional beam path for depletion. Furthermore, the setup allows for the measurement of the focal intensity distribution (Section 4.2) and spectrally resolved fluorescence measurements (Appendix A.1).

Figure 4.1 is a simplified illustration of this setup. Mirrors, wave plates, and telescopes that are not necessary for the basic understanding, have not been depicted. The heart of the setup is a femtosecond Ti:sapphire oscillator (SpectraPhysics MaiTai HP) operated at 810 nm center-wavelength. The laser emits 100 fs pulses with a repetition rate of 80 MHz. Such near-infrared fs-oscillators are very common choices in two-photon DLW. The laser is first manually attenuated using a half-wave plate and a polarizer (not depicted). An acousto-optic modulator (AOM) (AA MTS40-A3-750.850) is used to fine-adjust the transmitted laser power during writing. Instead of a fast shutter, we use the AOM to switch the writing beam on and off (*e.g.*, when aiming at writing interrupted lines). In our setup, the first diffraction order of the AOM is used while the zeroth order is blocked (not depicted). For optimal diffraction efficiency and mode quality after the AOM, the beam diameter before the AOM is reduced to roughly 1 mm using a Kepler telescope (not depicted).

After the modulator, the beam is expanded such that it eventually overfills the objective's entrance pupil by a factor of two in diameter (see Section 2.2.2). At this point, we have introduced a mirror in a motorized mount (New Focus 8807 Picomotor Center Mount) that can be used to adjust the beam angle (and, hence, the lateral focus position within the sample) in a computer-controlled fashion. Next, the excitation beam is reflected off of a dielectric beam splitter (AHF 700DCSPXR) and coupled into the back port of a modified commercial inverted microscope (Leica DM-IRB). Here, we have introduced a Kepler telescope that images the plane of the motorized mirror onto the entrance pupil of the objective lens. This allows for an adjustment of the angle under which the beam hits the objective lens (and hence the lateral position of the excitation focus in the sample) without the beam walking off the entrance pupil (which would yield a tilted focus).

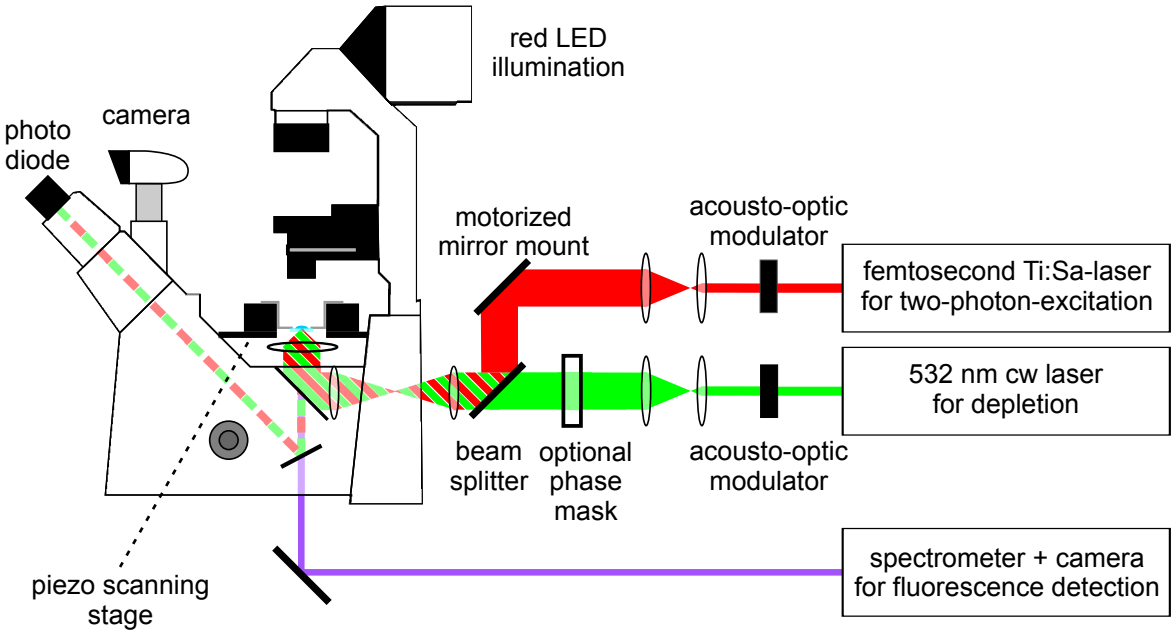

Figure 4.1.: Simplified illustration of the experimental setup for STED-inspired DLW.

The original Leica beam splitter inside the microscope is replaced by a dielectric beam splitter (AHF zt532rdc_R725-1070) that reflects both the excitation and the depletion laser. Finally, the excitation laser is circularly polarized by means of an achromatic quarter-wave plate (B. Halle RAC 4.4.15L, 500-900 nm) and focused into the sample through a high-NA oil immersion lens (Leica HCX PL APO 100×/1.4-0.7 OIL CS) . The circular polarization is used to attain polymer voxels that are rotationally symmetric with respect to the optical axis (see Section 2.2.2). Unless stated otherwise, all laser powers quoted in the remainder of this thesis are average-power values and measured at the position of the objective lens. The objective is removed and an aperture of the same diameter (5.6 mm) is inserted. Hence, the measured powers correspond to the powers entering the objective lens' entrance pupil. According to the manufacturer, the objective transmission at 532 nm and 810 nm wavelength is 86% and 68%, respectively.

In addition to the common writing laser, our setup features a green cw laser (Spectra-Physics Millenia X) at 532 nm wavelength for depletion. Like the writing beam, this additional beam is manually attenuated, demagnified, and modulated with an AOM (AA MQ110-A1.5-VIS-WLG). After modulation, the beam is expanded such that its diameter eventually matches the pupil diameter. Thereafter, an optional phase mask can be introduced into the beam path. Without any phase mask, focusing the Gaussian beam would yield an usual Gaussian-like focus. Upon using a vortex phase mask or a circular phase mask the focus shape changes to a donut mode or a bottle-beam focus, respectively (see Section 3.2).

The depletion beam is transmitted through the dielectric beam splitter and from there on shares its path with the excitation beam. The telescope images the phase mask plane onto the entrance pupil of the objective lens. Diffraction at the phase discontinuities of the

phase masks usually obscures the beam profile with interference fringes. When imaged to the objective lens plane, these fringes are strongly reduced because diffracted light is collected by the imaging system and imaged back to its original transversal beam position. Finally, the depletion beam is also circularly polarized by the above achromatic quarter-wave plate. For a Gaussian focus and for a bottle-beam focus, the circular polarization leads to a cylindrically symmetric $\langle|\vec{E}^2|\rangle$-distribution. In case of a donut focus, the circular polarization is essential to generate the interferometric zero in the center. Choosing linear polarization or circular polarization of the wrong handedness would destroy the zero and is, hence, not suitable for depletion DLW.

A precise co-alignment of the two beams is very important to guarantee spatial overlap of the two corresponding laser foci. A first coarse alignment is performed directly by using apertures or white cards. A precise co-alignment is performed using the focus measurement routine described in the next section. Usually, this precise alignment has to be confirmed or repeated on a daily basis. This is mainly due to thermal drifts of the involved components. Using the motorized mirror mount, a relative position accuracy on the order of 10 nm is usually achieved within the focal plane. This corresponds to 5 µrad angular precision between the two collimated beams.

The above-mentioned beam splitter inside the microscope reflects the excitation and depletion laser light with roughly 98% efficiency. At the same time, it transmits the counter-propagating light of a light-emitting diode (LED) with near-unity efficiency. This LED serves as illumiation at around 630 nm wavelength yielding a bright-field image on the camera (Leica DFC 350FX). Furthermore, the beam splitter transmits parts of the fluorescence emission anticipated from photoinitiator molecules within the sample. This emission is generally expected to be red-shifted with respect to the fundamental absorption band at 810 nm/2 = 405 nm, *i.e.* between 400 nm and 600 nm. The beam splitter transmits wavelengths between 400 nm and 500 nm with reasonable efficiency. The light originating from fluorescence emission within the sample is guided to a spectrometer (Jobin Yvon HR460) with a liquid-nitrogen-cooled silicon CCD camera (Princeton Instruments LN/CCD 1340/100-EB/1) attached to it. An aluminum-coated grating with 600 grooves/mm and blazed for 500 nm wavelength was used. The nominal diffraction efficiency of the grating for wavelengths between 400 nm and 500 nm is >80% for p-polarized and between 68% and 86% for s-polarized light.

In case some portion of the laser light is reflected or back-scattered from the sample and collected through the objective lens, roughly 2% of this light will also be transmitted through the internal beam splitter. This light is guided to a silicon photodiode located at the ocular position. This photo-diode is used to measure the focal intensity distribution as described in the following section.

The sample is mounted on a piezoelectric scanning stage (Physik Instrumente P-527.3CL) which is mounted on a motorized stage (Märzhäuser Wetzlar, SCAN IM 120 x 100). The former allows for the precise scanning of the sample in all three dimensions. The accessible displacement ranges in the x, y, and z-directions are 200 µm, 200 µm, and 20 µm, respectively. Throughout this thesis, the z-direction refers to the optical axis, while the x and y refer to transversal directions. The motorized stage allows to translate

the sample in the lateral directions by 120 mm and 100 mm, respectively. In this way, samples containing many different structures or test patterns can be created and extensive parameter sweeps are easily realizable on a single sample.

Finally, the whole experimental setup is controlled by a PC and a home-made software written in Labview and Matlab. Analog input and output channels are provided by the National Instruments PCI-Cards NI-6731 and NI-MIO-16XE-10. The piezoelectric stage and the RF-drivers for the AOMs are controlled *via* analog voltage signals. The stepper-motor stage is controlled using a dedicated PCI controller-card. The motorized mirror mount and the parameters of the spectrometer (grating angle, slit width) are controlled *via* RS-232. The camera attached to the spectrometer is read out through a dedicated PCI controller.

4.2. Focus-engineering and characterization method

For an experimentalist, it is important to not only know the shape of the used foci in theory but also to verify these shapes by means of a measurement. In this way, aberrations of the beam and imperfections of the alignment can be identified. When using two laser beams it is even more important to know the exact displacement between the two corresponding foci in three dimensions. If the foci do not overlap properly, the obtained experimental results are hard if not impossible to interpret.

For this purpose, we have implemented a procedure to measure the focal intensity distributions of the two lasers. We use single gold spheres with a diameter of 80 nm as nearly-point-like probes in the focus and measure the back-scattered light intensity (see Fig. 4.2). These spheres are spin-coated onto a standard glass cover-slip out of an aqueous dispersion. After the evaporation of the water, the gold beads on the glass surface are covered with the monomer pentaerythritol triacrylate that we will later use in our photoresists. In this way the beads are embedded in the refractive index as the photoresist will later have. Moreover, this refractive index ($n = 1.484$ [78]) is relatively close to the one of the substrate, such that Fresnel reflections from the glass-monomer interface are expected to be weak. In contrast, for a glass-air interface one would expect stronger reflections that would add a large offset to the weak scattering signal of the individual gold particles.

The backscattered light is detected using a simple silicon photodiode (Thorlabs FDS100) together with a home-built current-voltage-converter. We use a lock-in amplifier (Stanford Research Systems SR830 DSP) and chopped laser beams to improve the signal-to-noise ratio and to remove contributions from ambient light. For this purpose, both laser

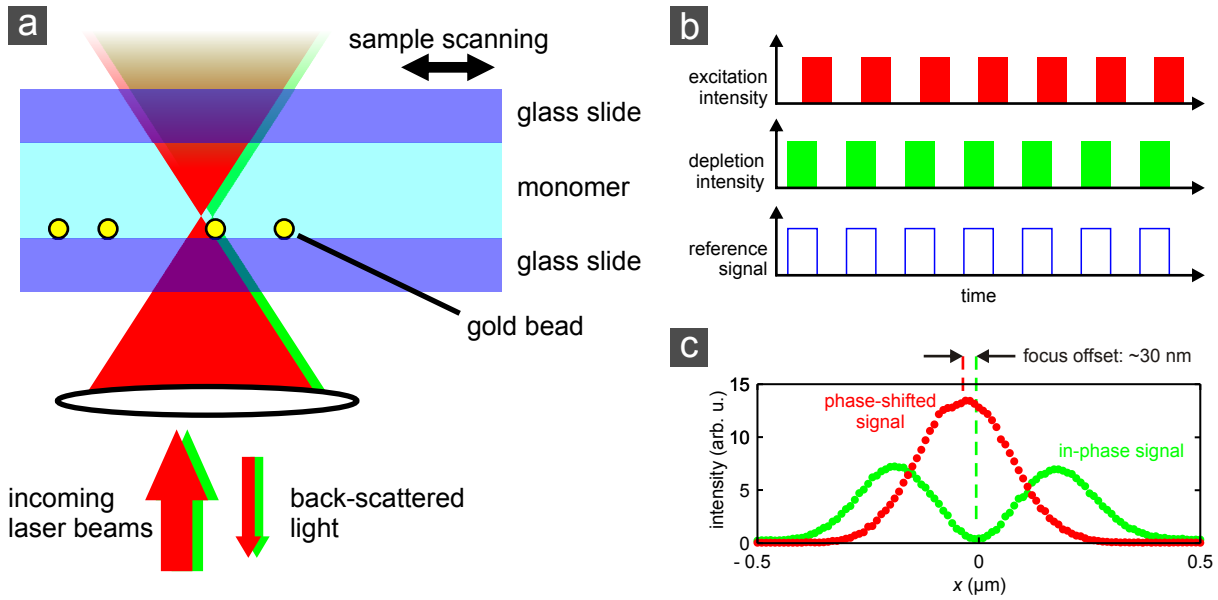

Figure 4.2.: Illustration of the focus characterization procedure for two beams with a small spatial offset. (a) Both laser beams are focused into a test sample in which gold beads are dispersed on a glass slide and embedded in a monomer. Back-scattered light is collected through the same lens and detected with a silicon photodiode using a lock-in amplifier. (b) Modulation scheme: Both lasers are modulated with acousto-optic modulators. A 4 kHz square wave is used. The depletion laser is modulated in phase to an electronic reference signal, the excitation laser is modulated with 90° phase shift. (c) Typical measured signal for a lateral line scan of a single bead through the overlapping foci (Gaussian excitation, donut depletion) using a 100 nm gold bead. Due to the phase modulation, both signals can be measured at the same time with a single detector. After fitting these data (not shown), a relative focus shift can be determined, usually with an accuracy of 10–20 nm.

beams are modulated by means of acousto-optic modulators. A reference signal of 4 kHz frequency is generated by the lock-in amplifier itself (see Fig. 4.2 (b)). Two arbitrary-function generators (Hewlett Packard 33120A) are triggered by this signal and generate synchronous square waves that are fed to the RF-drivers for the acousto-optic modulators described in the previous section. In this way, the laser beams are synchronously chopped in a square-wave fashion.

It is convenient to introduce a phase shift of 90° to the periodic modulation pattern of one of the beams. This can be done electronically using the arbitrary-function generators. In this way, the lock-in amplifier can discriminate between the contributions of the both lasers, as one is in phase and the other one is phase-shifted with respect to the reference signal. The back-scattered signal of both lasers can therefore be acquired at the same time with a single detector and without any optical spectral filtering. An exemplary data set corresponding to a single line scan is depicted in Fig. 4.2 (c). Here, the gold particle was scanned with constant velocity along the x-axis while the two analog outputs of the lock-in amplifier (corresponding to in-phase and out-of-phase contributions) are recorded with the control PC.

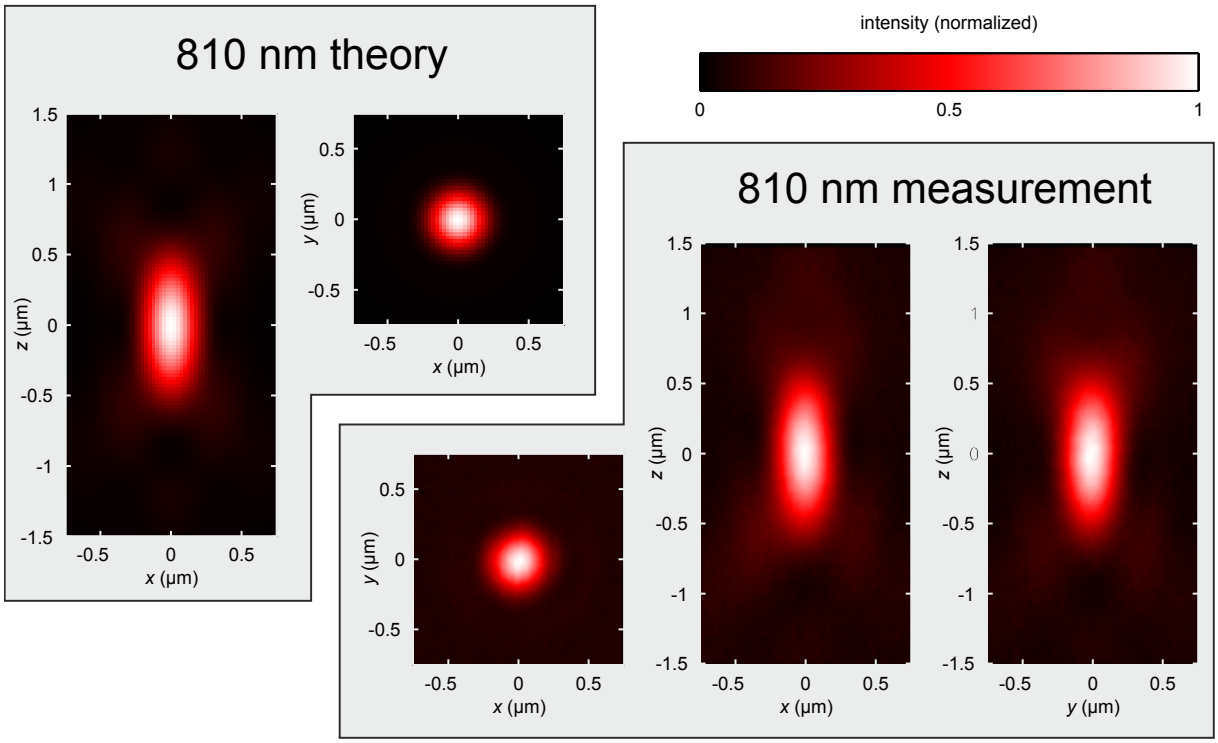

Figure 4.3.: Focal intensity distribution of the excitation laser. Left side: calculation according to Section 2.2.1. Right side: measurement by scanning a 80 nm gold bead through the focus.

We fit analytic functions to the obtained data (not depicted) and deduce a spatial displacement of the two foci out of the fit parameters. Usually, the repeatability of this value is in the range of 10–20 nm. By repeating this procedure for all three axes, we can measure the focus displacement in three dimensions. We use the computer-controlled mirror mount within the excitation beam path to iteratively correct for the lateral offset. An axial offset can be corrected by changing the beam collimation. For this purpose, we translate the second lens of the excitation-laser beam-expander telescope along the beam direction. For the lateral as well as the axial corrections, we move the excitation focus and leave the depletion focus fixed. In this way, the quality of the special depletion foci, that we will use, is not affected by the alignment procedure.

A major benefit of the simultaneous acquisition scheme exploiting a phase-shifted modulation is that the measured displacements between the two foci are completely insensitive to drifts of the sample and/or gold particle. Especially directly after the sample is exchanged, pronounced drifts in all spatial directions can be observed. In case the line scans for the excitation and depletion laser would be acquired sequentially, one would need to wait for these drifts to decay. Usually, this can take from tens of minutes to hours. For the simultaneous acquisition, however, the determined overall positions may drift, the relative positions (and therefore the alignment corrections performed with the motorized mirror) are always accurate.

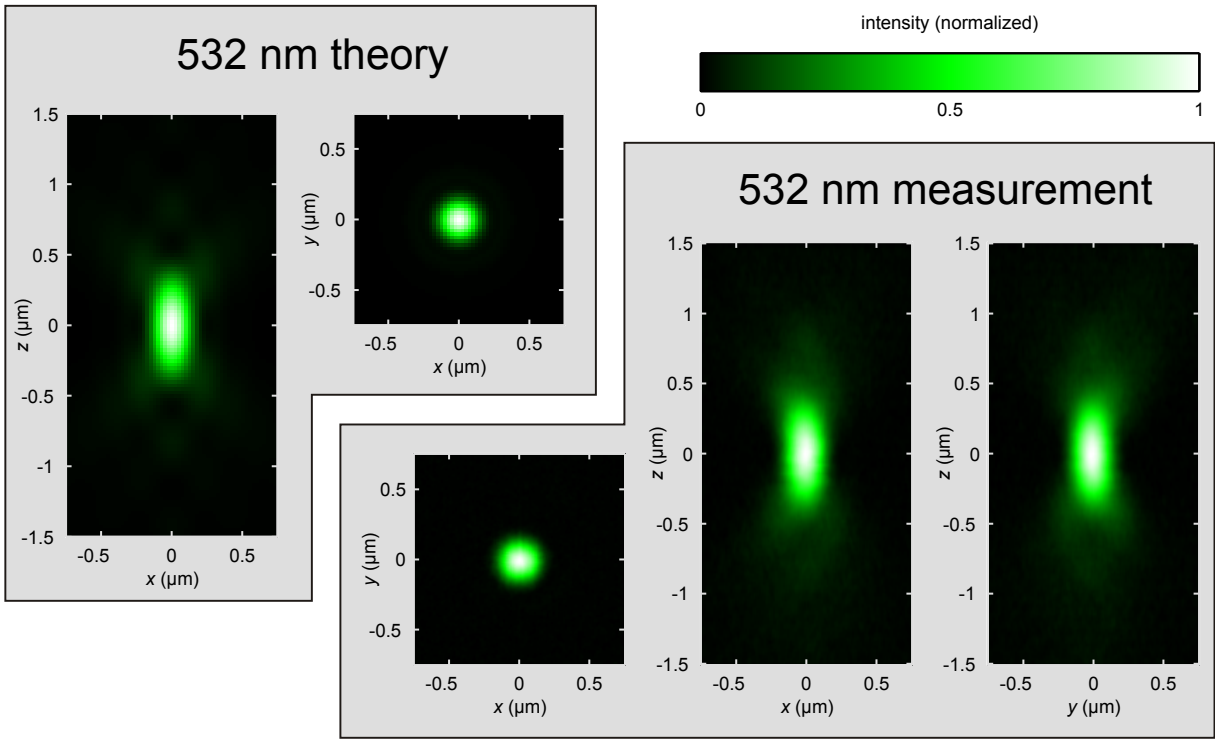

Figure 4.4.: Focal intensity distribution of the depletion laser without any phase mask inserted. Left side: calculation according to Section 2.2.1. Right side: measurement by scanning a 80 nm gold bead through the focus.

Besides performing line scans that enable a proper alignment of the beams, this method can also be used to create 2D or 3D data sets of the focal intensity distribution. Exemplary two-dimensional scans along the principal planes of the focal volume (the lateral x-y-plane and the two axial x-z- and y-z-planes) are depicted in Fig. 4.3 and Fig. 4.4 for wavelengths of 810 nm and 532 nm respectively.

Both figures show numerical calculations on the left hand side (compare Section 2.2.1) and the corresponding measurements on the right hand side. As the calculated distributions are rotationally symmetric around the optical axis, we only show one slice along the optical axis. Experimentally, we measure both the x-z-slice and the y-z-slice to confirm this symmetry.

Usually, we observe a constant signal-offset that is caused by Fresnel reflections of the incoming laser beam at the substrate-monomer interface and by reflections off of the achromatic wave plate inside the microscope. To remove this offset we subtract the smallest value of each slice. The measured values are averaged over an interval of 30 nm in the lateral directions and 60 nm along the axial direction to decrease measurement noise.

As shown in Fig. 4.3, theory and experiment for the excitation laser are in excellent agreement. This means that our starting point in conventional DLW will be optimal and that our setup does not suffer from heavy aberrations that would decrease the anticipated

resolution. When looking very closely, there seems to be a remaining weak astigmatism in the excitation beam as the lower part of the x-z-profile and the upper part of the y-z-profile seem to be a little broader. As mentioned, the focus should be rotationally symmetric and even symmetric with respect to the focal plane in theory.

For the depletion laser, theory and experiment also agree very well. Here, an aberration-free Gaussian focus is a paramount starting point for the successful generation of donut modes and bottle beams. When again looking very closely, one can see slight deviations from the rotational symmetry in the x-z- and y-z-slice. While the calculation is performed for a homogeneous illumination (corresponding to an infinite beam diameter), the actual beam diameter of the depletion beam was roughly the objective's pupil diameter. The effect of this discrepancy is visible above and below the main peak. While the calculated intensity distribution has a local minimum between the main peak and the two side-lobes above and below, the measured distribution shows no pronounced minimum but some sort of pedestal above and below the main peak. This compares well to our previous analysis of the beam-diameter influence (compare Fig. 2.6 (a), (c), and (e)).

5. The materials challenge in sub-diffraction lithography

5.1. Switching off the photopolymerization

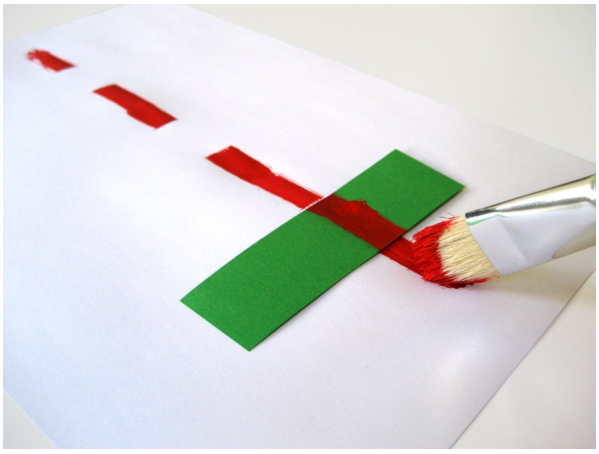

So far, the concept of using STED in DLW sounds very reasonable and one would have guessed it is easy to implement. It turns out, however, that common photoinitiators sensitive to UV light are not at all suitable for STED. The following section describes the shortcomings of common photoinitiators and the requirements on proper photoinitiators for STED lithography. During our extensive search for a STED photoinitiator, we have also discovered a second mechanism distinct from STED that can lead to an effective suppression of the polymerization and, hence, can be utilized for super-resolution lithography.

5.1.1. Common photoinitiators do not work

To test and compare different photoinitiators, we mix different photoresists with a simple fixed recipe. We use the monomer pentaerythritol triacrylate (PETA) as a basis. This monomer contains 300-400 ppm monomethyl ether hydroquinone as inhibitor. The monomer (technical grade) is purchased from Sigma Aldrich and used as received, *i.e.*, without purification or de-inhibition. We add the different photoinitiators at concentrations between 0.1% (wt) and 2% (wt) to this monomer. Examples for common UV photoinitiators that we have tested are Irgacure 369, Irgacure 819, Irgacure 1800, Darocur TPO, Benzil, 4-(Diethylamino)benzophenone, and 4,4'-Bis(diethylamino)benzophenone. The first three photoinitiators were samples provided by Ciba Specialty Chemicals (now part of BASF), the remaining ones were purchased at Sigma Aldrich and used as received.

Representative absorption and photoluminescence spectra are depicted in Fig. 5.1. These spectra for Irgacure 1800 and Irgacure 810 were taken in ethanol solution using a commercial UV-VIS spectrophotometer (Varian Cary 300 Scan) and fluorescence spectrophotometer (Varian Cary Eclipse). The excitation wavelength for the photolu-

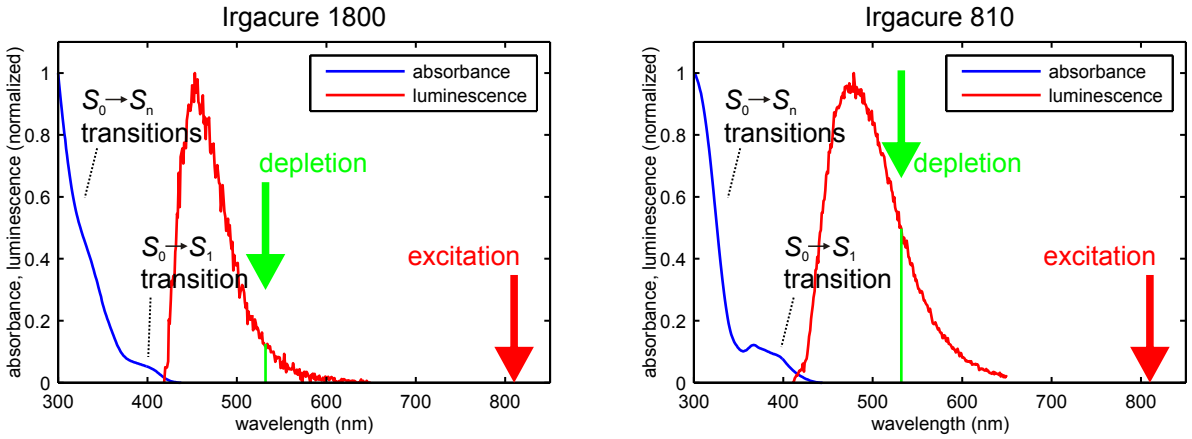

Figure 5.1.: Absorbance and photoluminescence spectra of two typical UV photoinitiators. Important properties for two-photon DLW: No absorption at the two-photon-excitation wavelength (810 nm), finite absorption at half of that wavelength (405 nm). Weak luminescence (presumably fluorescence) is detected. Important property for STED: The depletion wavelength is at the red end of the fluorescence spectrum. Due to small spatial overlap of the corresponding orbitals, the absorption peak corresponding to the $S_0 \rightarrow S_1$ transition is very weak, often not visible at all. Higher $S_0 \rightarrow S_n$ transitions possess much higher oscillator strengths corresponding to more pronounced (overlapping) absorption peaks at shorter wavelengths.

minescence measurements on Irgacure 1800 and Irgacure 810 was 350 nm and 380 nm, respectively.

When looking at the spectra, we see that there is hardly any absorption observed above 420 nm wavelength. This is important, because 2PA can only be utilized if the material is transparent for 1PA at the laser's wavelength. In our case, this is 810 nm where all common photoinitiators (and monomers) are transparent. Following the principles of STED microscopy, one would look for fluorescence from these compounds and place the depletion-laser wavelength at the red end of the fluorescence spectrum to avoid unwanted 1PA of the depletion laser. As our depletion laser has a fixed wavelength of 532 nm, we have to choose the photoinitiators carefully so that the spectra match this depletion-laser wavelength. As depicted in Fig. 5.1, these common photoinitiators usually show some weak photoluminescence that is likely fluorescence. However, we can not exclude that we see phosphorescence ($T_1 \rightarrow S_0^*$) here, as the fluorescence spectrophotometer is not sensitive to a time lag between excitation and luminescence. Assuming it is fluorescence indeed, the depletion-laser wavelength is appropriate for efficient STED.

The simplest test of the anticipated depletion effect is to switch the photopolymerization reaction off and on by switching the depletion laser on and off. For this purpose, we use two Gaussian foci for excitation and depletion as depicted in the previous section. As the depletion wavelength is shorter than the excitation wavelength also the corresponding focus is smaller. This seems unfavorable, because only the inner part of the excitation volume would be depleted. The excitation, however, is accomplished by two-photon absorption and therefore the squared intensity is relevant for the excitation distribution.

While the lateral FWHM of the excitation intensity is roughly 330 nm, the FWHM of the excitation profile is $\approx 330\,\text{nm}/\sqrt{2} = 233\,\text{nm}$. The depletion focus FWHM is of the same order, roughly 220 nm. With this configuration, we write simple test lines into the different photoresists directly at the substrate-resist-interface. We use a fixed scan speed of 100 µm/s but vary the excitation power and depletion power systematically. The samples are developed for 10 minutes in isopropanol and rinsed in acetone and water. Afterwards, they are characterized by optical microscopy and/or scanning electron microscopy.

The expectation for a depletion mechanism would be the following: If we write a line with the excitation laser and then switch on the additional co-aligned depletion laser at the appropriate power level for a short time, the resulting line should be interrupted. The photopolymerization reaction would have been suppressed for the time the depletion laser was switched on. A less digital observable is a shift in polymerization threshold. The polymerization-threshold power is the smallest excitation power (for a fixed scan speed) that yields polymerized lines. For yet smaller excitation powers, the resist is not sufficiently exposed and these regions are washed out during development. If the depletion laser reduces the photopolymerization to some extent, one would expect the polymerization-threshold power of the excitation laser to rise. The increased excitation power would lead to an increased production of initiating radicals and could compensate for the depletion effect induced by the depletion laser.

Against these clear expectations, the exact opposite behavior is observed for all the above listed photoinitiators. Switching on the depletion power does not have any effect at low power levels. When increasing the depletion power, the polymerization threshold actually increases. This means that the depletion laser does actually not deplete anything, but even leads to enhanced initiation and/or polymerization. Above a certain depletion-power level (typically between 50 mW and 100 mW), the green laser alone leads to a photopolymerization. This is very surprising, as one would not expect 2PA from a cw laser. Moreover, 1PA is also very unlikely, as the fundamental absorption band of the photoinitiators used is far away from depletion-laser wavelength. The monomer itself is also transparent in the visible. As a sanity check we have repeated the experiments with the pure monomer (*i.e.*, without any photoinitiator). No polymerization is observed, neither for the excitation laser nor for the depletion laser. Above roughly 60 mW average excitation power, we observe uncontrolled explosions within the resist. This is likely also an upper bound for the applicable excitation-power in the actual photoinitiator-containing photoresists.

These parasitic absorption processes of the cw depletion laser are observed with all photoinitiators, even with the STED-DLW photoinitiators to be described in the following sections. Clearly, this will be a limiting factor for STED-DLW. Interestingly, this "unwanted" absorption can be utilized for DLW with cw lasers. Due to the rather short wavelength, the resolution can be very good (depending on the photoresist). This method is very simple, inexpensive, and works with many commercial photoresists. As a side-project, we have published a corresponding paper [79] describing this new cw-DLW approach during the course of this thesis. While we could neither prove nor rule out 2PA as the underlying absorption mechanism, the examined photoresists definitely show a non-linear overall response that allows for 3D structuring using cw exposure [79].

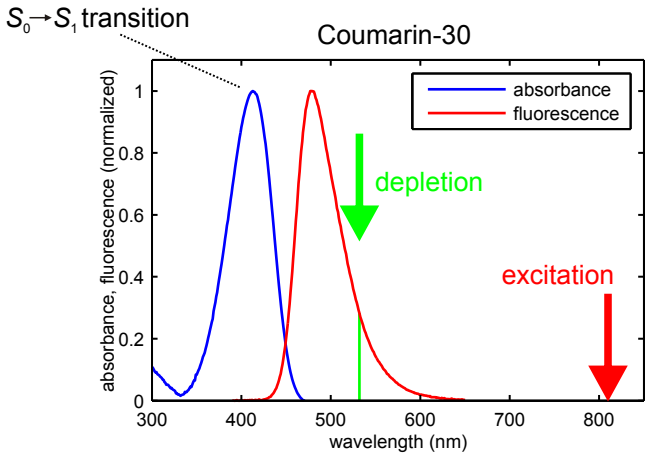

Figure 5.2.: Absorbance and fluorescence spectra of the fluorescent dye Coumarin-30. Note the pronounced $S_0 \rightarrow S_1$ transition. The mirror-image fluorescence-spectrum indicates that the absorption peak stems from the $S_0 \rightarrow S_1$ transition alone. The absorption peak is well separated from absorptions to higher S_n states.

5.1.2. Requirements for STED photoinitiators

Now knowing that common photoinitiators do not work in our simple cw-depletion scheme, let us elaborate a set of requirements for photoinitiator candidates that could do the job. It is reasonable to compare the optical properties of the photoinitiator molecules to those of fluorescent dyes that are successfully used in STED microscopy. The spectra of the common fluorescent dye Coumarin-30 dissolved in ethanol are depicted in Fig. 5.2 for comparison.

Oscillator strength:

The rate for stimulated emission is given by $k_{\mathrm{STED}} = \sigma_{\mathrm{SE}} I_{\mathrm{depl}}/(h\nu)$, where σ_{SE} is the cross-section for stimulated emission, I_{depl} is the depletion-laser intensity, and $h\nu$ is the energy of one depletion photon. Thus, for efficient stimulated emission we need a large σ_{SE} and/or large I_{depl}. The cross-section for stimulated emission is proportional to the oscillator strength of the electronic transition from S_1 to S_0. According to Einstein, this oscillator strength is the same as for the reverse transition ($S_0 \rightarrow S_1$).[1] This means that we should be able to identify molecules with large stimulated-emission cross-sections by pronounced absorption peaks corresponding to the $S_0 \rightarrow S_1$ transition. The larger the oscillator strength, the larger the extinction coefficient.

Common UV photoinitiators are indeed very good absorbers. Obviously, it is essential for industrial photocuring that light is efficiently absorbed and leads to the initiation of the polymerization reaction efficiently. Commercially available UV photoinitiators are highly optimized to fulfill this purpose. Unfortunately, they do not at all have a pronounced

[1] For STED we need at least a three-level system. Otherwise, the depletion laser would directly re-excite the molecules after depletion and the molecule would undergo Rabi oscillations instead of being depleted. The vibronically excited levels S_1^* and S_0^* extend the system to a four-level system (see Fig. 3.2). However, the above simple reasoning is still meaningful.

$S_0 \rightarrow S_1$ transition (that we could use for efficient stimulated emission) but pronounced $S_0 \rightarrow S_n$ transitions to higher singlet states, instead. The former transition is usually of type $n \rightarrow \pi^*$. Due to small spatial overlap of the initial n orbital and the final π^* orbital of the promoted electron, such transitions have inherently low oscillator strengths (*e.g.*, roughly $100\,\mathrm{L\,mol^{-1}\,cm^{-1}}$ for Irgacure 907 [80]). The transitions to the higher singlet states are often of type $\pi \rightarrow \pi^*$, have large spatial overlaps between the initial π and the final π^* orbital, and are therefore more pronounced (*e.g.*, $> 20\,000\,\mathrm{L\,mol^{-1}\,cm^{-1}}$ for Irgacure 907 [80]). In sharp contrast, the $S_0 \rightarrow S_1$ transitions of all fluorescent dyes used in STED microscopy are of the type $\pi \rightarrow \pi^*$ (see Fig. 5.2) and have large oscillator strengths (*e.g.* $45\,000\,\mathrm{L\,mol^{-1}\,cm^{-1}}$ for ATTO 425 [81], $120\,000\,\mathrm{L\,mol^{-1}\,cm^{-1}}$ for ATTO 594 [81], and $150\,000\,\mathrm{L\,mol^{-1}\,cm^{-1}}$ for ATTO 647N [81]). For the pure photoinitiation, the low oscillator strength of the first transition is no issue at all: Upon light exposure, the photoinitiator molecules are efficiently excited to a higher singlet state S_n. From this highly excited state, the molecules can either directly convert to the triplet manifold or quickly relax to the S_1. From the S_1, fluorescence emission is very unlikely due to the low oscillator strength of the $S_1 \rightarrow S_0$ transition. Therefore the molecules undergo intersystem crossing with a very high yield.

The low-oscillator-strength $S_0 \rightarrow S_1$ transitions can be recognized as a small shoulder in the exemplary absorption spectra in Fig. 5.1. Often, this fundamental transition is not visible in the spectra at all. Therefore, it may be hard to judge whether a pronounced peak in the absorption spectrum of a photoinitiator corresponds to the $S_0 \rightarrow S_1$ transition (and, hence, would render the molecule promising) or to a $S_0 \rightarrow S_n$ transition (which would render the molecule unfavorable for STED). Obviously, the absorption spectrum and the measured extinction coefficients alone are not a good measure for the STED-suitability.

Lifetime:

Another difference between common photoinitiators and fluorescent dyes is the lifetime τ of the S_1 state. As this excited state is the intermediate state that we want to deactivate *via* STED, its lifetime sets the time frame for potential interaction with the depletion photons. We have chosen to use cw depletion, which means that only the fraction $\tau/(12.5\,\mathrm{ns})$ of the depletion laser photons have an effect at all, where 12.5 ns is the pulse-to-pulse separation of our 80 MHz excitation-laser.

For fluorescent dyes, common values for τ are $2-5\,\mathrm{ns}$ [5, 61]. Due to their high fluorescence quantum efficiencies, the S_1 lifetime is mainly determined by the fluorescent depopulation rate k_{fl}. Thus, shorter lifetimes correspond to larger oscillator strengths and are therefore not bad *perse*.

Typical lifetimes of common radical photoinitiators are on the order of 100 ps [11, 80, 82]. This leaves an unfavorably short time window for interaction. When aiming for cw depletion, this means that only roughly 1% of the photons of the depletion beam have an effect at all. For typical photoinitiators, the S_1 lifetime is dominated by the intersystem-crossing rate k_{ISC} rather than by the fluorescent rate. Therefore, small lifetimes most likely imply fast ISC and are simply unfavorable.

Even if short laser pulses are available for depletion, these short lifetimes limit the depletion performance: The shorter the pulses get (at a fixed pulse energy), the higher is the probability for undesired multi-photon absorption of the depletion laser. As we will see in Section 6.1.2, this kind of undesired absorptions is a relevant limitation indeed.

Excited-state absorption:

Last, a limiting factor for the applicable depletion power is excited state absorption (ESA) from the S_1 state to higher S_n states. This process is induced by depletion-laser photons and, hence, competes with stimulated emission. Naively, one would assume that the small oscillator strength and the short lifetime described in the previous two paragraphs can be compensated by simply increasing the depletion power. As our cw depletion-laser has a maximum output power of 10 W and even more powerful lasers are available at this wavelength, there would be enough power to compensate for orders-of-magnitude shortcomings of the photoinitiator. However, the applicable laser power is limited by at least two things. First, the photoinitiator in its ground state does absorb the depletion light *via* 1PA or multi-photon absorption and leads to unwanted photopolymerization by the depletion laser (see previous section). Second, ESA competes with stimulated emission. The lower the stimulated-emission cross-section is, the more critical is the effect of ESA.

The behavior of such highly excited S_n states is hard to predict. In best case, the molecules will relax back from S_n to S_1 and can then perhaps be depleted. However, multiple sequential excitations to S_n and relaxations to S_1 will likely heat the photoresist locally. This temperature rise will eventually limit the applicable depletion power.

Moreover, molecules in highly excited states are known to show enhanced reactivity and often enhanced ISC rate-constants [66]. In both cases, the application of high depletion powers could lead to an enhanced polymerization instead of a depletion. This may also be a contribution to the experimental finding that for common UV photoinitiators the polymerization threshold is actually decreased by the depletion laser.

In addition, the cross-sections for ESA are hard to predict. However, the first impression from the absorption spectra of common photoinitiators (Fig. 5.1) and fluorescent dyes (Fig. 5.2) is that the latter seems to have a sparse energy-level structure: The single peak of the coumarin dye is likely only a single transition ($S_0 \rightarrow S_1$) because it has the mirrored shape of the fluorescence spectrum (which corresponds to the $S_1 \rightarrow S_0$ transition according to Kasha's rule [83]). At the short-wavelength side of this peak, the absorption declines considerably. In sharp contrast, the spectra of common photoinitiators show evidence for very tight energy levels. The $S_0 \rightarrow S_1$ (which should have the mirrored shape of the fluorescence) is hardly visible as a shoulder. On the short-wavelength side, the absorption rises continuously, indicating a high density of excited states.

To avoid ESA, the search for a dye-like spectrum may be a good guideline. A better rationale is to perform pump-probe experiments as described in Section 5.2.1 to directly access the transient optical properties of photoinitiator candidates.

5.1.3. Fluorescence quantum-efficiency as figure of merit

Now that we have elaborated on the necessary properties of a photoinitiator suitable for STED, we have to find convenient measures that are easily accessible experimentally. The oscillator strength can be easily measured using commercial UV-VIS spectrophotometers. However, it is not evident whether a pronounced absorption peak with high oscillator strength stems from the $S_0 \rightarrow S_1$ transition. The lifetime of the S_1 state can be measured by time-correlated single photon counting (TCSPC). In our labs this is a non-routine experiment and lifetimes below 1 ns are not reliably accessible because the instrument response function of the used avalanche photodiodes is around that value.

It turns out that a combination of these properties can be easily accessed by measuring the fluorescence quantum yield Φ_{fl} of the photoinitiators. This quantity is given by the ratio of the number of fluorescence photons emitted and the number of molecules excited. The value is given by

$$\Phi_{\mathrm{fl}} = \frac{k_{\mathrm{fl}}}{k_{\mathrm{fl}} + k_{\mathrm{ISC}} + k_{\mathrm{nr}}} = k_{\mathrm{fl}} \cdot \tau \propto \epsilon \cdot \tau \,, \tag{5.1}$$

where k_{fl} is the fluorescence rate, k_{ISC} is the intersystem-crossing rate, k_{nr} is the non-radiative decay rate, τ is the S_1 lifetime, and ϵ is the oscillator strength.

The fluorescence quantum-efficiency is proportional to the relevant oscillator strength and the excited-state lifetime. Therefore, we will search for photoinitiating molecules with high fluorescence quantum yield. Intuitively, this makes sense: Pronounced non-radiative decay is harmful for Φ_{fl} as well as for efficient STED (due to the resulting short lifetime). Large oscillator strength of the $S_1 \rightarrow S_0$ transition favors spontaneous emission as well as stimulated emission.

Experimental method:

We measure the fluorescence quantum efficiencies of several photoinitiators in ethanol solution. The fluorescence quantum efficiency can be conveniently measured relative to a known fluorescence standard. We use 9,10-diphenylanthracene which is known to have $90 \pm 5\%$ quantum efficiency in ethanol solution [84, 85]. In a first step, photoinitiator solutions with different concentrations are prepared and absorption and emission spectra are taken using the commercial UV-VIS spectrophotometer (Varian Cary 300 Scan) and fluorescence spectrophotometer (Varian Cary Eclipse). For each solution, the absorbance at the fluorescence-excitation wavelength[2] is extracted from the absorption spectra.[3] The measured fluorescence for each solution is integrated[4] and this integral fluorescence intensity is finally plotted *vs.* the respective absorbance values (see Fig. 5.3). The plotted lines are linear fits to the data. The lines are required to emanate from the origin. The slope (which is the amount of fluorescence divided by the amount of absorbed excitation

[2]The excitation wavelength was 350 nm or 380 nm, depending on the photoinitiator absorption spectrum.
[3]The extinction of a pure ethanol sample was used as baseline.
[4]The background-fluorescence signal from a pure ethanol sample was subtracted from all measured fluorescence spectra.

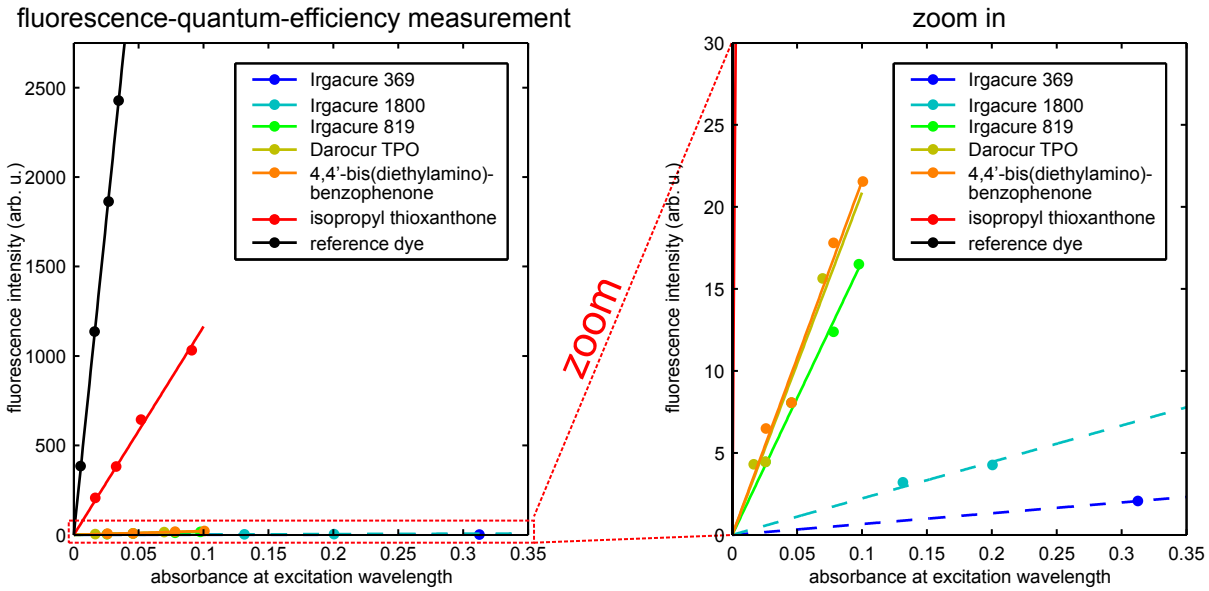

Figure 5.3.: Measurements of the fluorescence quantum efficiencies of different photoinitiators. The fluorescence intensity is plotted *vs.* the absorbance at the excitation wavelength for different concentrations. Circles are data, solid lines are linear fits. The slopes are proportional to the fluorescence quantum-efficiency. 9,10-diphenylanthracene serves as a reference dye with 90 % fluorescence quantum yield.

photons) is proportional to the fluorescence quantum-yield. Knowing the fluorescence quantum yield of the fluorescence standard allows to determine the proportionality factor and calculate the unknown quantum efficiencies of the other sample molecules.

We use a cuvette with a 10 mm × 10 mm footprint. It is important to ensure that the absorbance at the excitation wavelength and the emission wavelengths is below 0.1. Otherwise, the resulting data can be obscured by the inner filter effect [86]. In this case, the emitted light on its way out of the cuvette can be reabsorbed by ground-state molecules. Therefore, the recorded emission yields would be to low. For Irgacure 369 and Irgacure 1800 the emission was so weak, however, that the concentration had to be increased further. Therefore, the extracted values of 0.03% and 0.01% are to be taken with caution. We have plotted the corresponding ambiguous fits as dashed lines in Fig. 5.3. These experimental challenges clearly imply that the fluorescence quantum yield is very low. We discard the exact values and estimate 0.1% as an upper bound for these two photoinitiators.

Results:

The resulting values for Φ_{fl} are printed in Table 5.1. Clearly, the measured fluorescence quantum yields of common UV photoinitiators (upper group) are very low. In this light, it is not surprising that an efficient deactivation *via* stimulated emission was not observed in corresponding lithography experiments. We find two photoinitiators (lower group in Table 5.1), however, that show significant fluorescence quantum efficiencies and

Table 5.1.: Measured fluorescence quantum-efficiencies of different photoinitiators. Common photoinitiators (upper block) have poor fluorescence quantum-yields. The photoinitiators in the lower block possess larger values and do also provide a depletion mechanism. The last value is recorded dissolved in the monomer pentaerythritol tetraacrylate (PETTA).

Photoinitiator	**Φ_{fl} in %**
Irgacure 369 in ethanol	<0.1
Irgacure 1800 in ethanol	<0.1
Irgacure 819 in ethanol	0.2
Darocur TPO in ethanol	0.3
4,4'-bis(diethylamino)benzophenone in ethanol	0.3
isopropyl thioxanthone (ITX) in ethanol	14.9
7-diethylamino-3-thenoylcoumarin (DETC) in ethanol	2.3
7-diethylamino-3-thenoylcoumarin (DETC) in PETTA	29

are therefore good candidates for STED lithography. The first photoinitiator, isopropyl thioxanthone (ITX), shows a fluorescence quantum-efficiency of 15% in ethanol solution. The second photoinitiator, 7-diethylamino-3-thenoylcoumarin (DETC) [87], shows value of 2.3% in ethanol solution.[5] However, when exchanging the solvent by the actual high-viscosity monomer used in our photoresists the efficiency increases to 29%. The reason for this massive change is not known. Such solvent-dependent efficiencies can for example be ascribed to solvent-dependent non-radiative depopulation channels k_{nr} or k_{ISC}. This non-radiative decay would then have to be very pronounced in ethanol (and successfully outperform the fluorescence channel) and should be very weak when dissolved in the monomer (compare Eq. 5.1).

For ITX, we have previously determined S_1 lifetimes in ethanol (2.7 ns) and in a higher viscosity monomer (2.3 ns) by means of TCSPC [88]. These similar values lead us to the conclusion that the fluorescence quantum-efficiency of ITX is rather solvent-independent.

5.1.4. Successful polymerization suppression with ITX and DETC

The two photoinitiator candidates identified by their high fluorescence quantum yield are now tested in a lithography experiment. Again, the simplest experiment conceivable is to write a line with the excitation laser and to stop the polymerization temporally by switching on the depletion power at an appropriate power level.

For this purpose, we prepare photoresists as described in Section 5.1.1 using these photoinitiators. The corresponding formulations are depicted in Fig. 5.4. The spectra

[5] The measured data for DETC are not depicted in Fig. 5.3, as they stem from a separate measurement session and may not be directly comparable.

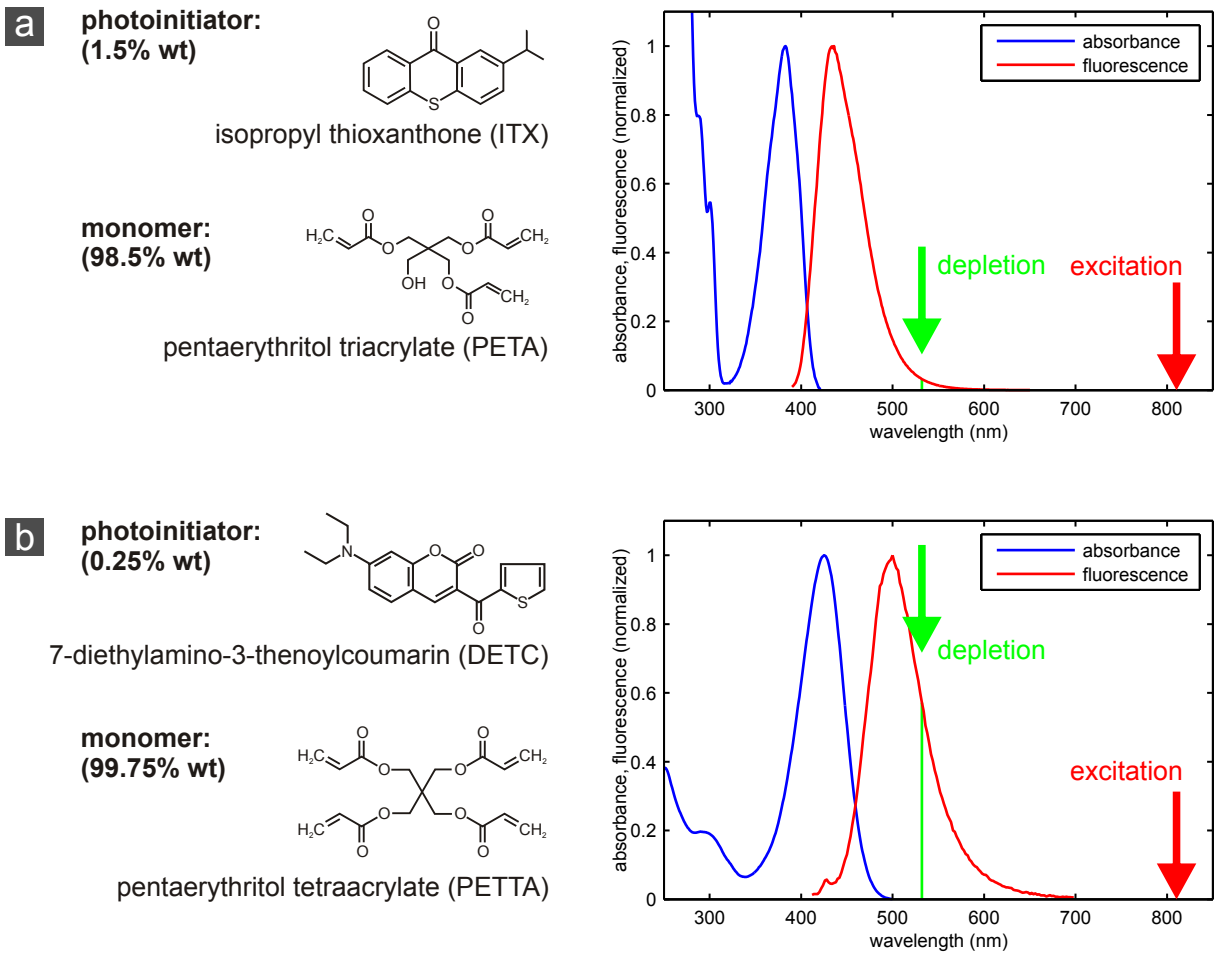

Figure 5.4.: Ingredients of the photoresists with depletion capability. The left sides show the molecules contained in the resists. In addition, both resists contain 300-400 ppm monomethyl ether hydroquinone as inhibitor to increase the shelf lifetime. The right sides show the absorption and fluorescence spectra of the respective photoinitiators in ethanol. (a) ITX-based photoresist. (b) DETC-based photoresist. The DETC-based resist uses the tetra-functional monomer pentaerythritol tetraacrylate (PETTA) instead of the previously used pentaerythritol triacrylate (PETA). The behavior of the two monomers does not differ significantly.

on the right hand side of Fig. 5.4 are taken in ethanol solution. We can immediately see that there is a pronounced absorption peak that looks like the mirror image of the fluorescence. This indicates that we see the $S_0 \rightarrow S_1$ transition indeed, which happens to be a $\pi \rightarrow \pi^*$ transition for these molecules. The oscillator strength is moderately high for ITX ($903\,\mathrm{L\,mol^{-1}\,cm^{-1}}$ [89]) and very high for DETC ($40\,550\,\mathrm{L\,mol^{-1}\,cm^{-1}}$ [89]). The latter value is comparable to that of state-of-the-art green-fluorescing dyes (*e.g.*, $45\,000\,\mathrm{L\,mol^{-1}\,cm^{-1}}$ for ATTO 425 [81]). Moreover, the absorption spectra look more "dye-like", as the fundamental absorptions are well separated from higher absorption bands. Hence, we expect the photoinitiators to be suitable for stimulated-emission depletion in lithography.

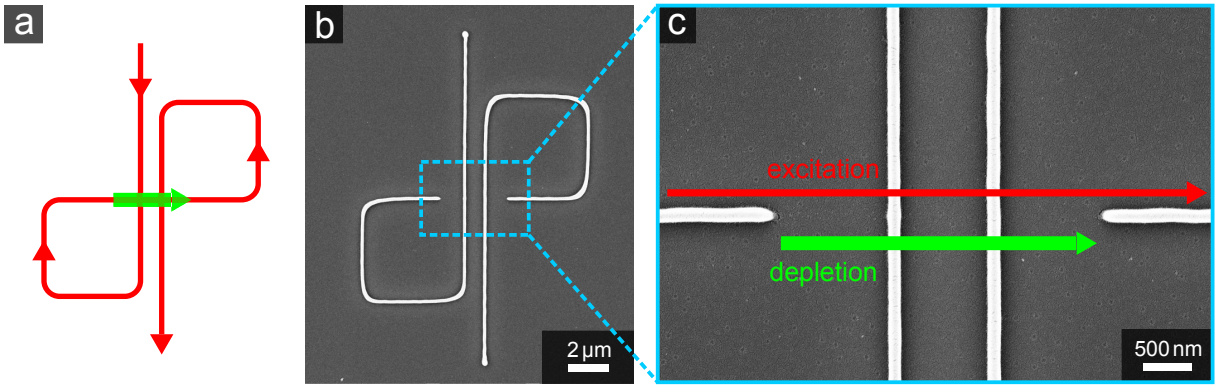

Figure 5.5.: Successful suppression of the photopolymerization using the ITX-based photoresist. (a) Writing trajectory used for the test structure. The continuous red path corresponds to the excitation laser being switched on all the time. The small green path corresponds to a small segment where the depletion laser was switched on in addition. (b) SEM image of the resulting polymer structure on the substrate surface. (c) SEM zoom-in showing the depleted region. Note that neither passing already polymerized lines with depletion laser on nor polymerizing previously depleted regions is an issue. Previously published in Ref. [88].

We start out with the ITX-based photoresist (see Fig. 5.4 (a)). In the lithography experiment, we write a special line pattern (see red line in Fig. 5.5) with 100 µm/s scan speed and 10 mW average excitation power directly at the substrate-resist interface. In one part of the pattern the co-aligned Gaussian depletion focus is switched on with a power of 37.5 mW. The pattern is chosen such that the trajectory exhibits two crossing points that we will discuss below.

The resulting structures are developed, sputtered with $\approx$ 6 nm gold and imaged with a scanning-electron microscope (SEM). The resulting images are depicted in Fig. 5.5. Indeed, the polymerization immediately stops when switching on the depletion laser and immediately starts again when switching it off. The depleted region is very clean and no residual polymerization is observed. This means that a digital switching of the polymerization is possible when using appropriate power levels. In case the depletion power is somewhat low, there is some remaining polymerization (not depicted). At even lower depletion power levels, the line stays connected (not depicted). The middle segment, however, shows a lower linewidth because the entire exposure dose profile is effectively reduced towards the threshold.

The two crossing points in the trajectory give us further important information. At the left crossing point, an already polymerized line is crossed with both lasers being switched on. The fact that the first line is not significantly altered at the crossing point tells us that we do not harm the final polymer by the depletion laser (which would prevent the fabrication of complex 3D structures). The first line could also be significantly thicker after being passed the second time. This would indicate that the depletion effect does not work in direct vicinity of the final polymer. This is not the case either. The second crossing point is even more important. In case the depletion laser would irreversibly damage the photoinitiator or the photoresist in general, one would expect that the vertical line (that is

written after the depletion) would not polymerize properly. It might be disconnected, or at least be thinner due to a reduced effective exposure dose caused by the lower concentration of undamaged photoinitiator. However, we can not observe any change in the photoresist sensitivity. The time delay between the depletion and the re-writing of the right crossing point was 0.2 s in this case.

The important message in this experiment is that the polymerization process is irreversible after 0.2 s (*i.e.*, $\tau < 0.2\,\mathrm{s}$), which is necessary for the fabrication of complex structures and fast scanning. On the other hand, the depletion mechanism is reversible on this time scale (i.e., $\tau + \tau_{\mathrm{rec}} < 0.2\,\mathrm{s}$), and the resist recovers completely. However, the real time scales are expected to be much smaller. The first timescale will be examined more closely in Section 5.2.2.

For the DETC-based photoresist (see Fig. 5.4 (b)), we obtain comparable results, yet at different power levels. This resist is based on the monomer pentaerythritol tetraacrylate (PETTA). We assign the depletion effect to the photoinitiators alone as the two monomers are in fact interchangeable and appear not to influence the depletion. As a double check, we have also used the monomer Sartomer SR502 (ethoxylated (9) trimethylolpropane triacrylate) together with ITX and have observed the depletion effect as well (not depicted).

As we will see in the next section, STED is not the only mechanism involved in the observed depletion effect. Therefore, for the remainder of this thesis, we will refer to our novel lithography approach as "STED-inspired DLW". While the term "depletion DLW" is meant to describe any depletion-assisted lithography scheme using any depletion mechanism (see Section 3.6), we use the term "STED-inspired DLW" for the approach developed in our group, featuring ITX or DETC in conjunction with a 532 nm cw depletion laser.

5.2. Investigation of the depletion mechanism

As we have seen in the previous section, our photoresists based on ITX and DETC can be "switched off" with a 532 nm wavelength cw depletion laser. We have been guided to these photoinitiators by looking for properties favorable for stimulated emission. In addition, we have performed experiments aiming at depleting the fluorescence emission of these photoinitiator molecules in ethanol solution. Indeed, the fluorescence can be quenched to roughly 50% of its initial intensity (see Appendix A.1).

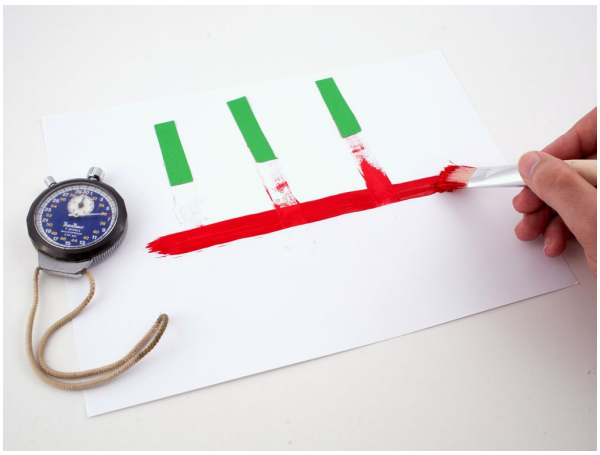

So far, all these observations are consistent with the expectations for STED. Nevertheless, the observed depletion could still be due to other effects. As indicated in Section 3.6.4, excited-state absorption might play a role as well. Our rationale for finding suitable photoinitiators was intended to favor stimulated emission. However, not only stimulated emission but also non-radiative decay channels described in 3.6.4 might profit from the $\pi \rightarrow \pi^*$ nature of the S_1 state.

For this reason, we have performed two sets of time-resolved experiments to clarify the underlying mechanisms of the observed polymerization suppressions in ITX- and DETC-based photoresists [89, 90].

5.2.1. Pump-probe experiments on ITX and DETC in ethanol solution

As a first set of experiments we have performed femtosecond pump-probe experiments on ITX and DETC in ethanol solution. These experiments have been done in collaboration with Thomas A. Wolf in the group of Andreas-Neil Unterreiner and have already been published in Ref. [89].

We use a regenerative Ti:sapphire amplifier seeded by a fiber oscillator as the master source. The laser operates at 775 nm center-wavelength and generates pulses of 150 fs width with a repetition rate of 1 kHz. A small portion is used for second-harmonic generation, which serves as pump centered around 387.5 nm wavelength. In this case, the molecules are excited *via* 1PA. The probe pulses are generated from the amplifier output by means of a non-collinear optical parametric amplifier. The probe pulses have a length of < 40 fs and can be tuned between 473 nm and 900 nm. These pulses can be delayed by a mechanical delay stage. Both beams pass a sample cuvette containing the photoinitiator molecules in ethanol solution and overlap in the sample region. The power of the transmitted probe beam is measured after the sample.

In a nutshell, this experiment determines the time-dependent change in the optical density (OD)[6] of the sample that is induced by the pump laser. The anticipated contributions to this change are depicted in Fig. 5.6 (a). We assume to pump the molecules into an electronically and vibronically excited state S_1^*. Some portion of the excited molecules may directly decay to the ground-state non-radiatively. A major portion, however, will quickly decay to S_1 non-radiatively. For a timescale between roughly 0.1 ns to 5 ns, we expect to see contributions from the occupied S_1 state. Negative signal contributions originate from stimulated emission, positive contributions stem from ESA to higher singlet states S_n. For probe wavelengths close to the fundamental absorption of the ground-state molecules, a negative signal might arise from the depopulation of the ground-state by the intense pump beam. This should not be misinterpreted as stimulated emission. For longer pulse delays we will most likely probe the sub-sequentially occupied

[6] To avoid confusion, we want to clarify that we use the term OD synonymous to absorbance: $\mathrm{OD} = \log_{10}(I_{\mathrm{in}}/I_{\mathrm{out}})$. In the literature, the term OD is sometimes also used for the index of refraction, which is not meant here.

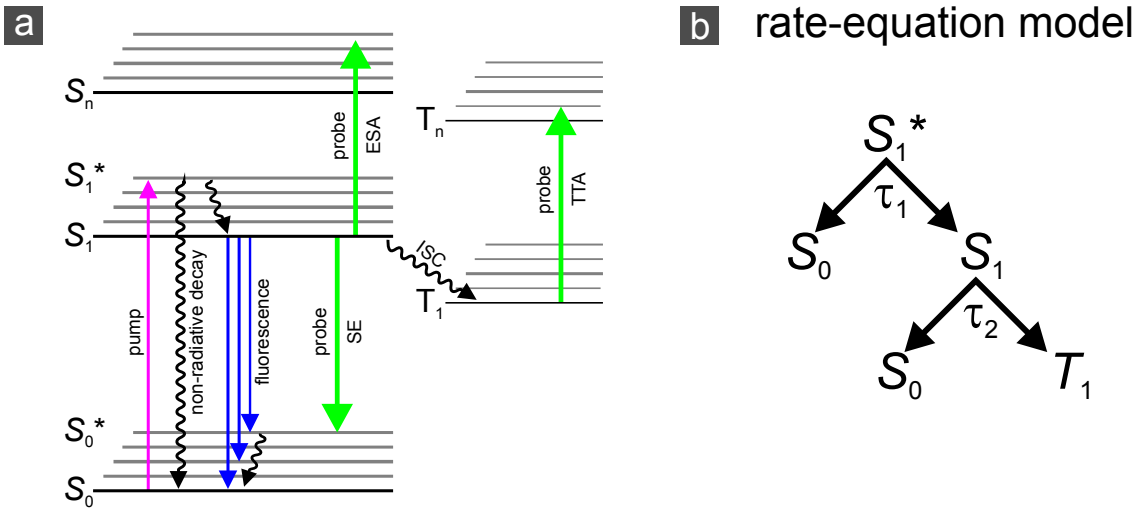

Figure 5.6.: (a) Scheme of transitions in a photoinitiator molecule for STED optical lithography and the anticipated contributions to the pump-probe signal. Pump laser photons (pink) excite a molecule from the S_0 ground-state into an excited state S_1^*. After vibrational relaxation to the S_1 state, probe photons (green) can bring the molecule back to its ground state *via* stimulated emission (SE) or into yet higher-energy states *via* excited-state absorption (ESA). After intersystem crossing (ISC) to the triplet state T_1, triplet-triplet absorption (TTA) of probe photons may occur. (b) Simple rate-equation model used to fit the experimental data. The time constants τ_1 and τ_2 describe the depopulation of S_1^* and S_1, respectively. Previously published in Ref. [89].

triplet state T_1. Here, we expect to see only positive contributions corresponding to a $T_1 \rightarrow T_n$ absorption.

To interpret the time dynamics of the signals, we construct a simple rate-equation model for the decay of the initially excited species (Fig. 5.6 (b)). As described in the previous paragraph, the S_1^* population can decay either to S_0 or S_1 with an overall decay rate of τ_1. The S_1 population can then decay to S_0 or to T_1 with a time constant τ_2. The contributions of the pump-probe signal originating from these states have to decay with the same time constants. Solving the corresponding set of differential equations leads to a model function

$$\Delta\mathrm{OD}(\Delta t) = A_\lambda \mathrm{e}^{-\Delta t/\tau_1} + B_\lambda \mathrm{e}^{-\Delta t/\tau_2} + C_\lambda(\tau_1 \mathrm{e}^{-\Delta t/\tau_1} - \tau_2 \mathrm{e}^{-\Delta t/\tau_2} + \tau_2 - \tau_1)\,. \qquad (5.2)$$

As we have three molecular states that contribute to ΔOD (S_1^*, S_1, and T_1), it is natural to have three fit parameters for each probe wavelength (A_λ, B_λ, and C_λ). The quantity B_λ is proportional to the ΔOD-contribution of the S_1 state, while C_λ is proportional to the ΔOD-contribution of the T_1 state. We will fit the experimental data for all probe

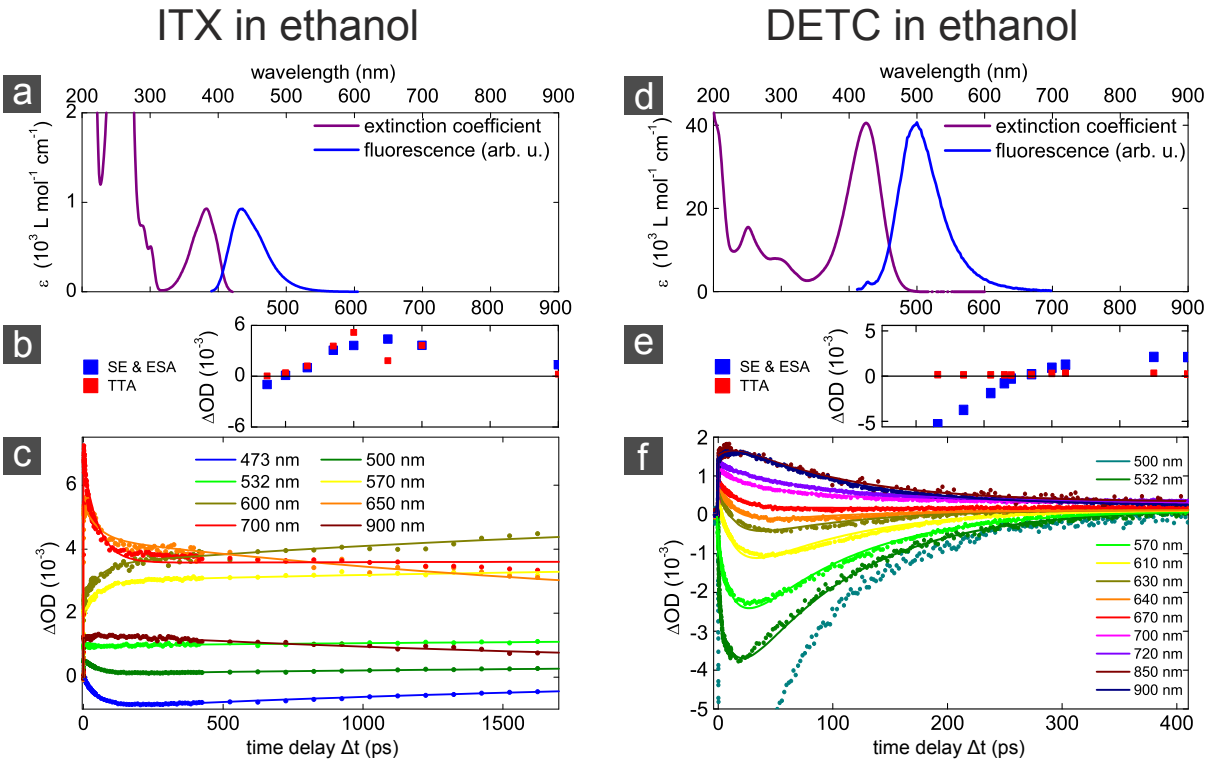

Figure 5.7.: Results of the pump-probe experiments on ITX (a–c) and DETC (d–f) in ethanol solution. (a, d) Molar decadic extinction coefficient (ϵ) and fluorescence spectrum the compounds. (c, f) Time-delay-dependent change of the optical density, ΔOD (dots), after 387.5 nm excitation for different probe wavelengths as indicated. $\Delta\mathrm{OD} < 0$ corresponds to increased probe transmittance upon optical pumping. The solid curves result from a global fit of a simple rate-equation model to these data. (b, e) Fit coefficients B_λ corresponding to the the sum of the observed SE and ESA (blue) and fit coefficients C_λ corresponding to the observed TTA (red). Previously published in Ref. [89].

wavelengths using this model with common fit parameters τ_1 and τ_2, yet with independent parameters A_λ, B_λ, and C_λ for each probe wavelength λ.[7]

The resulting data for ITX and DETC are depicted in Fig. 5.7 (c) and (f), respectively. The dots correspond to measured changes in optical density at the probe wavelength. The different probe wavelengths are color-coded as indicated. Solid lines are global fits to the data using the above model function. The panels (b) and (e) show fit coefficients from the global fits to the ITX data and the DETC data. In both panels, the transient contributions originating from S_1 are plotted as blue squares and the contributions from T_1 are plotted as red squares.

For ITX, we see already in the raw data that the transient change in OD is mainly positive. After a fast decay of the S_1^* species with $\tau_1 = 48$ ps we see positive contributions

[7]For DETC, the data at a probe wavelength of $\lambda = 500$ nm are not included in the global fits (see Fig. 5.7 (f)). The temporal behavior at this wavelength does slightly differ from that of longer wavelengths, probably due to the vicinity of the ground-state absorption band.

from S_1. This means that ESA dominates over stimulated emission. Only for the shortest wavelength of 473 nm we get a slightly negative signal corresponding to weak stimulated emission. With a time constant of $\tau_2 = 2.6\,\text{ns}$ the S_1 contribution fades into the T_1 contribution which has positive values *per se*. We conclude that the depletion effect observed with ITX-based photoresists is unlikely to be dominated by stimulated emission. Excited-state absorption from S_1 or T_1 is more likely to play a key role here.

For DETC, the situation is different. Here we see negative signals over a broad wavelength region. Especially for our standard depletion wavelength of 532 nm wavelength we see a negative signal that we assign to stimulated emission. Out of the global fit, we get the time constant for the S_1^* decay as $\tau_1 = 13.8\,\text{ps}$ and the lifetime of the S_1 state as $\tau_2 = 99\,\text{ps}$. Consequently, DETC in ethanol supports stimulated emission indeed, yet for an unfavorably short time of 0.1 ns. The fit coefficients B_λ for the S_1 contribution plotted in blue in Fig. 5.7 (e) do nicely resemble the fluorescence spectrum plotted above in panel (d): The higher the fluorescence spectrum, the stronger the transient gain observed. This is consistent with the interpretation that the negative signal is due to stimulated emission. For longer probe wavelengths, the B_λ becomes positive. Here, ESA from S_1 takes over. The triplet contribution C_λ is spectrally flat and slightly positive.

In conclusion, the pump-probe experiments presented in this sub-section suggest that STED is possible with DETC. The situation in a real photoresist can, however, differ drastically from that in ethanol solution. For example, the higher viscosity can change the rate constants and lifetimes of the molecular states. We have already seen in Section 5.1.3 that the fluorescence quantum-efficiency of DETC changes by more than an order of magnitude when exchanging ethanol by monomer. Even if the parameters would not change at all, other depletion mechanisms can still contribute to the observed effect in the DETC-based photoresist. One candidate for an alternative mechanism would be based on a triplet-triplet absorption. At first glance, the triplet-triplet absorption of DETC in ethanol seems negligible (red squares in Fig. 5.7 (e)). However, we have to keep in mind that the lifetime of the T_1 state can be orders of magnitude larger than that of the S_1. Therefore, the number of depletion photons absorbed by the triplet could easily exceed the number of photons that can trigger stimulated emission (especially for cw depletion). In the following sub-section, we will therefore investigate the depletion mechanism of DETC directly within the photoresist.

5.2.2. Pump-probe lithography experiments on DETC-based photoresist

To investigate the depletion mechanism directly within the actual photoresist we perform a second set of experiments. In these experiments, we use our STED-inspired DLW setup and replace the cw depletion-laser by a pulsed tunable depletion-laser. The depletion-pulse wavelength and the pulse timing between excitation and depletion can be adjusted to gain information about the underlying dynamics. The results in this subsection have already been published in Ref. [90] and major parts of the text have been taken over verbatim.

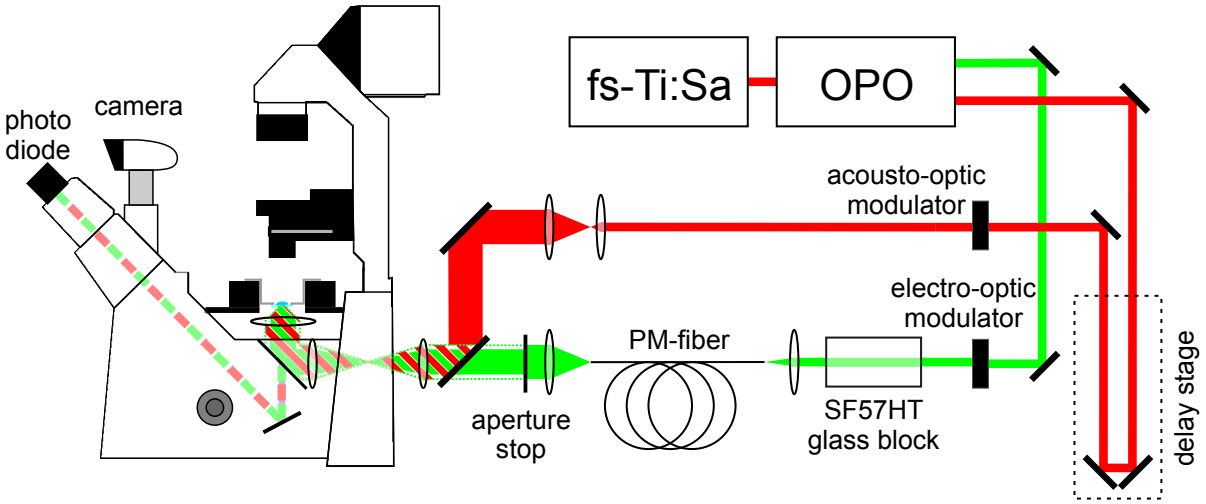

Figure 5.8.: Schematic illustration of the modified DLW setup used for the pump-probe-like lithography experiments. A femtosecond Ti:sapphire oscillator tuned to 820 nm pumps a second-harmonic-driven optical parametric oscillator (OPO). The residual 820 nm beam is delayed with a manual delay stage and used for two-photon excitation. The depletion pulses generated by the OPO are stretched by the transmission through a 15 cm long block of highly dispersive glass and 150 m of polarization-maintaining (PM) single-mode fiber. An aperture imaged onto the objective lens is used to reduce the diameter of the depletion beam. Previously published in Ref. [90].

The modified version of our STED-inspired DLW setup (see Fig. 4.1) is illustrated in Fig. 5.8. The femtosecond Ti:sapphire oscillator (fs-Ti:Sa) is tuned to 820 nm and used to pump an optical parametric oscillator (OPO). This machine (Newport Inspire HF100) first generates the second harmonic of the pump beam. The OPO frequency conversion is then driven by the resulting 410 nm beam. The residual 820 nm pump beam is used for two-photon excitation of the photoinitiator. A manual translation stage is used to delay the excitation pulses with respect to the depletion pulses. The stage position for pulse delay $\Delta t = 0$ is determined by a fast silicon photodiode with an estimated accuracy of ± 0.1 ns. The power level of the new pulsed depletion beam is adjusted by an electro-optical modulator (EOM) (Linos LM 0202 P VIS KD*P). The visible depletion pulses derived from the OPO are unfavorably short (around 200 fs) and might lead to 2PA of the depletion pulses by the photoinitiator's ground state. To avoid this unwanted excitation, we stretch the pulses to an estimated length of 250 ps by sending them through a 150 m long polarization-maintaining single-mode fiber. To minimize non-linear effects inside the fiber, we pre-stretch the pulses by sending them through a 15 cm long highly dispersive SF57HT glass block.

To investigate the depletion capability at different wavelengths, we use a simple Gaussian-like depletion focus (*i.e.*, no phase mask is inserted). The overlap and diameter of the foci are measured with the method described in Section 4.2. In the lateral directions, the excitation focus has a FWHM of 330 nm. However, the squared excitation intensity

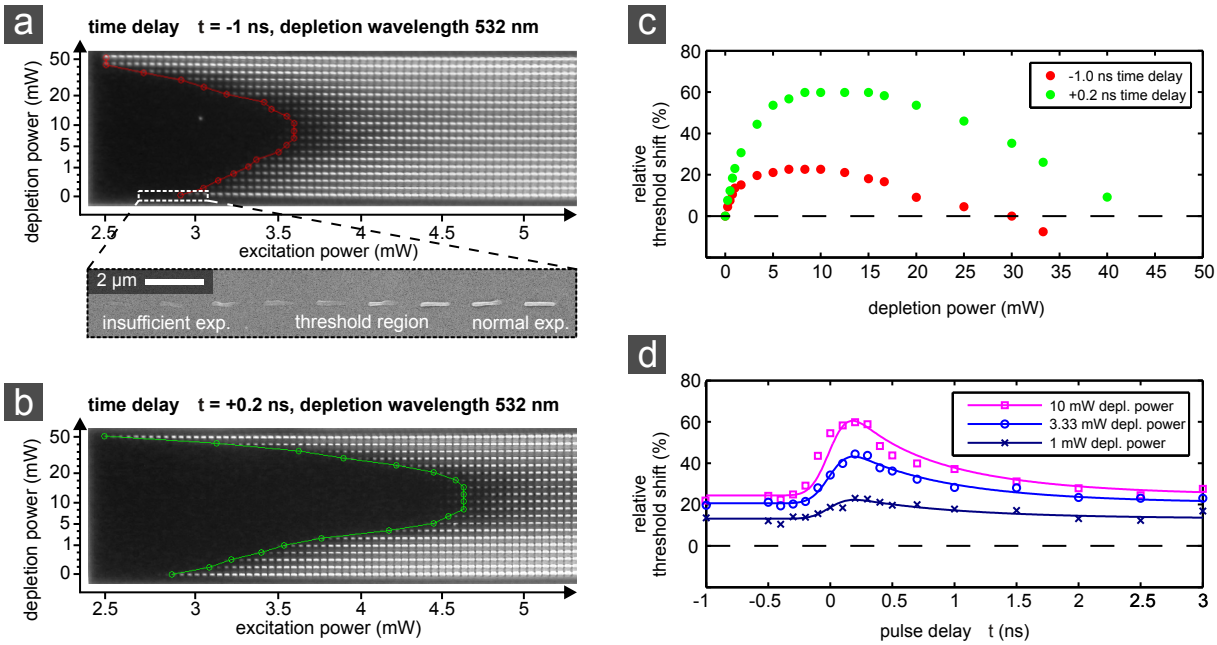

Figure 5.9.: (a) Optical micrograph (dark-field mode) of a typical pulsed depletion test pattern with 532 nm depletion wavelength and −1 ns time delay. The individual lines are 1.25 µm long. The polymerization-threshold powers are manually selected and marked with circles. For the region indicated by the white rectangle, an electron micrograph with higher magnification is depicted below the main panel and shows the transition from insufficient exposure to normal exposure. (b) Same as (a), but for +0.2 ns time delay. Note that the vertical scale is not linear. (c) Relative shift in polymerization-threshold power *vs.* average depletion power derived from (a) and (b). (d) Relative threshold shift *vs.* pulse delay for selected depletion powers. The solid curves are fits to the data (see Appendix A.2). Previously published in Ref. [90].

profile relevant for 2PA has a FWHM of only 225 nm. We reduce the depletion-beam diameter and, hence, its focusing NA (see Section 2.2.2) by means of an aperture to obtain a depletion focus that is larger than the excitation focus (FWHM 400 ± 20 nm). When tuning the depletion wavelength, this focus width is held constant by adjusting the beam diameter accordingly.

To obtain a quantitative measure of the depletion capability, we determine the polymerization-threshold power P_{th}. We define the latter as the smallest excitation laser power that still yields clear polymer lines that survive the development process. The corresponding lines are selected manually in the optical dark-field micrographs. We start by writing a series of lines with increasing excitation power (horizontal axis) and zero depletion power directly onto the substrate-resist interface (lowest row in Fig 5.9 (a)) at a constant scan velocity of 100 µm/s.

In this series, we determine the undisturbed polymerization-threshold power $P_{\mathrm{th},0}$. Next, we switch on the depletion laser tuned to 532 nm wavelength. Increasing the depletion laser power (vertical axis) shifts the threshold to higher powers $P_{\mathrm{th,shifted}}$, because part of the excited photoinitiator molecules are depleted and cannot contribute to the

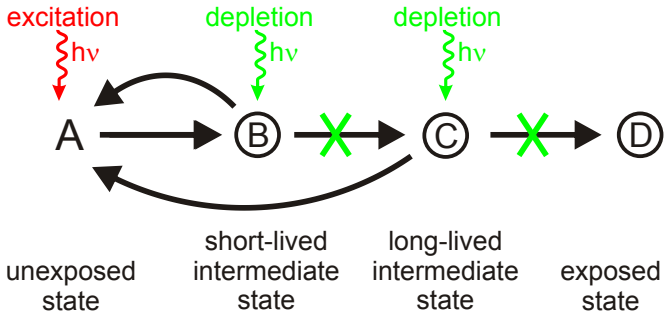

Figure 5.10.: Modified picture of the photoinitiator states appropriate for the DETC-based photoresist. Here, two intermediate states can be depleted. Compare to Fig. 3.6.

polymerization reaction. This means that for a given depletion power the polymerization can be effectively inhibited for writing powers between $P_{\mathrm{th},0}$ and $P_{\mathrm{th,shifted}}$ (as observed in Section 5.1.4).

The relative shift in threshold power $(P_{\mathrm{th,shifted}} - P_{\mathrm{th},0})/P_{\mathrm{th},0}$ in % is used as a measure of the depletion capability. Figure 5.9 (a) shows that the depletion capability increases up to an optimum average depletion power of 10 mW. Beyond that power, the depletion effect gets weaker and finally, for yet higher depletion powers, the threshold power even decreases. Here, the depletion laser leads to enhanced excitation that dominates over the depletion effect. On the basis of additional fluorescence experiments (see Appendix A.1), we conclude that the excitation of DETC by the depletion beam is mainly due to 1PA.

Next, we change the time delay between excitation and depletion pulses in order to investigate the temporal decay of the involved intermediate species. Figures 5.9 (a, b) show the resulting patterns for two characteristic pulse delays Δt. In Fig. 5.9 (a), the depletion pulses arrive before the excitation pulses ($\Delta t = -1$ ns). In Fig. 5.9 (b), the depletion pulses arrive shortly after the excitation pulses ($\Delta t = +0.2$ ns). The corresponding relative shifts in polymerization-threshold power extracted from these test patterns are plotted in Fig. 5.9 (c) and show different behavior. We repeat the test pattern for various further time delays (not depicted). The resulting Δt-dependent relative threshold shifts are plotted in Fig. 5.9 (d) for selected depletion powers. Solid lines are fits to the data (see Appendix A.2).

Interestingly, even for $\Delta t < 0$ (*i.e.*, the depletion pulses arrive shortly before the excitation pulses) we determine a positive threshold shift. This means that polymerization can still be suppressed, although 11.5 ns have passed since the last pulse of the 80 MHz excitation pulse-train. Around zero time delay, the attainable depletion rises within the duration of the depletion pulses and decays with roughly 1 ns time constant.

To explain this behavior, the picture for a generic depletion mechanism drawn in Fig. 3.6 must be changed to the one shown in Fig. 5.10. We assume the existence of two different sub-sequentially occupied intermediate states **B** and **C** with different lifetimes. Finally, the irreversibly exposed state **D** is reached. The fast decay (1 ns) corresponds to the lifetime of state **B** and can likely be assigned to the S_1 state's lifetime τ of DETC.

Another intermediate state **C** with a considerably longer lifetime ($> 12.5\,\mathrm{ns}$, *e.g.*, the T_1 state) is likely responsible for the depletion at negative (or large positive) time delays. Both intermediate states can lead to an effective inhibition of the photopolymerization.

So far, the fast effect (1 ns) originating from the S_1 could be either stimulated emission or be induced by ESA into yet higher singlet energy levels. The unexpected slow effect ($> 12.5\,\mathrm{ns}$), however, is definitely distinct from STED, as it can not originate from S_1.

In the previous section, we have found a different S_1 lifetime $\tau = 0.1\,\mathrm{ns}$ of DETC in ethanol solution [89]. This seeming discrepancy can be explained by solvent-dependent non-radiative decay rates: The lifetime of the state S_1 is given by

$$\tau = \frac{1}{k_{\mathrm{tot}}} = \frac{1}{k_{\mathrm{fl}} + k_{\mathrm{ISC}} + k_{\mathrm{nr}}}\,, \tag{5.3}$$

where k_{tot} is the sum of all decay rates contributing to the depopulation of S_1. Clearly, if the non-radiative rates k_{nr} and/or k_{ISC} increase when going from monomer to ethanol, this results in a shorter lifetime. Let us recall that we have previously measured the fluorescence quantum efficiency Φ_{fl} of DETC dissolved in ethanol and our monomer PETTA and obtained values of 2.3% and 29%, respectively (see Section 5.1.3). This unintuitive observation can also be explained by the same solvent-dependent non-radiative decay rates.

$$\Phi_{\mathrm{fl}} = \frac{k_{\mathrm{fl}}}{k_{\mathrm{tot}}} = \frac{k_{\mathrm{fl}}}{k_{\mathrm{fl}} + k_{\mathrm{ISC}} + k_{\mathrm{nr}}} = k_{\mathrm{fl}} \cdot \tau\,. \tag{5.4}$$

Assuming a solvent-independent radiative decay rate k_{fl}, the observed 12.5-fold increase in Φ_{fl} should directly correspond to a 12.5-fold increase in S_1 lifetime (hence, $\tau = 1.25\,\mathrm{ns}$ in monomer). This finding is in good agreement with the value of $\tau = 1.0\,\mathrm{ns}$ determined by fits to the above polymerization-experiment data. We speculate that this increase in the more viscous monomer is due to steric hindering of conformational changes necessary for ISC. Intersystem crossing is the main process that competes with radiative decay in the S_1 depopulation in DETC.

To further clarify the nature of the fast process, we repeat the above experiments for different depletion wavelengths. For wavelengths below $\lambda = 516\,\mathrm{nm}$, we observe little to no depletion at all (gray region in Fig. 5.11 (e)). When approaching the fundamental absorption of the photoinitiator molecule, the overall behavior is dominated by 1PA of the depletion beam. For every depletion wavelength between 524 nm and 600 nm, we observe the same general temporal behavior as for 532 nm. However, the relative strengths of the observed slow and fast components change with wavelength. As depicted in Fig. 5.11 (a), the fast effect decreases towards longer wavelengths while the slow effect gets even stronger. Circles are raw data, solid lines are fits like in Fig. 5.9 (d). These different dependencies are another indication that two distinct depletion mechanisms are at work in our photoresist. To illustrate the different behavior of the two effects, we select two corresponding time intervals in each curve and average over 3 data points (indicated by filled circles in Fig. 5.11 (a)). One curve like in Fig. 5.11 (a) then yields only two values of the threshold shift, one value for timing situation #1, where the depletion pulse arrives

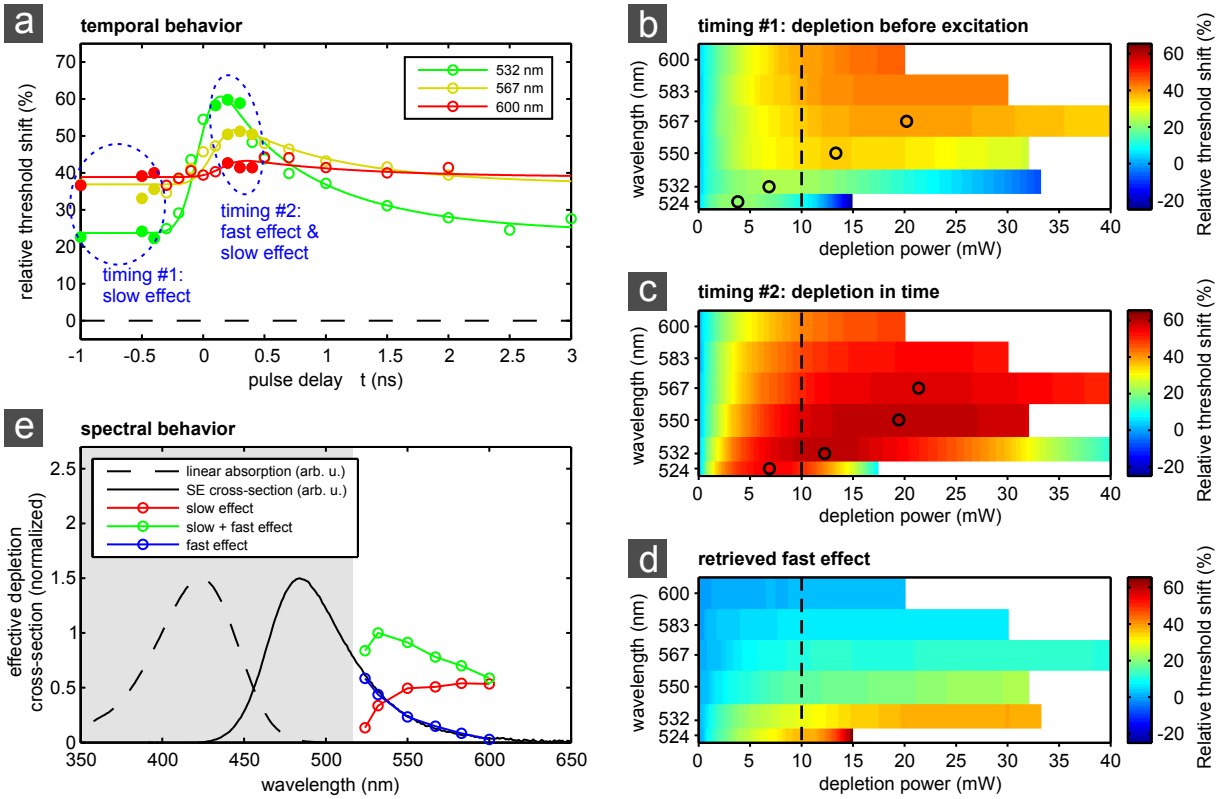

Figure 5.11.: (a) Pulse-delay-dependent relative threshold shift for different depletion-laser wavelengths as indicated. Solid lines are fits to the data sets. The average depletion power is 10 mW for all wavelengths. The data points with filled circles are examples of data chosen for (b, c). (b) Relative threshold shift *vs.* average depletion power and depletion wavelength for timing situation #1. Black circles mark the most effective depletion power for a given wavelength. The data along the vertical dashed line are used for panel (e). (c) Same as (b), but for timing situation #2. (d) Calculated threshold shift caused by the fast effect. (e) Spectral sensitivity of the different processes for 10 mW depletion power. The fast effect nicely follows the spectrum of the stimulated-emission (SE) cross-section. Due to pronounced 1PA, the gray area is inaccessible in our depletion experiments. Previously published in Ref. [90].

before the excitation pulse, and one value for timing situation #2, where the depletion pulse arrives "just in time" for optimal depletion. For timing #1, only the slow effect contributes, whereas for timing #2, both the fast effect and the slow effect contribute.

Figure 5.11 (b) illustrates the corresponding values for timing #1 plotted *vs.* depletion power and depletion wavelength. The optimum depletion powers are indicated by black circles. Beyond those powers, the behavior is likely dominated by 1PA of the depletion laser. For short depletion wavelengths, the optimum depletion power is lower than for larger wavelengths, consistent with the higher 1PA probability at shorter wavelengths. The maximum threshold shift of 45% is found for the longest depletion wavelength. Missing data for high depletion powers in Fig. 5.11 (b–e) are due to dominating 1PA

for short wavelengths and due to limited depletion power available in our setup at longer wavelengths. Figure 5.11 (c) shows the same plot for timing #2 (where both effects contribute). Clearly, the attainable maximum relative threshold shift of 59% is larger. Furthermore, the optimum depletion powers (black circles) shift towards larger powers, indicating that the fast effect can further limit the effect of parasitic 1PA.

We assume that each depletion component increases the initial threshold by a certain factor. If both effects contribute (like in timing #2), the increased polymerization-threshold power is the undisturbed value multiplied by the factors of both the slow and the fast effect. We can now isolate the threshold increase caused by the fast effect by dividing the increased threshold values from timing #2 (where both effects have contributed) by the corresponding threshold-increase factors $P_{\mathrm{th,shifted}}/P_{\mathrm{th},0}$ of timing #1 (where only the slow effect has contributed) for each wavelength and each depletion power. Using the resulting fictitious shifted threshold values (where only the fast effect would have contributed) we can calculate corresponding relative threshold shifts for the fast effect.

These results are shown in Fig. 5.11 (d). We find that the fast effect gets less pronounced for longer wavelengths. One should keep in mind that by dividing through the values of timing # 1, we probably do not only remove the contributions of the slow effect, but also parts of the limiting contribution of 1PA. Hence, the fact that Fig. 5.11 (d) shows very little saturation towards high depletion powers should be taken with caution.

For a more quantitative evaluation we calculate effective cross-sections for the involved intermediate states according to $\sigma \propto (P^2_{\mathrm{th,shifted}}/P^2_{\mathrm{th},0} - 1)h\nu$ (see Appendix A.2). The corresponding data are depicted in Fig. 5.11 (e), into which data from Fig. 5.11 (b–d) at 10 mW depletion power have entered. The data are normalized to the maximum value of the green curve. For comparison, we plot the absorption spectrum and the spectrum of the stimulated-emission cross-section $\sigma_{\mathrm{SE}}(\lambda) \propto \lambda^4 F(\lambda)$ [76] of DETC in arbitrary units along the vertical axis, where $F(\lambda)$ is the previously measured fluorescence spectrum of the compound. These spectra were taken in PETTA solution. Again, the slow effect (red) gets more pronounced towards longer wavelengths. The combined effective cross-section (green) has its maximum around 532 nm wavelength. The retrieved effective cross-section for the fast component (blue) nicely follows the shape of the stimulated-emission cross-section. We consider this finding a strong indication that the fast depletion effect is actually due to stimulated emission [76].

Last, we want to determine the lifetime of the long-lived intermediate state. As this lifetime exceeds 12.5 ns (which is the temporal pulse separation of our laser system), we use the amplitude modulators in our setup to form pulse bursts with a duration of about 1 µs. The envelopes of such pulse bunches are measured with a silicon photodiode that can not resolve single pulses and depicted in Fig. 5.12 (a). The FWHM of the excitation burst (red) is limited by the AOM used. In these additional experiments, the delay stage is positioned such that the depletion pulses arrive shortly before the excitation pulses (timing #1). Hence, negligible contribution from STED is expected and only the properties of the slow process are probed. We delay the pulse bunches with respect to each other and again write a test array like in Fig. 5.9 (a) for each value of the pulse-burst delay between −2 µs and 2 µs in steps of 0.25 µs. The resulting pulse-burst-delay-dependent relative threshold

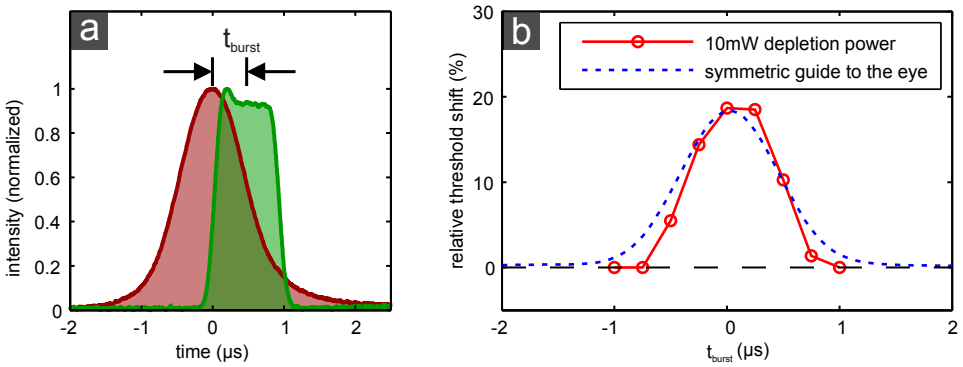

Figure 5.12.: (a) Pulse bursts modulated onto the excitation laser (red) and the depletion laser (green). A delay between their centers $\Delta t_{\mathrm{burst}}$ can be introduced electronically. (b) Observed relative threshold shift *vs.* $\Delta t_{\mathrm{burst}}$. No decay can be resolved on this µ*s* timescale.

shift plotted in Fig. 5.12 (b) shows a slight asymmetry towards the positive delay side. However, a temporal decay cannot be resolved unambiguously. These experiments only provide a firm upper bound for the lifetime of the long-lived light-absorbing intermediate state underlying the slow effect of 1 µs.

Let us briefly recapitulate on the depletion mechanism of DETC and ITX. For DETC, we have found pronounced stimulated emission and weak triplet-triplet absorption in ethanol solution. In the actual photoresist, we have found that DETC can be efficiently deactivated *via* stimulated emission. The S_1 lifetime of DETC in PETTA is roughly 1 ns. Furthermore, we identify a second slower depletion mechanism with a time constant in the range 12.5 ns − 1 µs. The nature of this mechanism is yet to be determined.

For ITX, we find no stimulated emission, but spectrally broad excited-state absorptions from S_1 as well as T_1 in ethanol solution. Hence, stimulated emission is unlikely to play a dominant role. Along the lines of Fig. 5.12, we have done pulse-burst-experiments on the actual ITX-based photoresist (with the cw depletion laser and a pulse-burst width of 7 µs, not depicted). Again, we could not resolve a temporal decay and conclude that the lifetime of the light-absorbing intermediate state responsible for the depletion is on a sub-µs to few-µs scale.

6. Experimental results

6.1. DLW enhancement in the lateral direction

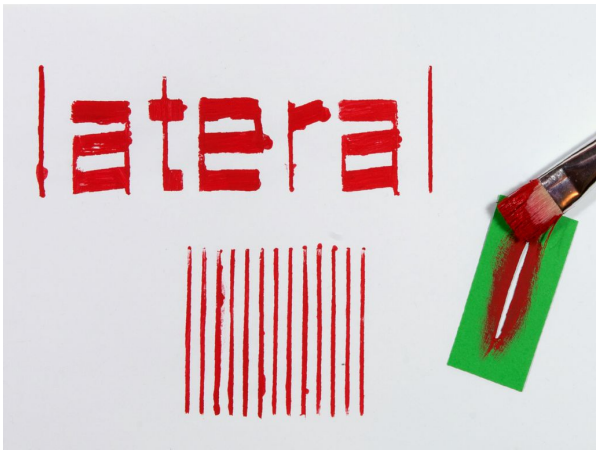

In the previous section, we have shown that stimulated emission is not the dominating depletion mechanism (at least for our standard setup with the cw depletion laser). For ITX, the observed depletion is due to an unknown mechanism, presumably related to excited-state absorption of some kind (compare Section 3.6.4). For DETC, STED is possible but accompanied by a second unknown depletion mechanism. Nevertheless, these unknown mechanisms are suited for super-resolution lithography in principle. The depletion is reversible (see Section 5.5) and the time constants are compatible with fast scanning. Using the upper limits of these time constants (1 µs for DETC and 7 µs for ITX) we deduce maximum scan velocities for a hypothetical 10 nm wide line on the order of 1 m/s. This is more than sufficient for our experimental situation with typical scan speeds of 100 µm/s.

In this section, we will address the lateral directions x and y, *i.e.*, transversal to the optical axis z. First, we will try to reduce the lateral linewidth of exposed lines. Then we will examine whether this also translates to improved resolution as discussed in Section 2.3.2. For this purpose, we use our original STED-inspired DLW setup again (see Section 4.1). In particular, all remaining experiments feature the cw depletion laser (Fig. 4.1), not the pulsed depletion laser used in the previous section (Fig. 5.8).

The data presented in this section have already been published in Ref. [88] and Ref. [91].

6.1.1. The donut depletion-focus

For an optimal confinement of the effective exposure dose along the lateral direction, we choose the donut depletion focus briefly described in Section 3.2. For this purpose, we insert a helical phase mask into the collimated beam of the cw depletion laser. The phase mask is commercially available and purchased from RPC Photonics, Rochester NY, USA. This phase mask imprints a helical phase ramp from 0 to 2π onto the beam. We use the phase pattern designed for 527 nm wavelength, which is the closest to our depletion

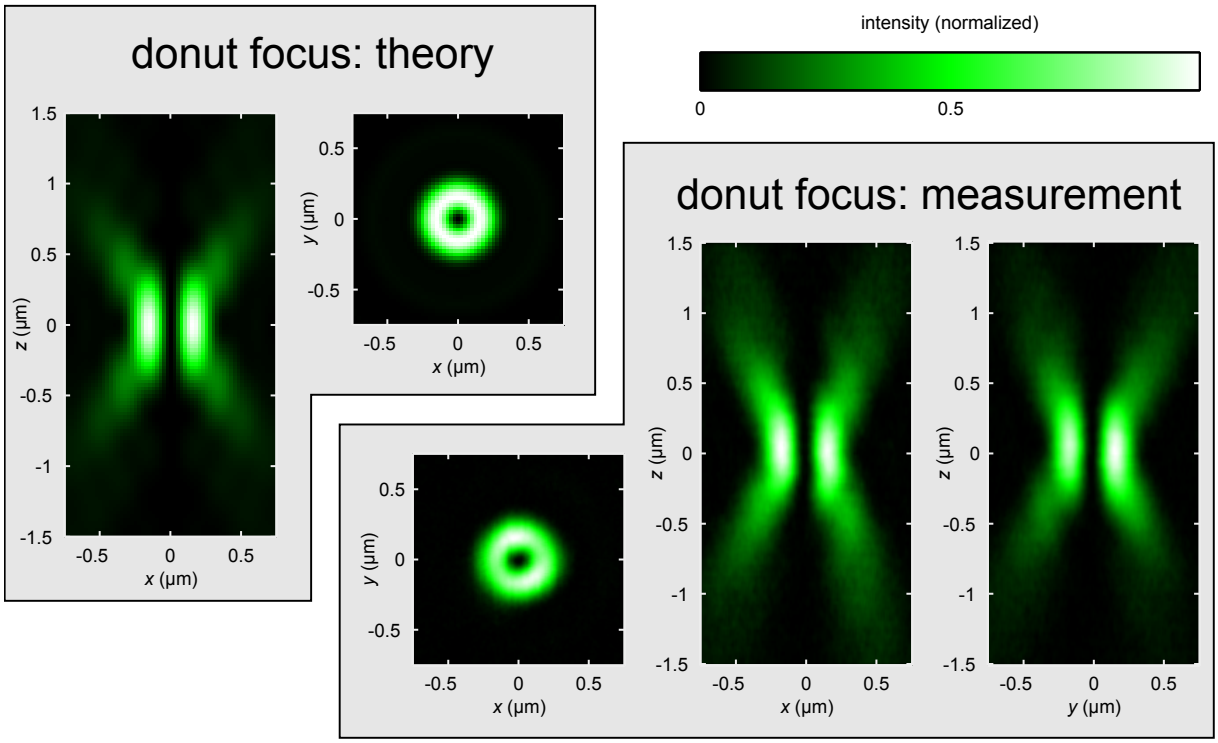

Figure 6.1.: Focal intensity distribution of the 532 nm depletion laser with the helical phase mask inserted. A so-called "donut" focus results. Left side: calculation according to Section 2.2.1. Right side: measurement by scanning a 80 nm gold bead through the focus.

wavelength of 532 nm. This leads to a maximum phase of 1.98π instead of 2π. For the focus, this means that the zero intensity becomes finite and is now 0.03% (from numerical calculations, not depicted). The phase mask is imaged onto the objective's back-aperture like previously described. The intrinsic phase discontinuity in the center and the discontinuity from 1.98π to 0 usually lead to diffraction of the beam. Interference rings and fringes originate from these positions and propagate into the beam with increasing propagation length. When using the imaging system, however, the diffracted light is mainly collected by the lenses and the intensity distribution directly after the mask (*i.e.*, for zero propagation length) is reconstructed at the objective. No interference fringes are visible in the mode profile at the objective position.

The resulting focal intensity distribution is shown in Fig. 6.1. On the left hand side calculations are done for an infinite beam diameter (*i.e.*, constant intensity over the objective's entrance pupil). During the measurements shown on the right-hand-side, the beam was roughly one pupil-diameter in width. The overall agreement between theory and measurement is very good. We think that the origin of the remaining asymmetry in the experimental x-y-slice is most likely caused by the objective lens. We have compared several nominally identical objectives and obtained different results here. Apart from the objective lens, the pronounced tails in the axial slices might also originate from a non-perfect beam profile or a non-perfect phase mask.

The main feature of a depletion focus is the zero intensity region. The minimum intensity is routinely measured to be $< 5\%$. When subtracting an offset caused by the Fresnel reflection at the substrate surface (where the gold beads are positioned) values $< 1\%$ result. With such a deep minimum, the focus should be appropriate to improve the lateral linewidth and resolution in DLW lithography.

6.1.2. Improved lateral linewidth

We have already elaborated on the anticipated linewidth scaling in Section 3.2. To test this behavior experimentally, we write lines directly on the glass-resist interface. Along the lines of Fig. 5.9 (a) we vary the excitation power as well as the depletion power, this time, however, with a cw laser and a donut-shaped depletion focus. The resulting lines are coated with $6-8\,\mathrm{nm}$ gold *via* sputter-coating (Cressington 108 auto) and imaged with an SEM. The widths of the polymer lines are extracted from the electron micrographs.

An alternative method to characterize the linewidth would be to write lines within the photoresist volume attached to supporting massive polymer structures at both ends. Such lines tend to suffer from heavy shrinkage and can have impressively small linewidths [92, 93]. However, to the best of our knowledge, these small feature sizes could not be utilized in a complex 3D structures, so far. Writing lines at the substrate interface does not allow for such pronounced shrinkage in horizontal direction because the lines are rigidly attached to the substrate surface across their whole contact area. Therefore, this method delivers results that are more meaningful.

To ensure that the lines are positioned properly along the z-direction, we measure the position of the substrate-resist interface at several lateral positions of the piezoelectric scanning stage using the Fresnel reflection of the green laser beam in a confocal detection scheme. We also extract the angles of the sample tilt from these measurements and adjust the z-coordinates of the writing trajectories to properly follow the tilted interface. Moreover, we write the test patterns at different z-positions (roughly $\pm 300\,\mathrm{nm}$) to ensure that at least one pattern has an acceptable z-position. Line arrays with a z-position shifted towards the glass-substrate side can be identified by a seemingly high polymerization-threshold power. Here, the threshold iso-intensity surface only fully enters the photoresist at increased excitation powers. Line arrays with a z-position shifted towards the photoresist side fall over or are washed away during the development step. We use lines that are right in between and anticipate that roughly 50% of the voxel volume is located inside the photoresist.

We start with the ITX-based photoresist [88]. The resulting linewidths of a selected series are depicted in Fig. 6.2. In this series, the average excitation power was fixed to $13.5\,\mathrm{mW}$ whereas the depletion power was increased as indicated. The linewidth decreases from an initial value of $155\,\mathrm{nm}$ down to a minimum value of $65\,\mathrm{nm}$ for $80\,\mathrm{mW}$ depletion power [88]. Beyond this depletion-power value, the linewidth increases again. This can be explained by parasitic absorption of the depletion laser by photoinitiator molecules as seen in Fig. 5.9 (a). This unwanted absorption leads to enhanced excitation instead

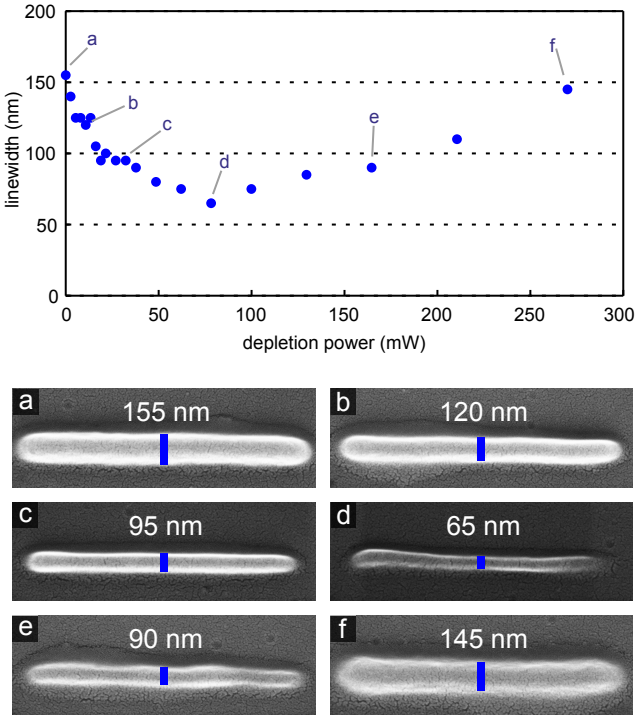

Figure 6.2.: Decrease in lateral linewidths using the ITX-based photoresist. Polymer linewidth *vs.* power of the cw depletion beam that is focused to a donut-shaped mode. The power of the two-photon excitation beam is fixed to 13.5 mW. The subpanels (a–f) exhibit electron micrographs illustrating the raw data underlying the data points. Previously published in Ref. [88].

of depletion. For ITX, we suspect this absorption to be governed by 2PA, based on additional fluorescence depletion experiments (see Appendix A.1).

For the DETC-based photoresist we get similar results. The resulting linewidths are depicted in Fig. 6.3. Again, the minimum attainable linewidth is 65 nm. Here, the optimum depletion power is around 90 mW. Again, we see an increase in linewidth for even higher depletion powers. As this increase is less pronounced and as the overall properties of the DETC-based photoresist outperform those of the ITX-based photoresist, we will use the DETC-based photoresist for the remainder of the work.

The seeming improvement from 155 nm down to 65 nm and from 220 nm down to 65 nm is very large. We have to keep in mind, however, that 100 nm wide lines are also attainable using conventional DLW. When we choose a series with lower excitation power out of the STED-inspired DLW test arrays, we indeed find 100 nm as a starting linewidth with the depletion laser being switched off. In such series, however, the lines tend to be underexposed for a certain depletion-power interval. Usually, as soon as the linewidth has dropped from 100 nm to 80 nm the lines become underexposed and sufficiently exposed again only for large depletion powers (where the linewidth is rising again).

One explanation for this behavior can be found in the scanning exposure scheme applied: Due to the uni-directional scanning, we have to integrate the 3D exposure-dose profile of a

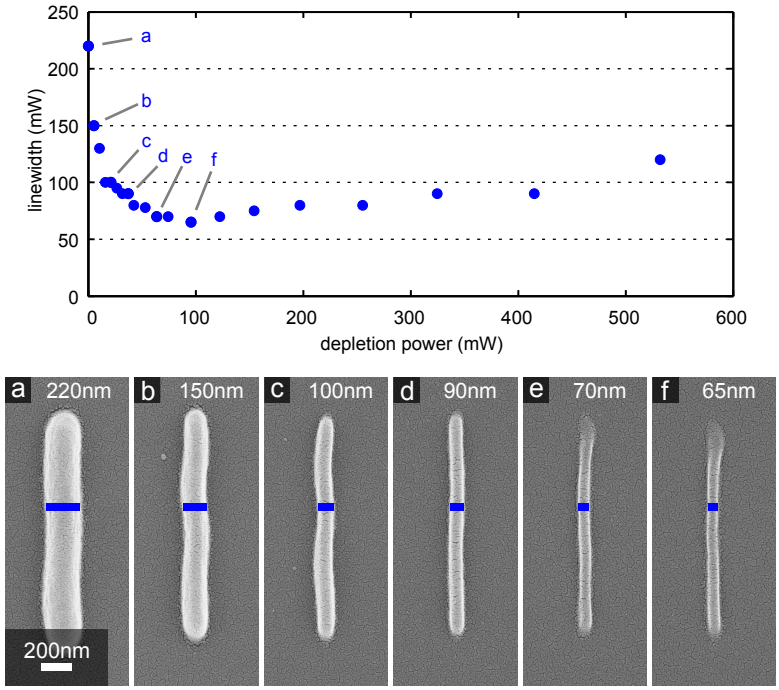

Figure 6.3.: Decreased in lateral linewidths using the DETC-based photoresist. Polymer linewidth *vs.* power of the continuous-wave depletion beam that is focused to a donut-shaped mode. The excitation power was fixed. The sub-panels (a–f) exhibit electron micrographs illustrating the raw data underlying the data points. Previously published in Ref. [94].

single voxel along the scan direction in order to obtain the 2D exposure profile along the polymerized line. When using the donut depletion-focus, the effective exposure profile of a single voxel shrinks in both lateral directions, and hence, also along the direction of scanning. Therefore, the resulting 2D exposure dose of the line (transversal to the scan direction) is not only decreased in width but also in magnitude. As soon as this decreasing peak of a line's exposure dose drops below the polymerization threshold, the lines are underexposed as observed experimentally.

Consequently, the improved linewidth of 65 nm should best be compared to the linewidths attainable in conventional DLW which are commonly believed to be in the range of 80 nm–100 nm [95, 96]. However, during the experiments in this subsection, we could not find linewidths below 100 nm that have been fabricated using conventional DLW and that exhibit proper quality.

The fact that for both photoresists the minimum attainable linewidth is 65 nm (in spite of totally different photoinitiators and laser powers) might be a hint that at this point other factors are already limiting the linewidth. For example, diffusion of the initiating and propagating radicals during the reaction time is likely on this spatial scale. For further improvements, diffusion could be reduced by either increasing the viscosity of the photoresist or by adding radical quenchers that reduce the lifetime of the radicals and, hence, the effective diffusion length.

Moreover, the unwanted absorption of the depletion laser should be eliminated in order to move the observed optimum towards higher depletion powers and lower linewidths. This could be achieved by changing the depletion laser wavelength or by finding better photoinitiators suitable for STED-inspired DLW.

6.1.3. Improved lateral resolution

As we have extensively discussed in Section 2.3, feature size and resolution are not the same. Due to the polymerization threshold, the attainable feature size can be much smaller than the half pitch of an attainable grating. In fact, the linewidth is not truly limited by diffraction, at all. Furthermore, shrinkage during the development stage or even during the SEM imaging can corrupt the measured linewidths and lead to smaller values.

In this section, we explore the minimum attainable lateral period of a line grating. This measurement is rather insensitive to shrinkage effects. Properly separated lines stay separated, even when suffering from subsequent shrinkage. Lines that are not properly separated but bridged by thin polymer filaments will likely stay connected or get distorted when shrinking.

Our simple modified Abbe formula (Eq. 2.11) for the lateral diffraction limit in two-photon DLW states

$$a_{xy} = \frac{\lambda}{2\sqrt{2} \cdot \mathrm{NA}} = \frac{810\,\mathrm{nm}}{2\sqrt{2} \cdot 1.4} = 205\,\mathrm{nm}\,. \tag{6.1}$$

For comparison, the numerical calculations of the two-photon Sparrow criterion yield $a_{xy} = 203\,\mathrm{nm}$.[1] This means that we would not expect any modulation in the exposure dose for a grating of a smaller period.

Benchmark examples from the literature do demonstrate center-to-center distances of $a_{xy} = 300\,\mathrm{nm}$ using 780 nm femtosecond pulses [95] or 532 nm cw exposure [79]. These periods are above the corresponding diffraction limits of $a_{xy} = 196\,\mathrm{nm}$ and $a_{xy} = 134\,\mathrm{nm}$. In fact, we can not find any attempt to break the diffraction barrier with conventional DLW in the literature.

We fabricate a series of gratings as depicted in Fig. 6.4 using the DETC-based photoresist [91]. Again, we vary the excitation power, the depletion power, and the z-position and pick corresponding best results. The excitation power is increased in fine steps of 1% to ensure at least one field has the optimal exposure dose. Furthermore, we systematically decrease the grating period a_{xy} in steps of 25 nm.

Figure 6.4 shows the best results for $a_{xy} = 200\,\mathrm{nm}$ and $a_{xy} = 175\,\mathrm{nm}$ fabricated using conventional DLW and STED-inspired DLW. Both periods are below the lateral diffraction limit. Therefore, assuming a linear accumulation of the exposure dose, we would expect to see no modulation at all for a diffraction-limited approach.

[1] The value $a_{xy} = 200\,\mathrm{nm}$ previously shown in Fig. 2.9 has to be scaled up to the slightly higher excitation wavelength in our setup.

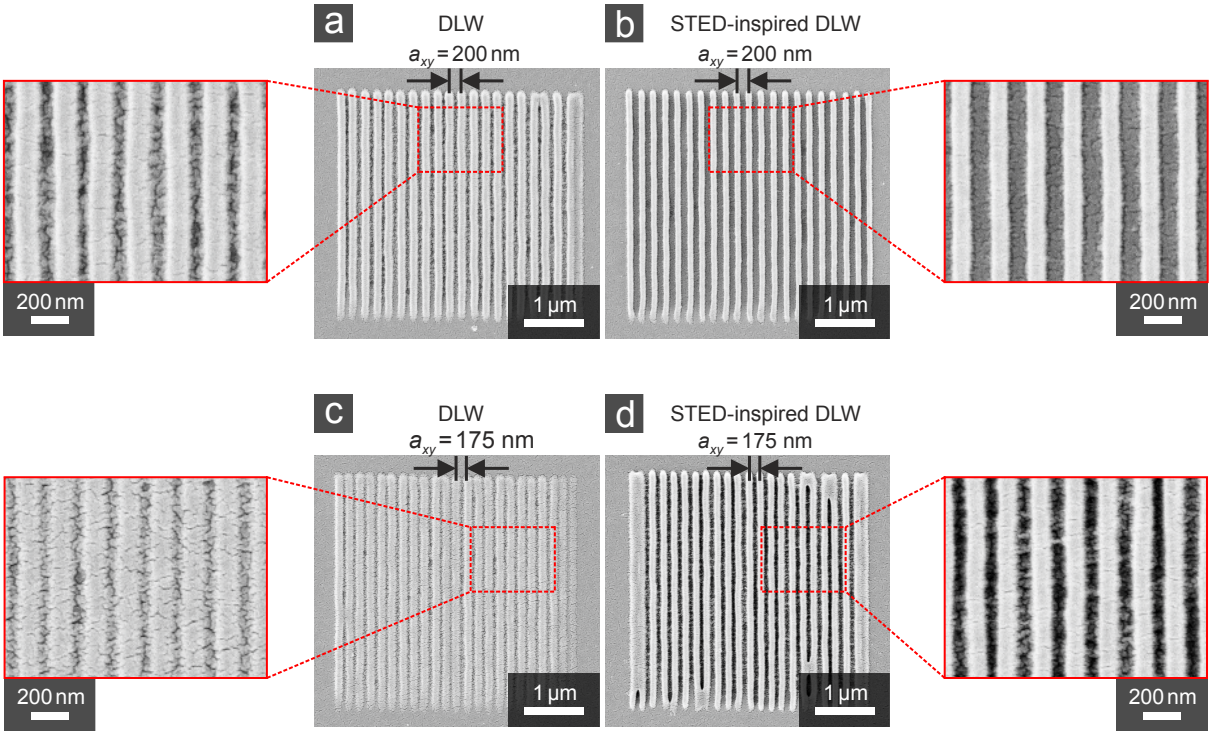

Figure 6.4.: Electron micrographs of simple line gratings fabricated *via* conventional DLW (a, c) and STED-inspired DLW (b, d). The center-to-center distances of the lines are $a = 200\,\text{nm}$ and $a = 175\,\text{nm}$ as indicated within the panels. The depletion power of the donut mode used is 50 mW in front of the microscope-objective-lens entrance pupil. Each panel exhibits an additional zoom-in to reveal finer features. Previously published in Ref. [91].

For conventional DLW we do not get a clean grating with period $a_{xy} = 200\,\text{nm}$ (Fig. 6.4 (a)). The lines are clearly modulated but the spacings in between are bridged by polymer filaments. The fact, however, that we see a modulation at all, tells us that the Sparrow criterion is not a sharp barrier but can in principle be overcome with conventional DLW by utilizing special "forgetting" photoresists (see Section 2.3.1). We are, however, not aware of any high-quality structures beating the Sparrow criterion in conventional DLW from literature.

For a yet smaller period $a_{xy} = 175\,\text{nm}$, we can not get a separated grating with conventional DLW. The image that we show instead (Fig. 6.4 (c)) is a structure where the z-position is shifted towards the glass substrate. In this configuration, only a small part of the voxel is inside the photoresist. In this way, we can only achieve a slight height variation, yet no clear separation and no elevation from the substrate surface.[2] Again,

[2]From an optics point of view, the lateral resolution gets even worse when leaving the $z = 0$ plane of the focus. However, it is often observed that smaller feature sizes are attainable for such buried voxels. This is probably due to the fact that the resulting small aspect ratio makes the structure more robust for the development step.

we can see a modulation below the diffraction limit ("forgetting photoresist"), but the structure quality is poor.

In contrast, using our STED-inspired DLW approach, we can fabricate a grating with $a_{xy} = 200\,\text{nm}$ with excellent quality (Fig. 6.4 (b)). The polymer lines are perfectly separated. To the best of our knowledge, this is the first time a high-quality structure below the diffraction limit has been fabricated using a DLW approach. The width of the lines is roughly 100 nm. This value might be little impressive, but is in fact a direct confirmation of our reasoning about linewidth and resolution: The smallest attainable linewidth within a dense-packed grating is significantly larger than that of a single line. This is due to the accumulation of exposure dose that would have been below threshold in case of an isolated line. While 100 nm linewidth (or even below) is often considered to be state of the art in conventional DLW, a corresponding period of 200 nm is not possible in high quality.

In case of $a_{xy} = 175\,\text{nm}$, we can still achieve a grating that is elevated from the substrate and shows separated lines in decent quality. Clearly, polymer filaments start bridging the lines. Nevertheless, the "modulation depth" is very good.

In conclusion, we have seen in this subsection that the lateral resolution of STED-inspired DLW exceeds that of best conventional DLW [91]. Smaller linewidths and smaller spatial periods have been achieved. Moreover, the fabrication of high quality gratings below the lateral diffraction limit was demonstrated for the first time [91].

6.2. DLW enhancement in the axial direction

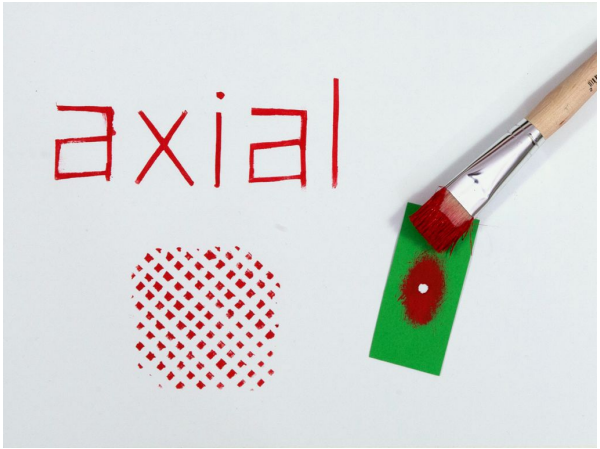

For the fabrication of small complex 3D structures, the axial resolution is even more of a problem than the lateral one. We have already elaborated on this issue in the Sections 2.3.1 and 2.3.2. Clearly, in some sense, the improvement of the lateral direction alone makes the situation even worse, as the aspect ratio of the fabricated voxels further increases. For most applications, however, a spherical voxel (*i.e.*, aspect ratio AR = 1) would be ideal. Therefore, we address the axial z-direction in this section. We will also move from 2D test-patterns on the substrate-photoresist interface to real 3D test structures. The appropriate depletion focus is characterized, and an improved voxel aspect-ratio as well as an improved axial resolution beyond the diffraction limit are presented.

The data presented in this section have already been published in Ref. [91] and Ref. [55].

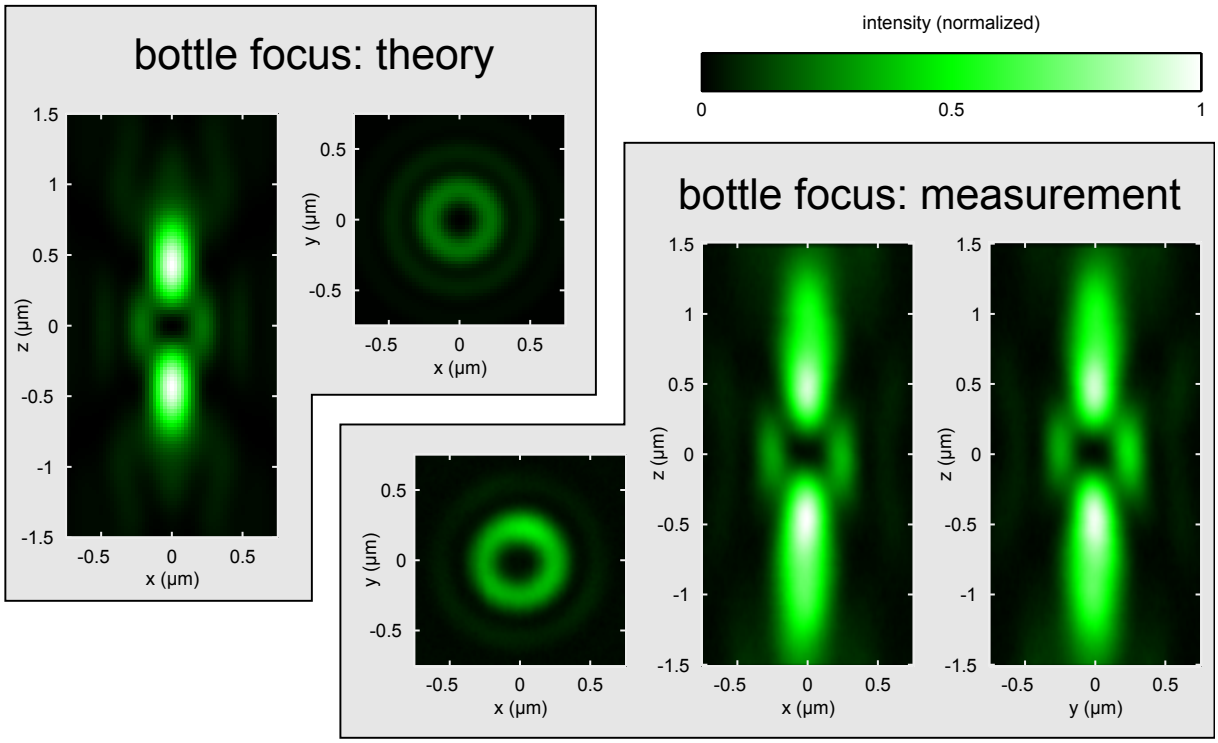

Figure 6.5.: Focal intensity distribution of the 532 nm depletion laser with the circular phase mask inserted. A so-called "bottle-beam" focus results. Left side: calculation according to Section 2.2.1. Right side: measurement by scanning a 100 nm gold bead through the focus.

6.2.1. The bottle-beam depletion-focus

In order to confine the excitation volume in the lateral and also in the axial direction, we use the bottle-beam depletion-focus depicted in Fig. 6.5. The phase mask needed to form this focus consists of two segments that are phase-shifted by π with respect to each other (compare Fig. 3.3 (i)). For an infinite beam diameter (like assumed in the calculations in Fig. 6.5), the inner circular segment covers half of the entrance-pupil area. In this way, the inner beam part and the π-shifted outer rim will lead to a complete destructive interference in the geometrical focus. For a finite beam diameter, the contribution of the outer part is smaller than that of the inner part. Therefore, the equation

$$\int_0^{r_1} \mathrm{d}r \; 2\pi\, r\, |\vec{E}(r)| = \int_{r1}^{r_2} \mathrm{d}r \; 2\pi\, r\, |\vec{E}(r)| \tag{6.2}$$

must be fulfilled, where r_1 is the radius of the inner disc, r_2 is the radius of the objective's entrance pupil, $\vec{E}(r)$ is the electric field strength of the incoming beam depending on the radial distance r from the central beam axis.

We use a home-built phase mask to generate the bottle beam. For this purpose, we spin coat the photoresist SU8-5 onto a standard glass slide, do a standard pre-bake to evaporate the solvent, expose the inner region using a UV lamp through an aluminum mask with a circular aperture, and dissolve the unexposed outer area. The photoresist

itself with its refractive index of roughly $n = 1.6$ serves as the phase-retarding medium. The layer thickness can be controlled by the spin speed. The needed thickness of the final layer is $d = \Delta\phi/(k_0 \cdot \Delta n) = \pi\lambda/(2\pi \cdot 0.57) \approx 443\,\text{nm}$. The minimum film thickness $d = 5\,\mu\text{m}$ for SU8-5 can be obtained by spinning for 60 s at 3000 rpm. To get thinner films, we dilute the photoresist with the solvent γ-butyrolactone (GBA) that is already contained in SU8 resists. This decreases the photoresist viscosity and, hence, the film thickness after spin coating. With a 1:1-dilution of SU8-5 with GBA and with a spin speed of 2400 rpm, we achieve the anticipated optical thickness $n \cdot d$. This quantity is measured by using our Fourier-transform-infrared (FTIR) spectrometer microscope as a reflectometer and measuring the Fabry-Pérot fringes on the reflected spectrum.

The phase mask is inserted into the collimated depletion beam and imaged onto the objective lens. The measured focal intensity distribution is shown on the right hand side of Fig. 6.5. The overall agreement with theory is good. The quality of the innermost part surrounding the zero-intensity point – which is most relevant for STED-inspired DLW – is very good. Again, the measured intensity in the minimum is less than 5% of the peak intensity.

All panels in Fig. 6.5 – both in theory and measurement – are normalized to the peak intensity of the entire 3D focus. Therefore, the x-y-scans have peak values < 1. The fact that the experimental x-y-slice looks brighter than the theoretical one is due to a lower peak intensity in the experimental bottle beam and the normalization procedure.

6.2.2. Improved aspect ratio

Like for the lateral direction, we have to distinguish between feature size and resolution in the axial direction. The axial extent d_z of a single rod is usually significantly larger than the lateral extent d_{xy}. As mentioned before, we use the aspect ratio AR to describe this elongation. Precisely, this quantity is given by $\text{AR} = d_z/d_{xy}$, a typical value for common DLW is $\text{AR} \approx 2.5$.[3]

The bottle-beam depletion-focus is expected to decrease the lateral as well as the axial extent of a single voxel (see Section 3.2). The axial improvement will be more pronounced, as the depletion-focus intensity rises more steeply along the z-direction and the initial excitation volume is also elongated in this direction.

One method to investigate the aspect ratio of a single voxel is the ascending-scan method [66, 98], where single voxels are exposed with increasing z-position. While the first voxels are "buried" within the substrate, the centers of sub-sequent point exposures move towards the photoresist half-space. Eventually, some voxels will not have physical contact to the substrate during the exposure. These voxels will fall down to the substrate and may survive the solvent wash lying on the substrate surface. Voxels with $\text{AR} > 1$ will usually fall over and have their long axis positioned parallel to the substrate surface. In this way, they can be easily characterized *via* SEM imaging. However, not being

[3] While common DLW using $\text{NA} = 1.4$ should yield $\text{AR} \approx 2.5$ in theory, larger values up to $\text{AR} \approx 5$ can be found in the literature [66, 97]. These larger values could result from optical aberrations or from the underlying polymerization chemistry.

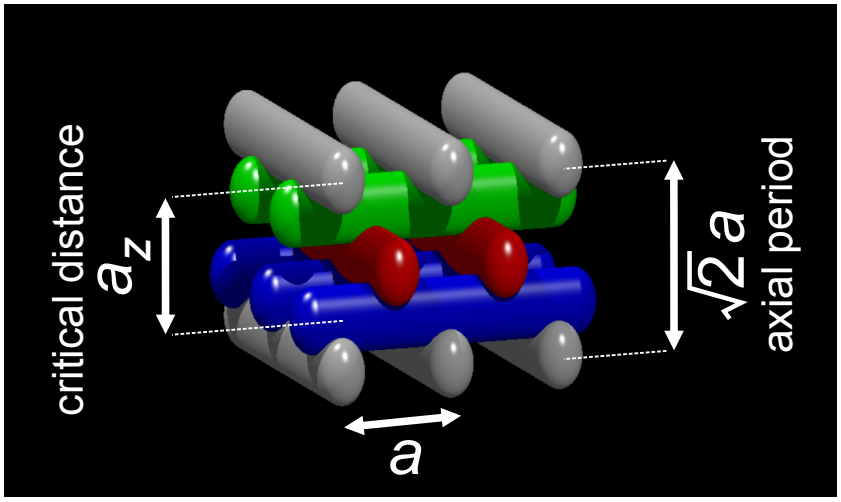

Figure 6.6.: Scheme of a 3D woodpile photonic crystal [99]. The woodpile is composed of a first layer (gray) of periodically arranged dielectric rods with rod spacing a, a second orthogonal layer (blue), a third layer (red) laterally displaced by half the rod spacing with respect to the first layer, and a fourth layer (green) displaced with respect to the second layer. This pattern is repeated along the axial direction. For a face-centered cubic (fcc) woodpile, the resulting axial period is given by $\sqrt{2}a$. In a woodpile, the smallest axial distance a_z equals 3/4 of this axial period. Previously published in Ref. [55].

attached anywhere, these voxels may be subject to strong shrinkage. Moreover, the SEM-characterization tends to alter small polymer features leading to further shrinkage.

Therefore, we decide to use a real 3D test structure. If the polymer lines can still form a complex 3D structure, we can exclude devastating shrinkage effects. Such effects could render single voxel experiments non-conclusive or meaningless for real-world 3D structuring.

As a 3D test structure, we use the "woodpile" photonic crystal [100]. This structure is well studied in the literature and corresponding experimental results have been published by many groups [7, 9, 10, 30, 79, 101, 102]. A schematic illustration of the structure of such a woodpile is depicted in Fig. 6.6. It consists of a first layer of rods (grey) that are equally spaced by a lateral rod spacing a. A second layer (blue) is rotated by 90° around the z-axis and added on top of the first one. The third layer (red) corresponds to the first one, yet shifted by $a/2$ along the direction of the lateral periodicity. The fourth layer (green) corresponds to the second one, again shifted by $a/2$ with respect to the second layer. This pattern is then periodically repeated in the z-direction. This axial period c is usually chosen as $c = \sqrt{2}a$ yielding a face-centered-cubic (fcc) symmetry of the resulting lattice. The corresponding layer-to-layer spacing in z-direction is $\sqrt{2}a/4$.

As mentioned above, we expect the polymer rods to decrease in size in both the lateral and the axial direction if we hold the excitation power constant and increase the depletion power. Clearly, as soon as the rods are so thin that the layers of the woodpile do not touch any more, the structures will collapse. To resolve this issue, we adjust the lateral

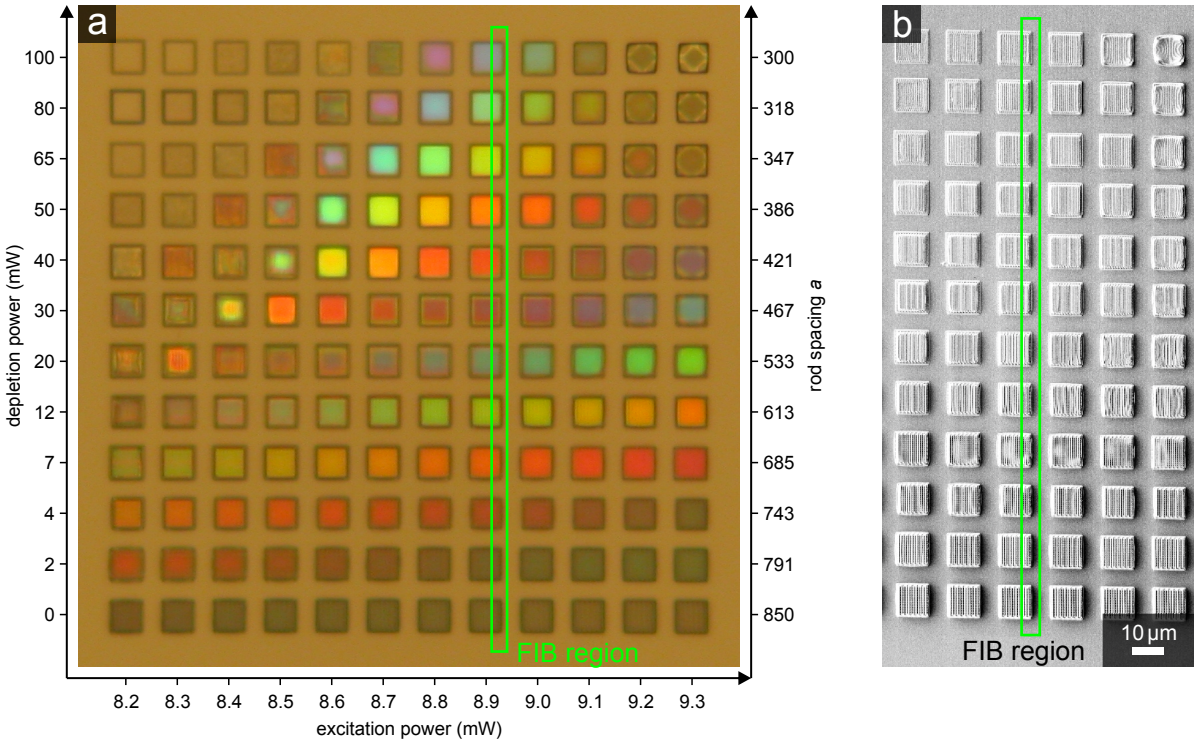

Figure 6.7.: (a) Test array of woodpile photonic crystals. Excitation power and depletion power are varied along the horizontal and vertical axis, respectively. With increasing depletion power, the rod spacing a is decreased to maintain a constant polymer volume filling-fraction (see vertical axis on the right). (b) SEM image of a smaller part of the same array, now filled with ZnO *via* atomic layer deposition (ALD). Green rectangles mark the area that will be removed using focused-ion-beam (FIB) milling.

rod spacing a and the layer-to-layer distance with increasing depletion power, such that the relative volume-content of polymer stays roughly the same. The appropriate function $a(P_{\mathrm{depl}})$ is found empirically in few experimental iterations. The final series of test-woodpiles is depicted in Fig. 6.7 (a). In this reflection-mode optical micrograph, every square is a small woodpile photonic crystal with roughly $10\,\mu\mathrm{m} \times 10\,\mu\mathrm{m}$ footprint and 10 layers. The colors of the squares are due to Bragg reflection off of the photonic crystals.

All z-coordinates of the writing trajectories were increased by 30% to account for shrinkage and defocus due to the refractive-index mismatch. In other words, for an anticipated axial periodicity $c = \sqrt{2}a$, we write a pre-stretched woodpile with $c = \sqrt{2}a \cdot 1.3$. Moreover, to reduce unwanted excitation by the depletion laser, we modulate pulse bursts with 4 kHz frequency and 3% duty cycle onto both laser beams (see Appendix A.3) using the arbitrary function generators described in Section 4.2. To ensure a fair comparison, the experiments with common DLW will also use this scheme. We will stick to the scheme for all remaining sections of this thesis. The powers quoted in the text correspond to the powers during the modulators' "on" phases. In other words, we average the power

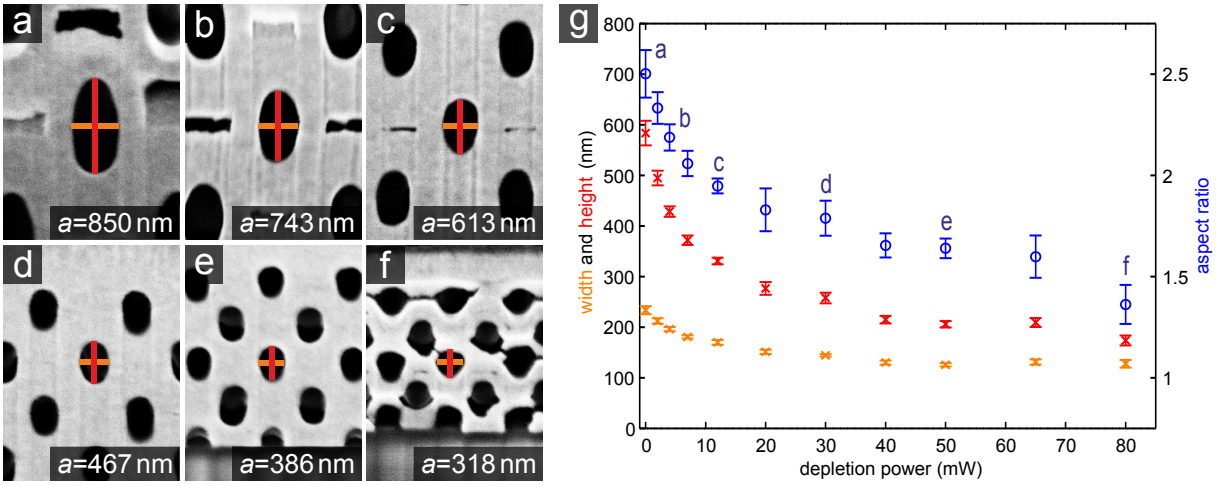

Figure 6.8.: (a–f) Oblique-view electron micrographs of ZnO-filled woodpile photonic crystals after FIB milling. The viewing angle with respect to the surface normal is 54°. (g) Width, height and calculated aspect ratio of polymer rods inside the three-dimensional woodpiles shown in (a–f). Height measurements have been corrected for the viewing angle. The measurements are averaged over 10 rods. The error bars indicate ± one standard deviation of the corresponding ensembles. The bars for height and width in (a–f) correspond to the averaged values shown in (g). Previously published in Ref. [91].

over the ultrafast pulses of the excitation laser, but not over the modulated pulse bursts described in Appendix A.3.

To ensure that the fabricated test structures are not altered by the SEM, we infiltrate the polymer structures with ZnO *via* atomic-layer deposition (ALD) using a commercial ALD machine (Cambridge NanoTech Inc., Savannah 100). In this way, nearly all air gaps between the polymer rods disappear and the polymer is embedded in a very rigid and resistive solid. The deposited ZnO is conductive enough to enable electron microscopy without an additional gold coating. Figure 6.7 (b) shows an SEM image of the same array as in (a), now encapsulated in a ZnO matrix.

For a fixed excitation power the resulting composite structures are opened *via* focused-ion-beam (FIB) milling to reveal their interior. The region to be removed is marked in Fig. 6.7 as green rectangle. During this step, the initial polymer structures are partly calcined, such that essentially holes in ZnO blocks remain. The opened structures are then imaged using an SEM. The viewing angle to the substrate normal is 54°. Figures 6.8 (a–f) show the resulting images. The ZnO appears as a bright grey surface. The FIB-cuts through the massive ZnO are planar and well-defined. The inner ZnO surfaces were used as a measure for the initial polymer lineshape (see bars in panels (a–f)).

The height and width of the initial polymer-rod shape is measured for ten rods for each depletion power.[4] Ten measurements are averaged for each depletion-power value and the

[4]The heights measured in the SEM images have to be multiplied by $1/\sin(54°) \approx 1.236$ to account for the oblique viewing angle.

average width and height are plotted in Fig. 6.8 (g). The average aspect ratio is calculated as the ratio of these average values and also plotted in Fig. 6.7 (g).

As expected, the lateral and axial extent of the lines decreases with increasing depletion power. As the axial extent decreases more rapidly, the AR is decreased as well. The aspect ratio of the rods without depletion laser is AR = 2.5, as expected. With increasing depletion power, the aspect ratio decreases towards AR = 1.6.

The further decreased aspect ratio for $> 80\,\mathrm{mW}$ depletion power is probably influenced by increased shrinkage. The exposure dose integrated along the scan direction is continuously decreased because the exposure volume is also confined in both lateral directions (compare Section 6.1.2). Therefore, the overall exposure dose might get too close to the threshold and lead to pronounced shrinkage at high depletion powers.

One might fear that this positive effect is restricted to the proximity of the substrate-photoresist interface. Spherical aberrations due to the slight refractive-index mismatch between substrate and photoresist will distort the bottle-beam depletion focus (and especially destroy the zero-intensity point) when focusing deep into the photoresist. However, numerical calculations with the code from Section 2.2.1 predict that up to a depth of $10\,\mu\mathrm{m}$ no significant problems should arise. Both laser foci might experience further optical aberration due to the fact that we have to build our structures from bottom up and the beams are therefore focused through polymerized material.[5] The polymerization process increases the refractive index from 1.484 to 1.528 [78]. To check that the improved aspect ratio can be used deeper inside the photoresist volume, we fabricate a woodpile with more than 10 layers.

It is common in two-photon DLW as well as in two-photon microscopy to slightly increase the excitation laser power when focusing deeper into the sample. The total amount of two-photon absorbed photons would otherwise decrease with increasing depth, as aberrations decrease the peak intensity and the 2PA is depending on the intensity quadratically. Moreover, in case the zero intensity of the bottle beam gets finite when focusing deep into the samples, we would also expect a drop in the effective exposure dose due to the enhanced depletion. To compensate for this exposure-dose drop, we use a linear power increase following the formula

$$P_{\mathrm{exc}}(z) = P_{\mathrm{exc}}(z = 0) \cdot (1 + f \cdot z)\,, \tag{6.3}$$

where $P_{\mathrm{exc}}(z)$ is the compensated excitation power, $P_{\mathrm{exc}}(z = 0)$ is the excitation power when writing at the substrate-photoresist interface, z is the distance to the substrate, and $f = 0.0037\,\frac{1}{\mu\mathrm{m}}$ is the empirically calibrated compensation constant. For shrinkage pre-compensation, we have stretched the writing files by a factor of 1.365 along the z-direction.

In this case, the final woodpile structure is developed, coated with a thin gold film *via* sputter coating, and opened with the FIB. No ZnO ALD is applied. An SEM image of the polymer structure's interior is depicted in Fig. 6.9 (a). The footprint of the structure

[5] This is due to the inverted microscope geometry and the liquid photoresist. If we started with the uppermost layer, the polymerized lines would quickly swim away before the exposure would have been completed.

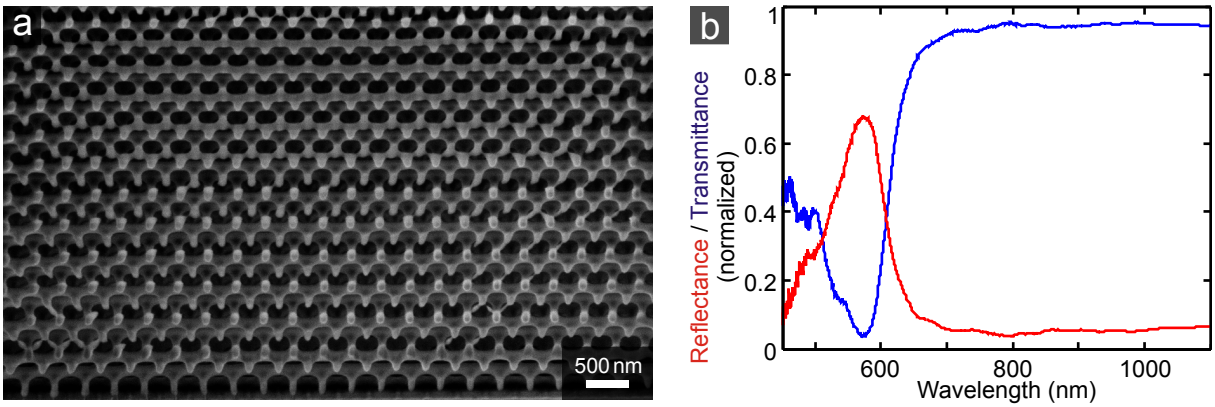

Figure 6.9.: (a) Oblique-view electron micrograph of a woodpile photonic crystal with 52 layers and a rod spacing of $a = 350\,\text{nm}$ made by STED-inspired DLW. The sample has been milled with a FIB to reveal its interior. (b) Corresponding reflectance and transmitted spectra (normalized to substrate transmittance and the reflectance of an 80 nm silver film, respectively). Previously published in Ref. [91].

is $70\,\mu\text{m} \times 70\,\mu\text{m}$, the lateral rod distance is $a = 350\,\text{nm}$, and the anticipated number of layers was 92. With the above simple linear excitation-power compensation we can only achieve 52 layers; all above layers are under-exposed and have collapsed during development. However, over the range of 52 layers (that equal roughly $6.5\,\mu\text{m}$ height) the sample quality is excellent. The alignment is very good, the aspect ratio is very low and homogeneous over the entire height. The filling fraction is low, the rods are perfectly separated, and no strong distortions of the structure are visible.

The optical characterization of the structure (that has been done before the gold coating and FIB milling) confirms the excellent sample quality. The transmission and reflection spectra depicted in Fig. 6.9 (b) show a pronounced and very deep stop band. The spectra were taken using a commercial FTIR-spectrometer microscope (Bruker Equinox 55). The used Cassegrain objective (Opticon 36×, NA = 0.5) illuminates the sample in the angular interval $15° - 30°$ from the optical axis. The transmission drops down to below 3.5% within the stop band.

Obviously, optical aberrations are no big issue for the fabrication of 3D nanophotonic structures with moderate heights of several microns. For yet larger heights, a more sophisticated power compensation or eventually an adaptive aberration correction using deformable mirrors or spatial light modulators could be applied [103].

Another option to circumvent the optical aberrations is to use a photoresist with the same refractive index as the immersion medium. In this way, spherical aberrations due to the refractive-index mismatch are avoided. Starting the writing process in the layer with the largest distance from the objective lens would avoid additional aberrations resulting from the focusing through a partly polymerized structure. A clever implementation by the Nanoscribe GmbH [18] uses the photoresist as immersion medium, which also eliminates the height constraints usually given by the microscope objective's free working distance [40].

6.2.3. Improved axial resolution

Having demonstrated an improved aspect ratio, the question arises whether this also directly translates to an improvement in the axial resolution. For a demonstration of a certain axial resolution, we have to write a structure that is periodic in the axial direction or at least one that contains features that share the same lateral position and are separated by small axial distances. The woodpile photonic crystal can again serve as a benchmark structure here. The smallest axial distance in such a structure equals three times the layer separation. Figure 6.6 illustrates this distance between the blue and the upper grey layer of rods. Although the rods are oriented in different directions, they include voxels that are shifted in the axial z-direction only. The critical distance for a fcc-woodpile is therefore given by $a_z = 3/4c = 3/4\sqrt{2}a$.

For the present experimental parameters, our simple modified Abbe formula (Eq. 2.12) approximating the two-photon Sparrow criterion in the axial direction states

$$a_z = \frac{\lambda \cdot \mathrm{AR}}{2\sqrt{2} \cdot \mathrm{NA}} = \frac{810\,\mathrm{nm} \cdot 2.5}{2\sqrt{2} \cdot 1.4} = 511\,\mathrm{nm}\,, \tag{6.4}$$

where AR = 2.5 is the aspect ratio of the excitation volume. According to the model of a "non-forgetting" photoresist, we would expect no exposures separated by smaller axial distances can be achieved with a diffraction-limited approach. The numerical evaluation presented in Fig. 2.9 states $a_z = 506\,\mathrm{nm}$ (corrected for the different excitation wavelength). We will use the numerical value.

For a woodpile photonic crystal with fcc symmetry, this diffraction-limited critical distance a_z would equal a lateral rod spacing of $a = 4a_z/(3\sqrt{2}) = 477\,\mathrm{nm}$. However, as stated earlier, we usually increase the z-spacing of the writing trajectories to pre-compensate for shrinkage. In order to not misinterpret shrinkage as increased resolution, we use the spacing of the initial exposure trajectories for the resolution measurement. The slight defocus due to the refractive index mismatch is neglected. With a shrinkage pre-compensation of 28% taken into account, we reach the critical axial spacing of the exposure trajectories for a lateral rod spacing $a = 4a_z/(3\sqrt{2} \cdot 1.28) = 373\,\mathrm{nm}$.

To the best of our knowledge, the smallest rod spacings with conventional DLW in fcc or bcc woodpiles published to date are $a = 600\,\mathrm{nm}$ using near-infrared femtosecond pulses [30], $a = 500\,\mathrm{nm}$ using 520 nm wavelength femtosecond pulses [102], and $a = 450\,\mathrm{nm}$ using 532 nm continuous-wave exposure [79]. However, none of these demonstrations are below the corresponding diffraction limits.

A very recent publication using a photoresist containing a radical quencher has achieved $a = 400\,\mathrm{nm}$ with 800 nm femtosecond pulses and slow scanning [104]. Missing FIB-cutting and detailed spectral characterization of the structures, the presented top-view SEM images leave the quality of the interior (especially along the axial direction) questionable.

In order to get a fair comparison between our conventional DLW and STED-inspired DLW, we write a large series of woodpiles with both techniques. All woodpiles have a footprint of $20\,\mu\mathrm{m} \times 20\,\mu\mathrm{m}$, 24 layers and are shrinkage pre-compensated by 28% along the z-direction. Furthermore, the excitation power is slightly increased with increasing distance between

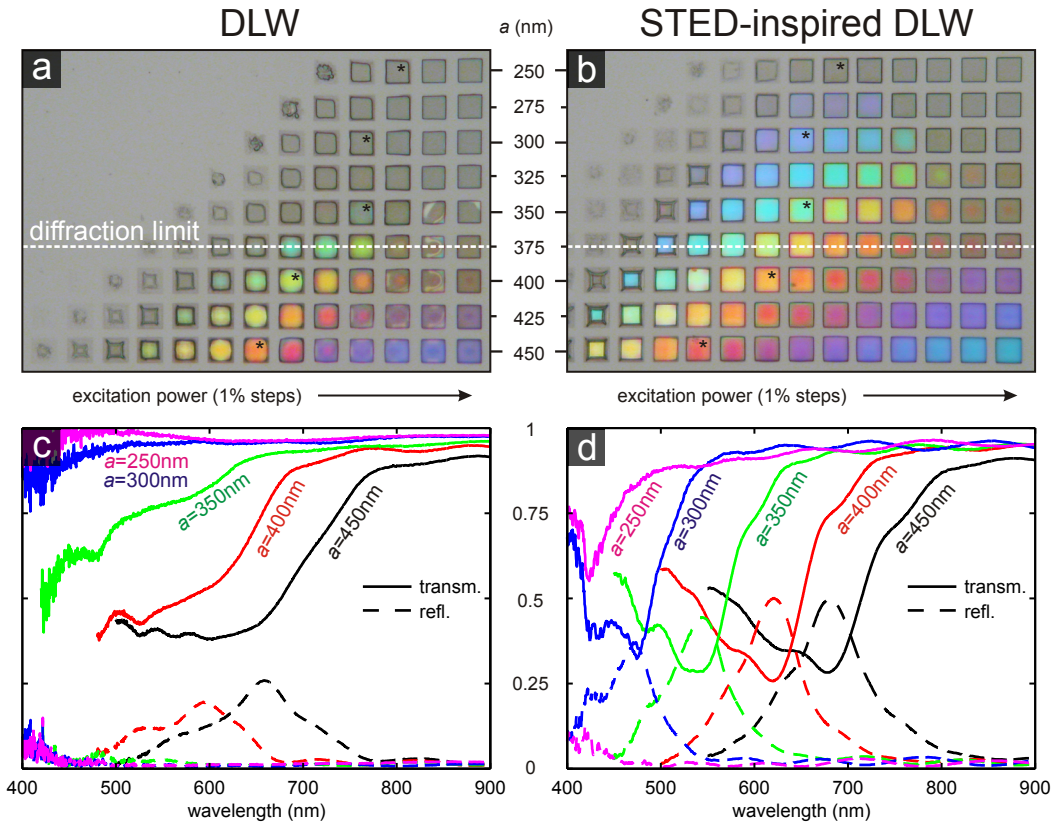

Figure 6.10.: (a) True-color reflection-mode optical micrographs of woodpile photonic crystals fabricated *via* conventional DLW. (b) The same, but using STED-inspired DLW. All woodpiles have 24 layers and a footprint of 20 µm × 20 µm. The rod spacing is decreased from $a = 450$ nm to $a = 250$ nm along the vertical, the exposure power is increased in relative steps of 1% from left to right. The axial diffraction limit is indicated by the white dashed lines. (c, d) Selected transmittance (solid) and reflectance (dashed) spectra for DLW and STED-inspired DLW, respectively (see asterisks in (a, b)). Previously published in Ref. [91].

the writing spot and the substrate (see previous section). We systematically decrease the lateral rod spacing a and connected to that the axial period $c = \sqrt{2}a \cdot s = \sqrt{2}a \cdot 1.28$, where s is the shrinkage pre-compensation factor. For the conventional-DLW reference experiment, the depletion laser is switched off. For the structures fabricated with STED-inspired DLW, the depletion laser power was set to 50 mW. To ensure optimal exposure doses for both techniques and all rod distances a, we perform exposure-dose tests for all combinations. We find that the optimum excitation powers for STED-inspired DLW with 50 mW depletion power are 31% higher compared to the optimum powers for conventional DLW.[6]

Reflection-mode optical micrographs of the final test patterns after development are depicted in Fig. 6.10 (a) and (b) for conventional DLW and STED-inspired DLW, respectively. Each square in the images corresponds to a woodpile structure. Again,

[6] Again, we modulate pulse bursts with 3% duty cycle on both the excitation laser and the depletion laser (see Appendix A.3). In the conventional-DLW reference experiments, we use the same modulation.

the colors correspond to Bragg reflections and are a sign for good sample quality. The rod spacing a is changed along the vertical axis. The largest value of $a = 450\,\text{nm}$ is already among the smallest ones reported in the literature. The axial Sparrow diffraction-limit for our experimental parameters is marked as white dashed line in Fig. 6.10 (a) and (b). The woodpiles in each row correspond to a fine excitation-power sweep in steps of 1% around the previously determined optimal value.

When looking at the images, we see that the woodpiles fabricated with STED-inspired DLW look brighter in color and are more homogeneous. The woodpiles fabricated *via* conventional DLW seem to suffer from shrinkage in the corners resulting in a darker tone or missing Bragg colors. Clearly, with STED-inspired DLW smaller rod distances down to $a = 275\,\text{nm}$ are feasible and show Bragg reflections. For a fixed lateral rod spacing a, the range of excitation powers that yields open colorful structures is much larger for STED-inspired DLW, indicating a higher resolution and higher robustness of the approach. Rod spacings below the axial diffraction limit are clearly possible with STED-inspired DLW (compare white dashed line in Fig. 6.10 (b)).

For conventional DLW, we see some weak Bragg reflection for woodpiles with $a \leq 375\,\text{nm}$. Again, like seen in Section 6.1.3, the axial Sparrow criterion (which corresponds to a lateral rod spacing $a = 373\,\text{nm}$) does not seem to be a sharp barrier. Again, high quality structures below the axial diffraction limit are not possible with common DLW.

To compare the structure quality more quantitatively, we measure the transmittance and reflectance spectra of all depicted woodpiles. For a-values of 450 nm, 400 nm, 350 nm, 300 nm, 300 nm, and 250 nm the best spectra[7] for both methods are plotted in Fig. 6.10 (c, d). The structures corresponding to these spectra are marked by asterisks in the above optical images.

For conventional DLW, we see some stop bands for $a = 450\,\text{nm}$ and $a = 400\,\text{nm}$. The broad shape of the stop bands and the fact that the transmission is not considerably rising when leaving the stop band towards shorter wavelengths does imply a low structure quality. For yet smaller a-values (*i.e.*, structures below the axial diffraction limit) no defined stop band can be observed. In sharp contrast, the structures fabricated *via* STED-inspired DLW show pronounced stop bands throughout all the visible spectrum, down to rod spacings of $a = 300\,\text{nm}$. The increasing transmission at the short-wavelength side of the stop bands together with the high reflectance values at the stop-band centers indicate excellent sample quality. Even the smallest rod spacing $a = 250\,\text{nm}$ shows indications for a stop band in the UV spectral region.

For STED-inspired DLW, the smallest rod spacing a that still shows colors in the optical micrograph is $a = 275\,\text{nm}$. This value corresponds to an axial separation of the initial exposure trajectories of $a_z = 3/4\sqrt{2}a \cdot s = 373\,\text{nm}$. This value is clearly below the axial two-photon Sparrow criterion of $a_z = 506\,\text{nm}$. To the best of our knowledge, this is the first time the axial diffraction barrier has been broken in optical lithography.

[7] The spectra of high-quality woodpiles possess stop bands with low transmittance and high reflectance values. While the transmittance can also be lowered by a disordered interior that scatters light out of the detection cone, a high reflectance is a definite sign for high quality. We have chosen the spectra with the highest reflectance values.

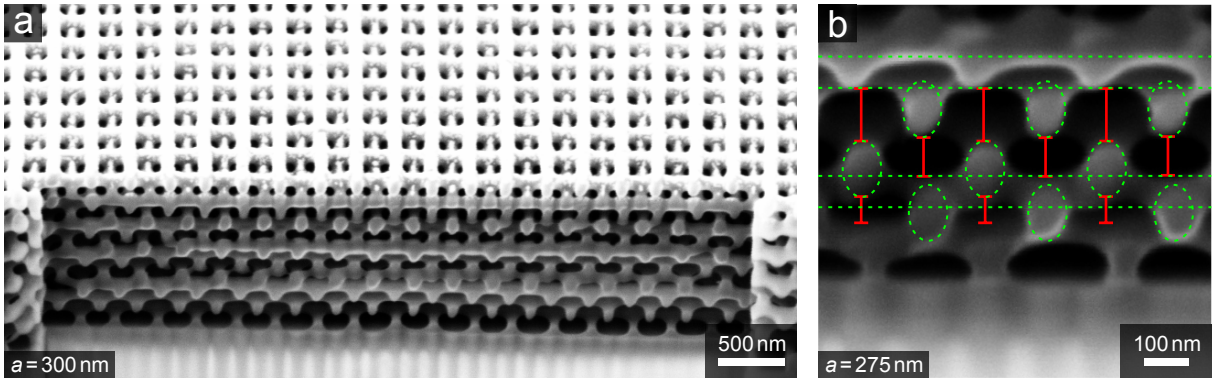

Figure 6.11.: FIB cuts of woodpile photonic crystals with distances below the axial diffraction limit. (a) $a = 300\,\text{nm}$. (b) $a = 275\,\text{nm}$. Critical distances are marked with red bars. Clearly, these critical points are all well separated and a sub-diffraction resolution is demonstrated.

DLW-written structures that are exposed with excitation-laser powers very close to the polymerization threshold usually suffer from heavy shrinkage. The same will hold for STED-inspired DLW operated close to the threshold. Therefore, we do not expect the quality of the smallest rod spacings in Fig. 6.10 (b) to be outstandingly good. Nevertheless, to ensure the structures are open and the rods shifted by the critical a_z are indeed separated, we open some structures with $a = 300\,\text{nm}$ and $a = 275\,\text{nm}$ on a nominally identical sample with the FIB and image the interior with the SEM. Figure 6.11 (a) shows a FIB cut of a polymer woodpile with $a = 300\,\text{nm}$. The features are nicely separated, the short and long-range order is very good. The structure with $a = 275\,\text{nm}$ is depicted in Fig. 6.11 (b). Here, the structure quality is affected by strong shrinkage. While shrinkage at low exposure doses is an inherent problem of 3D DLW and also STED-inspired DLW, we have noticed that a significant part of the shrinkage seen in this structure occurred during the FIB milling. Nevertheless, the rods of the woodpile are still clearly separated at the critical points (marked with red bars) where the axial distances of the exposure trajectories were significantly below the axial two-photon Sparrow limit.[8] Therefore, despite of the only decent quality of the woodpiles with $a = 275\,\text{nm}$, these structures demonstrate a resolution that is 36% beyond the axial diffraction limit ($\frac{373\,\text{nm}}{275\,\text{nm}} = 1.36$).

[8]The different lengths of the red bars originate from the 54° viewing angle in combination with different depth-positions of the horizontal polymer rods in the image.

6.3. Application in nanophotonics: The carpet cloak

At the end of the day, STED-inspired DLW should prove to be superior over common DLW, ideally in all major performance aspects. The above benchmark tests have shown that the resolution of STED-inspired DLW exceeds that of common DLW indeed. Clearly, this increased resolution should quickly lead to new applications and open new possibilities in the fabrication of, *e.g.*, nanophotonic devices. Otherwise, one could get suspicious whether this new approach is only attractive on paper and is for some reason not applicable to every day tasks.

The miniaturized woodpile structures from Section 6.2.3 are already very promising for future applications. Furthermore, transferring these woodpile polymer-templates to higher-refractive-index materials can open a complete photonic bandgap [105]. In 2010, I. Staude *et al.* [30] could demonstrate a 3D structure with a complete photonic bandgap at telecommunication wavelengths around $\lambda = 1550\,\mathrm{nm}$ using a silicon replication of a polymer woodpile with $a = 600\,\mathrm{nm}$. While this rod-spacing was considered to be state of the art only two years ago, we can now access rod spacings down to $a = 300\,\mathrm{nm}$ in very good quality. Given this improved resolution of our novel approach, even complete photonic bandgaps at visible wavelengths are in reach: With a lateral rod distance of $a = 310\,\mathrm{nm}$ and a novel TiO_2 double-inversion procedure developed by Andreas Frölich in our group, complete photonic bandgaps at around 700 nm wavelength are feasible.

In this following section, we describe the application of STED-inspired DLW to another particularly demanding photonic nanostructure, the so-called "carpet cloak". We point out that the fabrication of such a 3D carpet cloak would have been very demanding (if not impossible) for any alternative nanofabrication approach [55]:

Any purely periodic 3D nanostructure can likely be made inexpensively and on a large scale by optical interference lithography. Any simple layer-by-layer structure can be made by standard electron-beam lithography of the individual layers and successive planarization and stacking of layers. Challenges, however, do arise for these and other technologies in case of seemingly simple problems like achieving free-form surfaces in 3D space or 3D architectures which are intentionally non-periodic [55]. The carpet invisibility cloak to be described in this section comprises all of these difficulties at the same time and, hence, represents an interesting and challenging test case with a specific function. Indeed, STED-inspired 3D DLW has enabled the first (and so far also the only) 3D polarization-independent visible-frequency broadband carpet invisibility cloak [106].

The invisibility cloak described in this section has been designed, fabricated, and characterized in collaboration with Tolga Ergin. Further details on design and characterization can be found in his PhD thesis [107] and the journal publications Ref. [106, 108, 109].

6.3.1. Basic principle

Transformation optics is a new design tool in optics that allows to mimic the light propagation within curved spaces with specially tailored optical materials [110, 111]. A particularly impressive example is invisibility cloaking [112, 113]. Herein, an object is physically cloaked by re-guiding light-rays that would have hit the object in absence of the cloaking device. Often times, a spatial compartment is created that can not (or only very weakly) be penetrated by an impinging light wave. The existence of this compartment is then camouflaged by a tailored passive optical device surrounding it. The optical parameters of this device can be derived from transformation optics.

While the design freedom in transformation optics is huge, the optical parameters derived from this theory may have extreme or hard to implement values. Usually, an inhomogeneous distribution of anisotropic optical parameters results. Moreover, diverging, negative, or zero parameters can occur. In general, the permeability is required to be proportional to the permittivity. Using low loss materials, a limited range of permittivities is accessible experimentally. While, for common materials, the permeability at optical frequencies is unity, optical metamaterials provide the means to vary this quantity. However, tuning the permeability and reaching extreme values for the permittivity usually require the use of metals and lead to strong absorption losses at optical frequencies.

The concept of the carpet cloak [114] relaxes these experimental challenges, as its optical parameters can, in very good approximation, be reduced to an isotropic, inhomogeneous permittivity-distribution with constant permeability. Moreover, the required range of permittivities is decent; no diverging or below-one values are inherently necessary.

The scenery for such a carpet cloak contains a half space of a dielectric medium with a reference refractive index n_{ref} and a reflecting mirror – the "carpet" – at one boundary (see Fig. 6.12 (a)). Incoming light rays will be reflected without any distortion. If one would look into such a mirror, he would see an undistorted image of oneself. Now, we introduce a bump into this mirror (Fig. 6.12 (b)). The space below this bump can be used to hide some arbitrary object under the carpet. The bump will, however, impose aberrations on the incoming light field. The distorted reflected image would immediately raise suspicion that the mirror has been manipulated. The carpet cloak consists of a tailored refractive-index distribution put on top of this bump (color-coded in Fig. 6.12 (c)). This refractive-index profile compensates for the aberration introduced by the bump and reconstructs the undisturbed outgoing light field. In other words, the mirror looks flat and, hence, unsuspicious again.

The profile contains a region of higher refractive index on top of the bump (green to red colors) and two regions of lower refractive index at the sides of the bump (dark blue).

The carpet cloak concept has been realized experimentally by many different groups [35, 115–120], operating in wavelength ranges from microwave [115, 118] to the visible [119, 120], in microscopic and macroscopic [119, 120] fashions, some only for one polarization of light [119, 120], others also for unpolarized light [35, 115–118]. In this thesis we

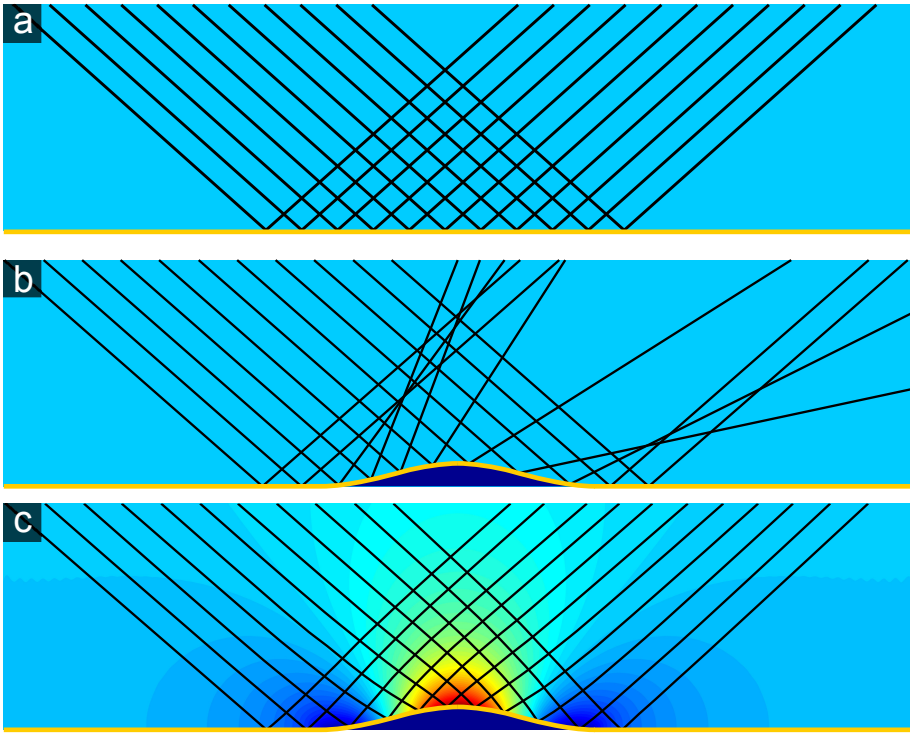

Figure 6.12.: A qualitative illustration of the carpet-cloak principle. (a) A flat mirror (yellow) is covered by a homogeneous dielectric medium (blue) and reflects a parallel bundle of light rays (impinging from the top left) without any distortion. (b) A bump in the mirror offers space to hide an object under this "carpet" (dark blue region). The presence of the bump heavily distorts the outgoing rays and would raise suspicion that the mirror has been manipulated. This situation will later correspond to the "reference structure". (c) The refractive-index distribution of the carpet cloak (color-coded) compensates for the aberration introduced by the bump and reconstructs a parallel bundle of rays leaving the domain. For an outside observer, the mirror appears flat again. See Fig. 6.13 for a quantitative refractive-index distribution. Courtesy of Tolga Ergin [107].

will describe the fabrication of the first and so far only three-dimensional polarization-independent carpet cloak operating at visible frequencies [106].

6.3.2. Tuning the refractive index

The refractive-index distribution necessary to realize the carpet cloak (see Fig. 6.13 (a)) can be mimicked by photonic metamaterials. We use a woodpile photonic crystal in the long-wavelength regime as an effective material. Calculations with the "MIT Photonic-Bands" (MPB) software package [121] show that for such low optical frequencies (below the first stop band), the dispersion relation of a woodpile is quite linear and isotropic [35]. Therefore, a woodpile can be seen as an effective isotropic dielectric material in this wavelength range. Special properties that are commonly associated with photonic crystals (diffraction, Bragg reflection) are absent in this spectral domain.

The effective refractive index n_{eff} of a woodpile (*i.e.*, the inverse slope of the lowest band in the dispersion relation) is between the refractive index of air ($n = 1$) and that of the bulk polymer ($n = 1.52$). The exact value is determined by the polymer volume filling fraction of the structure. In STED-inspired 3D DLW, this volume filling fraction can be easily tuned by adjusting the excitation-laser power P_{exc} while leaving the depletion power at a fixed value. Higher excitation-laser powers lead to larger polymer rods and, for a given rod spacing a, to smaller air gaps in between. Thus, n_{eff} increases as well. This simple reasoning is supported by calculations using the MPB package: Fig. 6.13 (c) shows the anticipated dependence of the effective refractive index n_{eff} on the polymer-rod linewidth d for an aspect ratio of AR = 1.65. However, this theoretical range of linewidths is not accessible in practice [35]: Linewidths below 70 nm are not attainable, even with STED-inspired DLW. Moreover, the wet-chemical development process does not allow for air voids that are completely surrounded by polymer. Therefore, n_{eff} can not be smoothly increased to $n_{\text{eff}} = 1.52$, but will in practice show a discontinuous behavior and likely jump from 1.48 to 1.52 (see Ref. [35]).

The rod spacing of the woodpile photonic crystal determines the operation wavelength range. As the woodpile needs to act as an effective material, its substructure must be smaller than the light wavelength used. For longer and longer wavelengths, the device is supposed to keep working as long as the polymer stays transparent. In 2010, T. Ergin and N. Stenger have already realized a similar carpet cloak [35]. With a lateral rod spacing of $a = 800\,\text{nm}$, this device can operate at wavelengths above 1.5 µm [35]. For a scaled-down version with $a = 350\,\text{nm}$, we expect the lowest operation wavelength to shift from 1.5 µm down to $1.5\,\mu\text{m} \cdot 350\,\text{nm}/800\,\text{nm} = 0.7\,\mu\text{m}$. We can conclude that the effective medium condition is sufficiently satisfied as soon as one leaves the woodpile's fundamental Bragg-reflection band to the long-wavelength side and the transmittance of the material approaches unity (compare typical woodpile spectra in Fig. 6.9 (b) with $a = 350\,\text{nm}$).

Compared to common DLW and for a fixed woodpile rod-spacing a, STED-inspired DLW with a bottle-depletion-beam offers a greater range of excitation powers that lead to open colorful woodpile structures (compare Fig. 6.10 (a, b)). For the anticipated rod spacing of $a = 350\,\text{nm}$, conventional DLW can hardly yield any open woodpile structure while STED-inspired DLW can be used to fabricate high-quality woodpiles with stop bands from the blue all the way to the orange-red spectral region (see Fig. 6.10). For a fixed rod spacing, this color shift directly indicates a change in the effective refractive index n_{eff} of the photonic crystal. This large tunability is paramount for the fabrication of a carpet cloak. The lack of this tuning-freedom renders conventional DLW useless when aiming at $a = 350\,\text{nm}$.

In order to achieve the fine-tuned refractive-index pattern of the carpet cloak, we start by calibrating the resulting effective refractive index by fabricating homogeneous test-woodpiles (*i.e.*, without a variation in filling fraction) with various excitation powers. Each woodpile has roughly the size of the anticipated final cloaking structure and is written using a fixed depletion power of 50 mW. Again, we modulate pulse bursts with 3% duty cycle (see Appendix A.3). Figures 6.13 (e–i) show SEM images of FIB-cut structures. Clearly, for increasing excitation power, the filling fraction increases as well. We measure the linewidths and lineheights in such images and (together with the relation

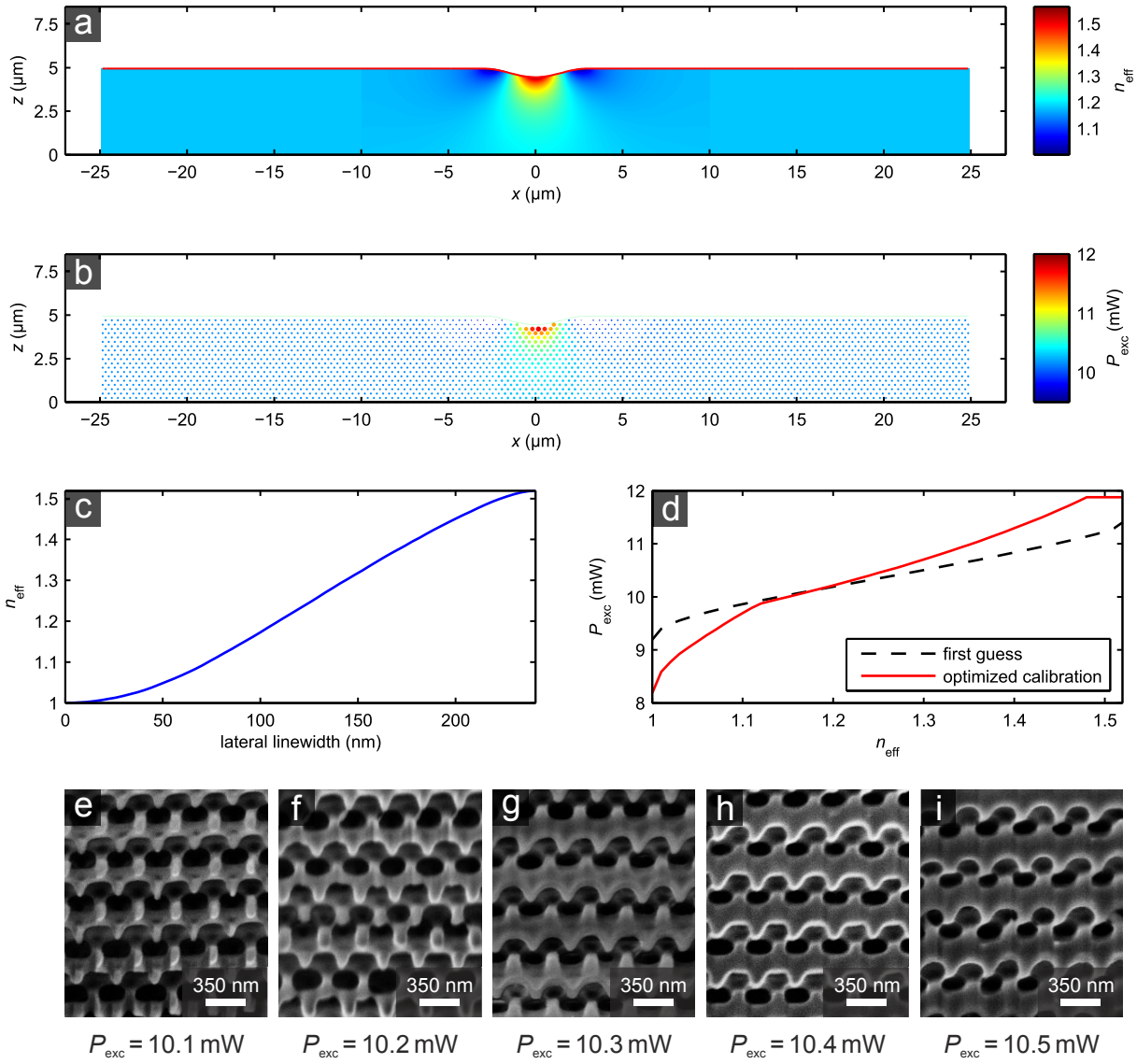

Figure 6.13.: (a) Calculated refractive index distribution of the carpet cloak structure. Note that the structure is from now on put upside-down compared to the previous figure (*i.e.*, the carpet is on the top). The calculated index profile expands over a width of 20 µm and is embedded in a homogeneous medium so that the total length is 50 µm length. The refractive index of this embedding medium is the reference index $n_{\mathrm{ref}} = 1.18$. (b) The refractive-index distribution from (a) is converted to excitation powers for the final woodpile-based structure (color-coded). Only rods parallel to the bump are depicted. The circle size is chosen proportional to the anticipated rod diameter. The carpet is written with 1.05× the excitation power of regions with $n_{\mathrm{eff}} = n_{\mathrm{ref}}$ at a rod spacing of 25 nm. (c) Resulting effective refractive index n_{eff} *vs.* lateral width of the polymer rods for $a = 350$ nm and AR = 1.65 calculated with the MPB package. (d) Required excitation power *vs.* final effective refractive index n_{eff}. A first guess is extracted from the FIB cuts in panels (e–i) (dashed black curve). An empirically optimized function is plotted as red line. (e–i) SEM images of FIB-milled homogeneous woodpiles fabricated with different excitation powers and 50 mW depletion power using a bottle-beam for depletion.

in Fig. 6.13 (c)) deduce a first guess for a function $P_{\mathrm{exc}}(n_{\mathrm{eff}})$ (Fig. 6.13 (d), dashed black line). This function can – in principle – be used to translate an arbitrary refractive-index distribution into a set of local excitation powers for the fabrication.

We assign the excitation powers corresponding to the local filling fractions to each rod of the polymer woodpile (see Fig. 6.13 (b)). Rods crossing the bump region are interrupted to leave this region free. For the polymer rods orthogonal to those depicted in Fig. 6.13 (b), we vary the excitation power continuously along the path of every line. The excitation power is updated every 25 nm, the calculated data are interpolated linearly. This way, we achieve a very smooth variation of n_{eff}.

It turns out, however, that the above function $P_{\mathrm{exc}}(n_{\mathrm{eff}})$ (Fig. 6.13 (d), black dashed line) deduced from homogeneous woodpile samples is not valid in general. The situation within the inhomogeneous carpet cloak differs from the situation in a homogeneous woodpile: Due to the proximity effect, the actual exposure dose and linewidth do not solely depend on the excitation power but also on the exposures performed in the direct vicinity. Therefore, the above function is iteratively optimized by writing carpet cloaks (*i.e.*, woodpiles with the anticipated filling-fraction distribution) and comparing the resulting local filling fractions with the anticipated ones. For the final structure described in the next section, we end up with an optimized function $P_{\mathrm{exc}}(n_{\mathrm{eff}})$ depicted in Fig. 6.13 (d) as red line. The steepness of the function is increased because the proximity effect tends to decrease the exposure contrast between neighboring regions.

To further improve the quality of the final cloaking structures, we apply some experimental tweaks. As described in the previous sections, we slightly scale up the z-coordinates to compensate for anticipated shrinkage. In case of the carpet cloak we have chosen a stretching-factor of $s = 1.26$. We have also previously mentioned that it is common to increase the excitation power when focusing deeper into the photoresist. Again, we use the linear power increase described in Eq. 6.3. To ensure a constant scan velocity (which is necessary to achieve a constant linewidth), we start each line-scan with zero laser power and switch on the laser after 8 µm of straight movement. In this way, the scan stage has already reached its final velocity ($v = 100\,\mu\mathrm{m/s}$) before the laser is switched on. At the end of each line, we switch off the laser but continue moving the stage at constant speed for another 8 µm. The analog signals that control the AOMs are delayed by roughly 10 ms with respect to the signals controlling the scan stage to account for the inertia of the stage. Finally, inhomogeneous shrinkage caused by the intentionally inhomogeneous exposure and the inhomogeneous filling fraction of the cloak will distort the shape of the carpet and the bump. The highly exposed regions below the bump will show very little shrinkage, while the low-index regions will suffer from stronger shrinkage due to the close-to-threshold exposure. For a reference structure with the same geometry but with a homogeneous filling fraction, this is not a problem. To ensure that the shapes of the bumps are very similar in both cases (the cloak and the homogeneous reference), we slightly modify the shape of the carpet in case of the cloak to pre-compensate for inhomogeneous shrinkage.

6.3.3. Final structure and optical performance

The final cloaking structure consists of a woodpile photonic crystal designed to have fcc lattice symmetry. The rod spacing is $a = 350\,\text{nm}$, the footprint is $50\,\mu\text{m} \times 20\,\mu\text{m}$, and the woodpile consists of 40 layers (corresponding to a height of $5\,\mu\text{m}$). The bump has a squared-cosine shape with a design height of $0.5\,\mu\text{m}$ and a full width of $6\,\mu\text{m}$. On top of the structure, we write a thin layer of polymer (marked red in Fig. 6.13 (a)). After exposure, the structures are developed in isopropanol and dried supercritically with CO_2 (Leica EM CPD030). After this step, we sputter gold on top of the structure (sputter chamber Cressington 108 auto) to create the reflective mirror. The polymer film serves as substrate to ensure a flat reflective surface. As the numerical design does not account for this additional dielectric layer, we keep it as thin as possible ($\approx 100\,\text{nm}$). This "polymer-carpet" is written as a layer of densely packed lines oriented parallel to the bump. The line spacing of the overlapping lines is 25 nm (see Fig. 6.13 (b)).

In addition to the cloaking structure, we fabricate a reference structure nearby on the same substrate. This structure has a homogeneous filling fraction (and, hence, a constant refractive index) and serves as reference experiment for the "uncloaked" case. We will compare the visibility of the bump for the cases of the reference and the cloaking structure.

Figure 6.14 (a) contains SEM images of the final structures. The images have been colored to indicate the different materials. The sputtered gold is colored in yellow, the polymer in purple. The upper structure is the reference while the lower one is the cloaking structure. We see that the bumps indeed look very similar.[9]

As we do not want to destroy our best cloaking structures by FIB milling, we use a different, but nominally identical sample for this purpose. Figure 6.14 (d) and (e) show SEM images after FIB milling of a reference structure and a cloaking structure, respectively. For the reference, we see a homogeneous filling fraction as expected. The structure is highly ordered, the filling fraction is independent of the z-position, and the aspect ratio is low (around 1.65) throughout the whole structure. For the cloak structure, we find the anticipated distribution in filling fraction with a high filling fraction below the bump and a low filling fraction at the sides.

The actual performance of the cloak can easily be tested by optical microscopy. We use a self-built microscope based on a single objective lens (ZEISS LD achroplan, 20×, NA = 0.4) that images the sample onto a silicon-based camera. For illumination, we use the OPO described in Section 5.2.2 tuned to 700 nm wavelength. We send the laser through a rotating diffuser to reduce the lateral coherence which would lead to unwanted image artifacts [122, 123]. Illuminations with different linear polarizations lead to results without any visible difference (not depicted). As expected, the device is independent of the polarization state of the illumination. We use circular polarization from now on.

When we inspect the sample from the "wrong" air side (*i.e.*, we look directly from top onto the bumped mirror) we see very similar images for both the reference and the cloaking structure (Fig. 6.14 (b)). This is expected, as the bumps have identical shapes and we look at them from the backside. The flat mirror surface on top of the structures is seen

[9] Additional interferometric measurements show that the bump heights differ by less than 5% [108].

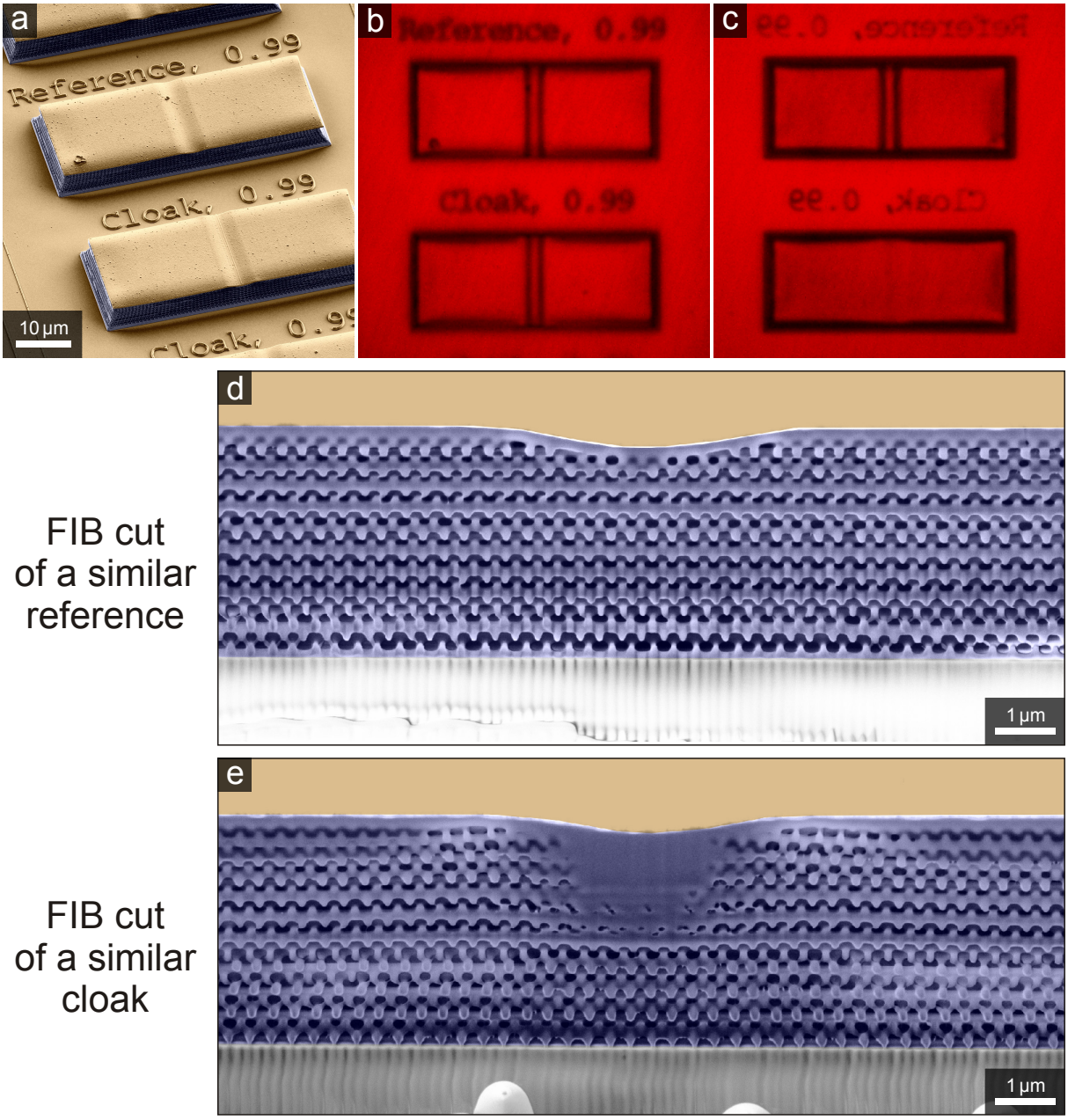

Figure 6.14.: (a) Colored oblique-view electron micrograph of the polymer reference (top) and carpet cloak (bottom) structures (fabricated on a glass substrate and coated with 100 nm gold). To enhance the visibility of the woodpile structure, two images with different brightness have been overlayed ("high dynamic-range image"). (b, c) True-color optical micrographs of the structures in (a) taken with an optical microscope under circularly polarized illumination at 700 nm wavelength. Note the identical distortions due to the bump in both structures in (b) when inspected from the air side (serving as a control experiment). When inspected from the glass-substrate side in (c), the reference structure (top) still shows pronounced dark stripes. In sharp contrast, the stripes essentially disappear for the cloaking structure (bottom). (d, e) Corresponding FIB cuts of nominally identical structures imaged under 54° viewing-angle to the surface-normal. Previously published in Ref. [106].

as a homogeneous bright area that is disturbed by the presence of the bump. Each bump leads to two dark stripes in the image.[10]

If we turn the sample upside down and now inspect it through the artificial index-distributions (*i.e.*, from the "correct" side) the situation changes. In the case of the reference, we still see two pronounced dark stripes as before. The homogeneous woodpile indeed acts as a simple transparent medium. In sharp contrast, for the cloak, the two dark stripes almost completely disappear. Due to the carpet cloak, the mirror looks flat again.

The optical performance of this carpet cloak has been extensively tested. A comprehensive description of the performance is found in Ref. [107]. The device has been shown to work well for a broad range of wavelengths from 650 nm to 900 nm [106]. We expect the cloak to work for even longer wavelengths up to at least 3 µm where polymer absorptions set in. Furthermore, it has been tested under different angles to check the 3D performance [106, 109]. Rotating the sample around the bump axis does not at all affect the cloaking performance [106]. Even rotating the sample around the axis orthogonal to the bump is not very critical [109]. Also, the device does still work if the microscope is intentionally defocused [109]. Finally, the cloak does not only reconstruct the light amplitude but also the light phase [108]. This has been shown using highly sensitive interferometric measuremtns [108].

In conclusion, we have fabricated the first 3D polarization-independent visible-frequency carpet invisibility cloak using our novel approach. The resolution of conventional DLW would not have been sufficient for this task (compare Fig. 6.10). Already today, the increased resolution of STED-inspired DLW allows to create devices that have been thought impossible before.

[10] The exact origin of the dark stripes is explained in Ref. [107].

7. Conclusions and outlook

In this thesis, we have investigated the combination of DLW optical lithography with a depletion-scheme inspired by STED microscopy. While DLW allows for the fabrication of nearly arbitrary three-dimensional shapes, its resolution is fundamentally limited by diffraction. Applying a STED-like mechanism induced by an additional laser brings the perspective to substantially increase the resolution in DLW. No fundamental optics limit remains.

In Chapter 2, after repeating the fundamentals of DLW, we have elaborated on the resolution in lithography. We started with a reminder on Abbe's diffraction barrier:

$$a_{xy} = \frac{\lambda}{2n \sin \alpha} = \frac{\lambda}{2\,\mathrm{NA}}\,.$$

While Abbe's considerations and his formula only apply to parallel exposure schemes, we have used such a scheme as an example to point out the critical difference between "resolution" and "linewidth", two terms that are often misused and intermingled. In lithography, the term "resolution" should be used to describe the minimum attainable distance between two lithographic features. In the case of a parallel exposure, the resolution is fundamentally limited by Abbe's diffraction formula whereas the linewidth is not.

To describe a serial exposure scheme like DLW, we have made the assumption that the exposure doses of sequential exposures simply add up. Regions where the accumulated exposure dose exceeds a threshold dose solidify and remain after development. This rather pessimistic assumption proved to be a good rule of thumb. Within this model, we have generalized the Sparrow criterion and have applied it to sequential 3D exposures *via* two-photon absorption. Using numerically calculated electric-field distributions, we have defined a diffraction limit for common DLW. Interestingly, although DLW is often referred to as a "sub-diffraction-limited" approach, the critical values given by the generalized Sparrow criterion have (to the best of our knowledge) never been surpassed in the literature. Furthermore, we have introduced two handy modifications of the Abbe formula – one for the lateral and one for the equally important axial direction – that nicely resemble the numerical results of the Sparrow criterion for two-photon DLW:

$$a_{xy} = \frac{\lambda}{2\,\mathrm{NA}\,\sqrt{2}}$$

$$a_z = \frac{\lambda\,\mathrm{AR}}{2\,\mathrm{NA}\,\sqrt{2}}\,.$$

Here, AR is the aspect ratio of the diffraction-limited exposure volume.

In Chapter 3, we have explained the depletion idea in detail using STED as an example. In principle, any other depletion mechanism can be used instead. We have derived the anticipated resolution scaling for different depletion foci based upon numerical calculations as well as on asymptotic considerations. Furthermore, the decreased sensitivity to laser-power fluctuations and a possible applicability to low-NA systems have been pointed out.

While many different depletion mechanisms may seem suitable at first, we have shown that the lifetimes of the involved intermediate states impose restrictions on the attainable scan speed and the appropriate type of depletion laser: The shorter the lifetime, the larger the maximum attainable scan speed. However, the requirement on the peak-power of the depletion laser in general increases as well.

At the end of Chapter 3, we have described the different mechanisms leading to a photo-induced polymerization inhibition found in the literature so far, namely STED, RAPID, and the use of a photoinhibitor. The corresponding properties have been discussed and distinct advantages and disadvantages of each approach have been pointed out.

In Chapter 4, we started out by describing the experimental setup that was built and used throughout this thesis. The focus measurement procedure using single gold nanoparticles is essential for the generation of high quality foci, both for the Gaussian excitation focus and for the special depletion foci. Moreover, these measurements have proven to be an important tool to achieve the crucial spatial overlap of the excitation and the depletion focus. The synchronous detection of both lasers described in this thesis renders the method insensitive to thermal drifts of the sample.

In Chapter 5, we have described our (finally successful) search for a photoinitiator that is suitable for STED. As common UV-photoinitiators did not show the anticipated behavior, we have elaborated a list of properties for a suitable STED photoinitiator: a large oscillator strength of the $S_0 \rightarrow S_1$ transition, a rather long S_1 lifetime, and weak excited-state absorption at the depletion wavelength. While the latter is difficult to access, we found the fluorescence quantum-efficiency to be a convenient figure of merit combining the first two properties. Looking for high fluorescence-quantum efficiencies, we have found two photoinitiators that are indeed capable of a photo-induced reversible polymerization suppression, namely isopropyl thioxanthone (ITX) and 7-diethylamino-3-thenoylcoumarin (DETC).

To investigate the nature of this depletion mechanism, we have performed pump-probe experiments in ethanol solution. We found that the transient absorption of ITX is dominated by excited-state absorption and triplet-triplet absorption. Therefore, STED is unlikely to play a key role in the polymerization suppression. In contrast, DETC shows pronounced stimulated emission and weak triplet-triplet absorption.

A second set of experiments aiming at clarifying the depletion mechanism of DETC has been conducted with the photoresist itself. We have tested the depletion capability with a pulsed tunable depletion laser. Upon varying the depletion wavelength as well as the time delay between the excitation and depletion pulses, we have identified two distinct depletion mechanisms in the DETC-based photoresist. The faster one is STED, identified by the intermediate state lifetime ($\tau = 1\,\mathrm{ns}$) and the spectral sensitivity that resembles

the DETC gain-spectrum. The slower depletion effect is yet to be determined. The lifetime of the corresponding intermediate state is between 12.5 ns and 1 µs and could not be resolved in our experiments.

In Chapter 6, we have tested the novel photoresists in lithography experiments. While STED might have favorable properties over the unknown depletion mechanisms in ITX and in DETC, these effects can be used to exceed the diffraction limit. We started out by tackling the lateral direction. Using a donut depletion-focus and cw depletion, we have demonstrated a reduced linewidth of 65 nm in photoresists containing ITX or DETC as photoinitiator. To the best of our knowledge, this is the smallest reported value fabricated using two-photon DLW with near-infrared excitation wavelengths.

As described above, the real challenge is not achieving small feature sizes but achieving small periods or spacings. The generalized Sparrow criterion sets the diffraction limit for the lateral direction to be $a_{xy} = 203\,\text{nm}$. Using our STED-inspired DLW approach, the DETC-based resist, and a donut mode for lateral confinement, we have demonstrated line gratings with $a_{xy} = 200\,\text{nm}$ in excellent quality and with $a_{xy} = 175\,\text{nm}$ in reasonable quality. These values are the smallest found in the literature and below the diffraction limit for the first time. The common-DLW results have suggested that the generalized Sparrow criterion (based on the pessimistic model of a linear accumulation of exposure doses) can only serve as a guideline, but is not a sharp barrier for the resolution of common DLW. However, the fair comparison between common DLW and STED-inspired DLW that we have performed has shown that the latter is superior.

Next, we have addressed the important axial direction in 3D DLW. Using a bottle beam to increase mainly the axial resolution, we have demonstrated a decrease in the aspect ratio of polymerized lines from 2.5 down to 1.6 . Importantly, we have used three-dimensional test structures for these measurements to make sure that the improvement in aspect ratio is directly applicable to every-day 3D DLW tasks.

We have further shown that this improved aspect ratio translates to an improved resolution in the axial direction. The generalized Sparrow criterion states that the diffraction limit is at a critical distance of $a_z = 506\,\text{nm}$. We have successfully fabricated woodpile photonic-crystals with lateral rod distances down to $a = 275\,\text{nm}$. The axial resolution needed for these structures is $a_z = 373\,\text{nm}$. Here, we have demonstrated sub-diffraction-limited axial resolution for the first time. Again, the Sparrow criterion turns out to be a good resolution guideline, yet no sharp barrier for common DLW.

Finally, we have applied the improved resolution of our STED-inspired DLW approach to the fabrication of a 3D carpet invisibility cloak that works at visible wavelengths. This device shows excellent performance, it is polarization independent, broadband, works under a variety of incidence angles, and reconstructs not only the light amplitude but also its phase. We think that this would not have been possible with common DLW or any alternative nanofabrication technology.

Clearly, the data presented in this thesis are only the beginning. Indeed, the diffraction limit has been broken, yet only by a small margin. In the future, resolution on the scale of 10 nm may become possible while maintaining full 3D capabilities.

To proceed towards smaller and smaller features and resolutions, it will be necessary to find improved photoinitiators for STED-inspired DLW. As the slow component seen in DETC is not yet understood, it might be beneficial to concentrate on STED as a depletion mechanism. The photoinitiator properties described in Section 5.1.2 should lead to further photoinitiator candidates. The pump-probe experiments in Section 5.2.1 can be used to identify candidates with low excited-state absorption which is known to be a resolution-limiting factor in STED microscopy.

The pulsed-depletion experiments in Section 5.2.2 and the relative threshold shift introduced as a measure for the depletion capability should allow to compare the performance of different photoinitiators in a quantitative fashion. Different components can be identified and optimal depletion wavelengths, pulse lengths, and repetition rates can be determined.

So far, DETC is the only photoinitiator known to support stimulated emission. We have shown that another depletion mechanism exists in a corresponding photoresist. One could get rid of the unknown depletion component by using a pulsed depletion laser and reducing the repetition rates of both the excitation and the depletion laser from the currently used 80 MHz to significantly smaller values. This would decrease the weight of this slow component and could lead to a further resolution increase.

Moreover, it will likely be necessary to optimize not only the photoinitiator but also the remaining photoresist composition. The minimum linewidth in Section 6.1.2 was found to be 65 nm, independent of the photoinitiator used. Possibly, the polymerization reaction is actually limiting the linewidth and resolution – independent of the size of the effective exposure volume. For example, propagating polymer chains diffusing out of the excitation volume could be responsible. The propagation of a polymer chain can take up to 1 second, which leaves plenty of time for diffusion. This diffusion could be tackled by increasing the photoresist viscosity and, hence, decreasing the mobility of the diffusing molecules. Another possibility is the addition of radical quenchers that terminate propagating chains. This would reduce the time of the chain propagation and therefore the mean distance a propagating chain diffuses within its lifetime.

While the resolution in common DLW has not evolved much within the last decade, STED-inspired DLW opens a new perspective towards quasi unlimited resolution. Common DLW is inherently coupled to the diffraction-limited focal volume and can only slightly shift this border towards smaller scales using chemical tricks. In sharp contrast, there is no optical limitation in STED-inspired DLW any more. With future advances in photoinitiators and photoresists, this novel approach might lead to a revolution in nanoscience and nanotechnology.

At the end, we can say that Richard Feynman's famous sentence "There's plenty of room at the bottom" is still valid.

A. Appendix

A.1. Fluorescence-depletion measurements

Searching for stimulated emission in photoinitiator molecules, we have started out by examining the fluorescence of different photoinitiators in ethanol solution. As described in Section 5.1.3, high fluorescence quantum-efficiencies have guided us to the two photoinitiators that finally worked in the lithography experiments. As high fluorescence quantum-efficiencies are favorable properties for efficient stimulated emission (see Section 5.1.2), one would expect that we can also deplete the fluorescence of the compounds with our depletion laser.

In this section, we report on corresponding fluorescence-depletion experiments with ITX and DETC in ethanol solution. Our setup described in Section 4.1 includes a grating spectrometer with a liquid-nitrogen-cooled CCD camera. We enclose the sample solutions in a "sandwich" consisting of two glass slides with an aluminum spacer. The sandwich edges are sealed with glue such that the ethanol solvent cannot flow out or evaporate.

We focus the Gaussian excitation beam (810 nm center-wavelength) into the volume of the sample solution. The focus position is chosen 5 µm away from the glass-fluid interface to avoid any strong influence of the interface. The excitation laser is switched on with a fixed power and the fluorescence spectrum is recorded. We integrate over the spectrum to get a single number for the fluorescence intensity.

When switching on the co-aligned Gaussian depletion beam (532 nm wavelength, cw), the fluorescence intensity decreases with increasing depletion power. This behavior is depicted in Fig. A.1 for several fixed excitation powers and both photoinitiators. The fluorescence signals of all panels in Fig. A.1 are normalized to the maximum fluorescence with the maximum excitation power. For high excitation powers (red dots), we see a decrease in fluorescence that seems to saturate to a constant value around 0.45 for ITX and 0.35 for DETC. For the intermediate excitation power level (yellow dots), the fluorescence decreases to some extent and then slightly increases again. This behavior is comparable to the increasing linewidths for high depletion powers seen in Fig. 6.2 and Fig. 6.3. Interestingly, with the excitation laser switched off (green dots), we see an increasing fluorescence signal with increasing depletion power. This can be explained by a finite absorption of the depletion laser by ground-state photoinitiator-molecules. The same behavior is observed in lithography experiments with the corresponding photoinitiators: Even with the excitation laser being switched off we observe a polymerization at high depletion powers.

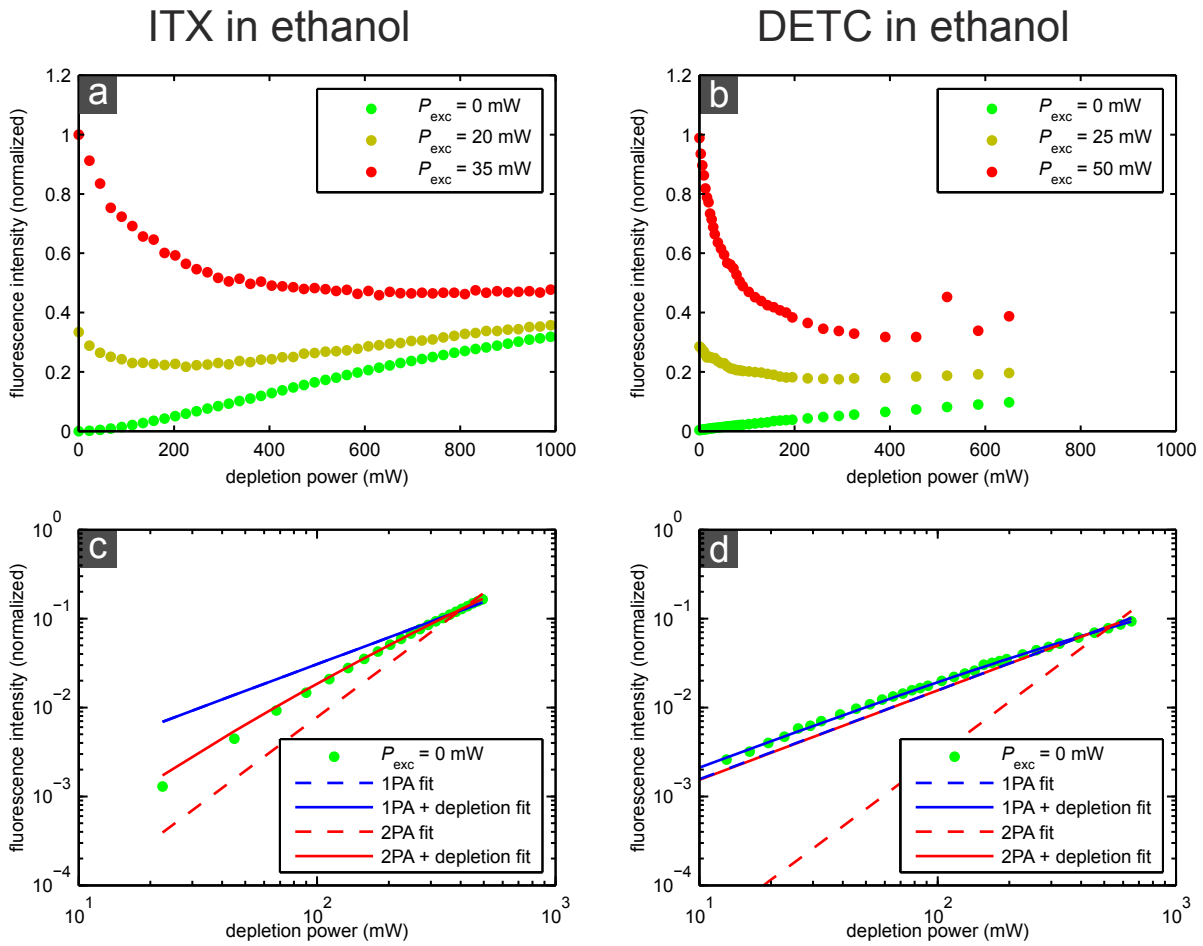

Figure A.1.: (a) Measured fluorescence intensity of ITX in ethanol solution excited *via* two-photon absorption at 810 nm wavelength at different power levels as indicated in the legend. A co-aligned 532 nm cw depletion laser changes the fluorescence level. (b) Same as (a), but for DETC in ethanol solution. (c) Double-logarithmic plot of the unwanted fluorescence of ITX caused by the depletion laser *vs.* depletion-laser-power. (d) Same as (c), but for DETC. Parts of the data have been previously published in Ref. [88].

If we take a closer look at the high and intermediate excitation-power levels again (red and yellow dots), we can see that those do actually not converge to constant value but do asymptotically approach the green signal. Consequently, the excitation caused by the depletion laser does directly limit the depletion capability of the systems.

So far, these findings are perfectly consistent with stimulated emission being the mechanism of fluorescence depletion. Using one-photon excitation, a related publication on ITX and DETC [124] has meanwhile shown that the depletion of fluorescence is only possible within a very short time frame < 100 ns, while stopping the photopolymerization is still possible after a larger time span. Therefore, we do not expect that the same mechanism is responsible for the fluorescence depletion and for the polymerization inhibition. This assumption is consistent with the observation that the depletion power

needed for polymerization inhibition (typically 50 mW) is less than the power needed for substantial fluorescence depletion (around 400 mW). Finally, Ref. [124] has shown an efficient fluorescence depletion of ITX with 642 nm depletion wavelength, comparable to the above data in Fig. A.1. Remember that stimulated emission is only possible within the fluorescence band of a molecule (see Fig. 5.4 for the ITX spectra). Therefore, at 642 nm wavelength, STED is very unlikely to be responsible for the fluorescence depletion in ITX (consistent with the spectra in Fig. 5.4 (a) and the findings of Section 5.2.1). For DETC, however, Ref. [124] finds only very weak fluorescence depletion with 642 nm depletion wavelength. This depletion could be STED indeed (consistent with the spectra in Fig. 5.4 (b) and the findings of Section 5.2.1).

In order to investigate the nature of the unwanted excitation process induced by the depletion laser, we plot the fluorescence signal caused by the depletion laser on a double-logarithmic plot in Fig. A.1 (c) and (d).[1] For a 1PA process, we would expect a linear dependence between fluorescence and incident power. The corresponding graph in the double-log plot should have a slope of one. The blue dashed curves[2] are corresponding linear least-squares fits to the data. In case of a 2PA process, we expect a quadratic dependence, *i.e.*, a slope of two. The red dashed curves correspond to quadratic fits.

For DETC, the 1PA fit works quite well. For ITX, however, neither the 1PA fit nor the 2PA fit yield satisfying agreement. If we take into account that the depletion laser does of course not only excite fluorescence, but also deplete excited states again, we get to more accurate model functions. For this purpose, we take the exact distribution of the electric fields in the focal region derived from numerical calculations (Section 2.2.1) into account.

For a modified 2PA fit, we calculate for each volume element $\mathrm{d}V$ in the focal volume the corresponding contribution to the fluorescence intensity

$$\mathrm{d}I_{\mathrm{fl}} = \sigma_{\mathrm{2PA}} \, |\vec{E}_{\mathrm{depl}}(x,y,z)|^4 \cdot \frac{1}{1 + \sigma_{\mathrm{depletion}} |\vec{E}_{\mathrm{depl}}(x,y,z)|^2} \tag{A.1}$$

where σ_{2PA} is a fit parameter proportional to the 2PA cross-section of the photoinitiator at 532 nm wavelength, σ_{depl} is a fit parameter proportional to the cross-section of the depletion process. $\vec{E}_{\mathrm{depl}}(x,y,z)$ is the calculated electric field of the depletion laser for a Gaussian focus. $|\vec{E}_{\mathrm{depl}}(x,y,z)^2|$ is first normalized to the peak value and must then be scaled with the depletion power. Finally, we sum up all volume elements to obtain the integral fluorescence intensity.

Along these lines, we define a modified 1PA fit function

$$\mathrm{d}I_{\mathrm{fl}} = \sigma_{\mathrm{1PA}} \, |\vec{E}_{\mathrm{depl}}(x,y,z)|^2 \times \frac{1}{1 + \sigma_{\mathrm{depletion}} |\vec{E}_{\mathrm{depl}}(x,y,z)|^2} \tag{A.2}$$

where σ_{1PA} is a fit parameter proportional to the 1PA cross-section of the photoinitiator at 532 nm wavelength.

[1] Here, we exclude depletion powers above 500 mW because additional non-linear behavior seems to set in above this value.

[2] The blue dashed curve in Fig. A.1 (c) is covered by the solid blue curve.

With this additional degree of freedom, we can now fit the ITX data using the model of 2PA with a depletion (red solid line in Fig. A.1 (c)). The inclusion of the depletion effect does not improve the simple 1PA fit. Therefore, this new fit (solid blue line) lies directly on top of the simple 1PA fit (dashed blue line). We conclude that ITX is most likely excited *via* two-photon absorption and the signal is influenced by a "self-depletion".

For DETC, one-photon absorption with a slight "self-depletion" fits the data best (solid blue curve in Fig. A.1 (d)). The simple 1PA fit is also reasonably good (dashed blue line). A pure 2PA excitation can not explain the observed behavior at all (dashed red line). A 2PA model including the depletion can coincide with a simple 1PA and fit the data in reasonable quality. Nevertheless, we conclude that DETC is most likely excited *via* 1PA.

A.2. Model for the pulsed depletion

Within this section, we describe the model used to fit the data shown in Section 5.2.2 and to derive effective cross-sections of the depletion mechanism in Fig. 5.11 (e). Major parts of this text are taken over verbatim from the supporting online material of the previously published Ref. [90].

Fitting the time-resolved data: We model the observed fast decay of the depletion ability on the basis of stimulated emission. First, we assume the S_1 population is generated instantaneously by the fs-pulse and then decays mono-exponentially according to

$$[S_1]_{\Delta t} = \Theta(\Delta t) \cdot [S_1]_0 \cdot \exp(-\Delta t/\tau)\,, \tag{A.3}$$

where $\Theta(\Delta t)$ is the Heaviside step-function, $[S_1]_0$ is the population of the S_1 directly after the excitation pulse, and τ is the excited-state lifetime. The population that has already left S_1 at a certain time Δt after excitation ($[S_1]_0 - [S_1]_{\Delta t}$) will be transferred to the triplet state, generate radicals, and can finally initiate the polymerization reaction at a certain constant yield. A fraction η of the remaining population is sent back to the S_0 *via* stimulated emission induced by the depletion pulse. After the depletion pulse, the remaining undepleted fraction also contributes to the initiation. Hence, the effective exposure dose D_{eff} for a chosen depletion pulse timing is proportional to the sum of the population that has decayed before the depletion pulse arrives ($D_{\text{before}} \propto [S_1]_0 - [S_1]_{\Delta t}$) and the undepleted part of the remaining population ($D_{\text{after}} \propto [S_1]_{\Delta t} \cdot (1-\eta)$):

$$D_{\text{eff}} = D_{\text{before}} + D_{\text{after}} \propto [S_1]_0 - \eta \cdot [S_1]_{\Delta t}\,. \tag{A.4}$$

Because the above proportionality factors are equal, the resulting threshold ratio is given by

$$\frac{P_{\text{th,shifted}}}{P_{\text{th,0}}} = \sqrt{\frac{D_0}{D_{\text{eff}}}} = \sqrt{\frac{[S_1]_0}{[S_1]_0 - \eta \cdot [S_1]_{\Delta t}}} = \sqrt{\frac{1}{1 - \eta \cdot \Theta(\Delta t) \cdot \exp(-\Delta t/\tau)}}\,, \tag{A.5}$$

where D_0 is the unperturbed dose corresponding to zero depletion power. The slow time constant cannot be resolved in our experiment and merely leads to an offset in Fig. 5.9 (d), *i.e.*, to a constant factor. Thus, we multiply the above values (that only account for stimulated emission) by a constant factor c to mimic the threshold-shift caused by the slow effect and by one-photon absorption:

$$\frac{P_{\mathrm{th,shifted}}}{P_{\mathrm{th,0}}} = c \cdot \sqrt{\frac{1}{1 - \eta \cdot \Theta(\Delta t) \cdot \exp(-\Delta t/\tau)}}\,. \tag{A.6}$$

Finally, we convolute the data with a Gaussian pulse with FWHM τ_0 to account for the finite depletion pulse length.

For 532 nm depletion wavelength, we simultaneously fit the resulting formula to the data for several depletion powers below the depletion optimum (0.25 mW, 0.75 mW, 1.66 mW, and 5 mW). The excited-state lifetime τ and pulse length τ_0 are set to be the same for all depletion powers, whereas the depletion efficiency η and the slow-effect threshold-shift c are allowed to be different for each depletion power. The resulting best fit parameters for S_1 lifetime and pulse length are $\tau = 0.99$ ns and $\tau_0 = 0.28$ ns, respectively. The remaining data for other depletion powers (Fig. 5.9 (d)) and for other depletion wavelengths (Fig. 5.11 (a)) are fitted with the same function, but with these predetermined values for τ_0 and τ. Additionally, for each wavelength, we allow a slight shift for the time-delay $\Delta t = 0$ ($\Delta t \to \Delta t - t_0$) to account for measurement inaccuracies of the zero time-delay.

Effective depletion cross-sections: We assume that both depletion effects lead to a reduction of the initial exposure dose D_0 according to $D = D_0/(1 + \sigma\Phi_{\mathrm{depl}})$, where Φ_{depl} is the flux of depletion photons, σ is an effective cross-section associated to the corresponding depletion effect [63]. This observed effective cross-section is proportional to the molecular cross-section and furthermore depending on the temporal overlap between the corresponding intermediate state and the depletion pulse(s). As the depletion focus diameter was held constant in our experiment, $\Phi_{\mathrm{depl}} \propto P_{\mathrm{depl}}/h\nu$ holds, where P_{depl} is the depletion power and $h\nu$ is the depletion-photon energy. From the relative threshold shift $P_{\mathrm{th,\,shifted}}/P_{\mathrm{th,\,0}} - 1$ we obtain the cross-section *via* the condition $P_{\mathrm{th,\,shifted}}/P_{\mathrm{th,\,0}} = \sqrt{D_0/D} = \sqrt{1 + \sigma\Phi_{\mathrm{depl}}}$. The re-arranged formula $\sigma = (\frac{{P_{\mathrm{th,\,shifted}}}^2}{P_{\mathrm{th,\,0}}} - 1)/\Phi_{\mathrm{depl}}$ becomes

$$\sigma \propto (\frac{P^2_{\mathrm{th,\,shifted}}}{P_{\mathrm{th,\,0}}} - 1) \cdot h\nu \tag{A.7}$$

for a fixed depletion power.

A.3. Pulse bursts

We have seen above that not only excitation laser photons but also the depletion laser photons are absorbed by ground-state photoinitiator-molecules. This is a limiting factor in depletion DLW approaches.

In order to reduce the amount of depletion-laser photons absorbed while maintaining the a high depletion efficiency, we introduce a super-pulsing scheme for excitation and depletion. According to Section 3.6.1 the depletion of an intermediate species by any single depletion channel follows $\frac{1}{1+\gamma I_{\mathrm{depl}}}$. The number of excited molecules per volume is not involved.

The number of depletion photons absorbed by the photoinitiator ground state is $\propto I_{\mathrm{depl}} \cdot \Delta t$ for 1PA and $\propto I_{\mathrm{depl}}^2 \cdot \Delta t$ for 2PA. Independent of the absorption-process order, a reduced exposure time Δt will clearly reduce the number of unwanted excitations.

Therefore, we use the AOMs in our setup to modulate square pulses with relatively short duration (7.5 µs), low duty cycle (3%) and high frequency (4 kHz). For the excitation laser, this modulation leads to a burst of roughly 600 fs-pulses. For the depletion laser, we get a simple flat-top pulse.

Let us compare this scheme with the unmodulated case. For the unmodulated case, we assume an average excitation power $P_{\mathrm{exc},\,0}$ and a cw depletion power of $P_{\mathrm{depl},\,0}$. If we now chop the beams with 3% duty cycle, the number of molecules excited by the excitation laser will drop to 3% of the initial value. To compensate for this loss in exposure dose, we have to increase the excitation power to $P_{\mathrm{exc}} = P_{\mathrm{exc},\,0}/\sqrt{0.03} \approx 5.8\, P_{\mathrm{exc},\,0}$.[3]

The depletion efficiency stays the same as before, as it does not depend on the exposure time. Whenever the excitation laser is on, the depletion laser is on as well. Assuming the lifetime of the depleted intermediate state is much shorter than the duration of the pulse bursts, we can say that any excited molecule experiences the same depletion intensity as in the continuous exposure case and will, hence, be depleted with the same probability.

The number of molecules excited by the depletion laser drops to 3% of the initial value as the overall exposure time drops by the same number. In this way, higher depletion powers can be applied.

The frequency of 4 kHz is fast enough to not influence the homogeneity of a written line. At our standard scan velocity of $v = 100\,\mu\mathrm{m/s}$, two adjacent burst-exposures are separated by 25 nm, which is considerably smaller than our current linewidth.

Experimentally, we can verify the expected trends. When changing from continuous exposure to the pulse-burst scheme, the excitation power has to be increased, the depletion capability per mW depletion power stays roughly the same, and the absorption of the depletion laser decreases. Due to the latter, the polymerization-threshold power of the depletion laser rises considerably. For the excitation laser, the threshold does not rise by the predicted factor of 5.8, but by a smaller value in the range of 2–3. Here, the simple model of an accumulating exposure dose described in Section 2.3.2 is lacking some time-dependent characteristics.

Whenever the pulse burst mode is used, the powers mentioned in the text correspond to the powers during the on-phases of the modulators.

[3] Here, we assume that only a small portion of the photoinitiator molecules within the focal volume are excited and we expect no saturation effect.

The use of pulse bursts with a low duty cycle does in many ways correspond to using faster scan speeds. When using faster scan speeds, the local exposure time is reduced, the excitation power has to be increased, the depletion effect per mW depletion power remains the same, and the amount of unwanted absorption of the depletion laser should decrease. Within the model of accumulating exposures, there is no difference at all. Nevertheless, a difference might arise from the temporal dynamics of the polymerization reaction neglected in this model. In practice, fast scan speeds come along with lower accuracy and repeatability due to the increased mechanical load on the scan hardware. Therefore, the above modulation scheme can be more conveniently used without the need for further changes in hardware, software, or writing strategy.

Bibliography

[1] T. Theis, D. Parr, P. Binks, J. Ying, K. E. Drexler, E. Schepers, K. Mullis, C. Bai, J. J. Boland, R. Langer, P. Dobson, C. N. R. Rao, and M. Ferrari, "nan'o·tech·nol'o·gy *n.*" Nature Nanotechnology **1**, 8–10 (2006). http://dx.doi.org/10.1038/nnano.2006.77 (p. 9)

[2] E. Abbe, "The Relation of Aperture and Power in the Microscope (continued)," Journal of the Royal Microscopical Society **2**, 460–473 (1882). http://dx.doi.org/10.1111/j.1365-2818.1882.tb04805.x (p. 10, 26)

[3] J. K. W. Yang and K. K. Berggren, "Using high-contrast salty development of hydrogen silsesquioxane for sub-10-nm half-pitch lithography," Journal of Vacuum Science & Technology B: Microelectronics and Nanometer Structures **25**, 2025–2029 (2007). http://dx.doi.org/10.1116/1.2801881 (p. 10, 13)

[4] H. Duan, D. Winston, J. K. W. Yang, B. M. Cord, V. R. Manfrinato, and K. K. Berggren, "Sub-10-nm half-pitch electron-beam lithography by using poly (methyl methacrylate) as a negative resist," Journal of Vacuum Science & Technology B: Microelectronics and Nanometer Structures **28**, C6C58–C6C62 (2010). http://dx.doi.org/10.1116/1.3501353 (p. 10, 13)

[5] S. W. Hell and J. Wichmann, "Breaking the diffraction resolution limit by stimulated emission: Stimulated-emission-depletion fluorescence microscopy," Optics Letters **19**, 780–782 (1994). http://dx.doi.org/10.1364/OL.19.000780 (p. 11, 33, 48, 67)

[6] E. Rittweger, K. Y. Han, S. E. Irvine, C. Eggeling, and S. W. Hell, "STED microscopy reveals crystal colour centres with nanometric resolution," Nature Photonics **3**, 144–147 (2009). http://dx.doi.org/10.1038/nphoton.2009.2 (p. 11, 33)

[7] H. B. Sun, S. Matsuo, and H. Misawa, "Three-dimensional photonic crystal structures achieved with two-photon-absorption photopolymerization of resin," Applied Physics Letters **74**, 786–788 (1999). http://dx.doi.org/10.1063/1.123367 (p. 13, 14, 97)

[8] S. Kawata, H. B. Sun, T. Tanaka, and K. Takada, "Finer features for functional microdevices," Nature **412**, 697–698 (2001). http://dx.doi.org/10.1038/35089130 (p. 13, 14)

[9] M. Straub and M. Gu, "Near-infrared photonic crystals with higher-order bandgaps generated by two-photon photopolymerization," Optics Letters **27**, 1824–1826 (2002).
http://dx.doi.org/10.1364/OL.27.001824 (p. 13, 97)

[10] M. Deubel, G. von Freymann, M. Wegener, S. Pereira, K. Busch, and C. M. Soukoulis, "Direct laser writing of three-dimensional photonic-crystal templates for telecommunications," Nature Materials **3**, 444–447 (2004).
http://dx.doi.org/doi:10.1038/nmat1155 (p. 13, 14, 97)

[11] C. N. LaFratta, J. T. Fourkas, T. Baldacchini, and R. A. Farrer, "Multiphoton fabrication," Angewandte Chemie International Edition **46**, 6238–6258 (2007).
http://dx.doi.org/10.1002/anie.200603995 (p. 13, 67)

[12] K. S. Lee, R. H. Kim, D. Y. Yang, and S. H. Park, "Advances in 3D nano/microfabrication using two-photon initiated polymerization," Progress in Polymer Science **33**, 631–681 (2008).
http://dx.doi.org/10.1016/j.progpolymsci.2008.01.001 (p. 13)

[13] G. von Freymann, A. Ledermann, M. Thiel, I. Staude, S. Essig, K. Busch, and M. Wegener, "Three-dimensional nanostructures for photonics," Advanced Functional Materials **20**, 1038–1052 (2010).
http://dx.doi.org/10.1002/adfm.200901838 (p. 13)

[14] Y. L. Zhang, Q. D. Chen, H. Xia, and H. B. Sun, "Designable 3D nanofabrication by femtosecond laser direct writing," Nano Today **5**, 435–448 (2010).
http://dx.doi.org/10.1016/j.nantod.2010.08.007 (p. 13)

[15] S. M. Kuebler, M. Rumi, T. Watanabe, K. Braun, B. H. Cumpston, A. A. Heikal, L. L. Erskine, S. Thayumanavan, S. Barlow, S. Marder, and J. Perry, "Optimizing two-photon initiators and exposure conditions for three-dimensional lithographic microfabrication," Journal of Photopolymer Science and Technology **14**, 657–668 (2001).
http://dx.doi.org/10.2494/photopolymer.14.657 (p. 14)

[16] M. Thiel, M. Rill, G. von Freymann, and M. Wegener, "Three-dimensional bi-chiral photonic crystals," Advanced Materials **21**, 4680–4682 (2009).
http://dx.doi.org/10.1002/adma.200901601 (p. 14)

[17] J. K. Gansel, M. Thiel, M. S. Rill, M. Decker, K. Bade, V. Saile, G. von Freymann, S. Linden, and M. Wegener, "Gold helix photonic metamaterial as broadband circular polarizer," Science **325**, 1513–1515 (2009).
http://dx.doi.org/10.1126/science.1177031 (p. 14)

[18] "Nanoscribe GmbH," .
http://www.nanoscribe.de (p. 14, 101)

[19] F. Klein, T. Striebel, J. Fischer, Z. Jiang, C. M. Franz, G. von Freymann, M. Wegener, and M. Bastmeyer, "Elastic fully three-dimensional microstructure scaffolds for cell force measurements," Advanced Materials **22**, 868–871 (2010). http://dx.doi.org/10.1002/adma.200902515 (p. 14, 15, 42)

[20] A. Tandaechanurat, S. Ishida, D. Guimard, M. Nomura, S. Iwamoto, and Y. Arakawa, "Lasing oscillation in a three-dimensional photonic crystal nanocavity with a complete bandgap," Nature Photonics **5**, 91–94 (2010). http://dx.doi.org/10.1038/nphoton.2010.286 (p. 13)

[21] G. Subramania, Y. Lee, A. Fischer, and D. Koleske, "Log-Pile TiO2 Photonic Crystal for Light Control at Near-UV and Visible Wavelengths," Advanced Materials **22**, 487–491 (2010). http://dx.doi.org/10.1002/adma.200902264 (p. 13)

[22] S. Wong, M. Deubel, F. Pérez-Willard, S. John, G. A. Ozin, M. Wegener, and G. von Freymann, "Direct laser writing of three-dimensional photonic crystals with a complete photonic bandgap in chalcogenide glasses," Advanced Materials **18**, 265–269 (2006). http://dx.doi.org/10.1002/adma.200501973 (p. 14)

[23] S. H. Wong, M. Thiel, P. Brodersen, D. Fenske, G. A. Ozin, M. Wegener, and G. von Freymann, "Highly selective wet etch for high-resolution three-dimensional nanostructures in arsenic sulfide all-inorganic photoresist," Chemistry of Materials **19**, 4213–4221 (2007). http://dx.doi.org/10.1021/cm070756y (p. 14)

[24] M. S. Rill, C. Plet, M. Thiel, I. Staude, G. von Freymann, S. Linden, and M. Wegener, "Photonic metamaterials by direct laser writing and silver chemical vapour deposition," Nature Materials **7**, 543–546 (2008). http://dx.doi.org/10.1038/nmat2197 (p. 14)

[25] A. Radke, T. Gissibl, T. Klotzbücher, P. V. Braun, and H. Giessen, "Three-dimensional bichiral plasmonic crystals fabricated by direct laser writing and electroless silver plating," Advanced Materials **23**, 3018–3021 (2011). http://dx.doi.org/10.1002/adma.201100543 (p. 14)

[26] N. Tétreault, G. von Freymann, M. Deubel, M. Hermatschweiler, F. Pérez-Willard, S. John, M. Wegener, and G. A. Ozin, "New route to three-dimensional photonic bandgap materials: Silicon double inversion of polymer templates," Advanced Materials **18**, 457–460 (2006). http://dx.doi.org/10.1002/adma.200501674 (p. 14)

[27] A. Ledermann, L. Cademartiri, M. Hermatschweiler, C. Toninelli, G. A. Ozin, D. S. Wiersma, M. Wegener, and G. von Freymann, "Three-dimensional silicon inverse photonic quasicrystals for infrared wavelengths," Nature Materials **5**, 942–945 (2006). http://dx.doi.org/10.1038/nmat1786 (p. 14)

[28] M. Hermatschweiler, A. Ledermann, G. A. Ozin, M. Wegener, and G. von Freymann, "Fabrication of silicon inverse woodpile photonic crystals," Advanced Functional Materials **17**, 2273–2277 (2007).
http://dx.doi.org/10.1002/adfm.200601074 (p. 14)

[29] A. Frölich and M. Wegener, "Spectroscopic characterization of highly doped ZnO films grown by atomic-layer deposition for three-dimensional infrared metamaterials," Optical Materials Express **1**, 883–889 (2011).
http://dx.doi.org/10.1364/OME.1.000883 (p. 14)

[30] I. Staude, M. Thiel, S. Essig, C. Wolff, K. Busch, G. von Freymann, and M. Wegener, "Fabrication and characterization of silicon woodpile photonic crystals with a complete bandgap at telecom wavelengths," Optics Letters **35**, 1094–1096 (2010).
http://dx.doi.org/10.1364/OL.35.001094 (p. 14, 97, 102, 106)

[31] M. Thiel, M. Decker, M. Deubel, M. Wegener, S. Linden, and G. von Freymann, "Polarization stop bands in chiral polymeric three-dimensional photonic crystals," Advanced Materials **19**, 207–210 (2007).
http://dx.doi.org/10.1002/adma.200601497 (p. 14)

[32] M. Thiel, J. Gansel, M. Wegener, and G. von Freymann, "Wenn das Licht den Dreh raus hat. Künstliche chirale Materialien," Physik in unserer Zeit **42**, 70–76 (2011).
http://dx.doi.org/10.1002/piuz.201101253 (p. 14)

[33] A. Ledermann, M. Wegener, and G. von Freymann, "Rhombicuboctahedral three-dimensional photonic quasicrystals," Advanced Materials **22**, 2363–2366 (2010).
http://dx.doi.org/10.1002/adma.200903885 (p. 14)

[34] C. Soukoulis and M. Wegener, "Past achievements and future challenges in the development of three-dimensional photonic metamaterials," Nature Photonics **5**, 523–530 (2011).
http://dx.doi.org/10.1038/nphoton.2011.154 (p. 14)

[35] T. Ergin, N. Stenger, P. Brenner, J. B. Pendry, and M. Wegener, "Three-dimensional invisibility cloak at optical wavelengths," Science **328**, 337–339 (2010).
http://dx.doi.org/10.1126/science.1186351 (p. 14, 107, 108, 109)

[36] T. Grossmann, S. Schleede, M. Hauser, T. Beck, M. Thiel, G. von Freymann, T. Mappes, and H. Kalt, "Direct laser writing for active and passive high-Q polymer microdisks on silicon," Optics Express **19**, 11 451–11 456 (2011).
http://dx.doi.org/10.1364/OE.19.011451 (p. 14)

[37] S. Wong, O. Kiowski, M. Kappes, J. K. N. Lindner, N. Mandal, F. C. Peiris, G. A. Ozin, M. Thiel, M. Braun, M. Wegener, and G. von Freymann, "Spatially localized photoluminescence at 1.5 micrometers wavelength in direct laser written optical nanostructures," Advanced Materials **20**, 4097–4102 (2008).
http://dx.doi.org/10.1002/adma.200801508 (p. 14)

[38] N. Lindenmann, I. Kaiser, G. Balthasar, R. Bonk, D. Hillerkuss, W. Freude, J. Leuthold, and C. Koos, "Photonic waveguide Bonds – a novel concept for chip-to-chip Interconnects," in *Optical Fiber Communication Conference* p. PDPC1 (2011). http://www.opticsinfobase.org/abstract.cfm?URI=OFC-2011-PDPC1 (p. 14)

[39] N. Lindenmann, G. Balthasar, R. Palmer, S. Schuele, J. Leuthold, W. Freude, and C. Koos, "Photonic wire bonding for single-mode chip-to-chip interconnects," in *Group IV Photonics (GFP), 2011 8th IEEE International Conference on* pp. 380–382 (2011).
http://dx.doi.org/10.1109/GROUP4.2011.6053823 (p. 14)

[40] T. Bückmann, N. Stenger, M. Kadic, J. Kaschke, A. Frölich, T. Kennerknecht, C. Eberl, M. Thiel, and M. Wegener, "Tailored 3D mechanical metamaterials made by dip-in direct-laser-writing optical lithography," Advanced Materials **24**, 2710–2714 (2012).
http://dx.doi.org/10.1002/adma.201200584 (p. 14, 101)

[41] M. Kadic, T. Bückmann, N. Stenger, M. Thiel, and M. Wegener, "On the feasibility of pentamode mechanical metamaterials," Applied Physics Letters **100**, 191 901 (2012).
http://dx.doi.org/10.1063/1.4709436 (p. 14)

[42] I. Staude, C. McGuinness, A. Frölich, R. L. Byer, E. Colby, and M. Wegener, "Waveguides in three-dimensional photonic bandgap materials for particle-accelerator on a chip architectures," Optics Express **20**, 5607–5612 (2012).
http://dx.doi.org/10.1364/OE.20.005607 (p. 15)

[43] F. Klein, B. Richter, T. Striebel, C. M. Franz, G. Freymann, M. Wegener, and M. Bastmeyer, "Two-component polymer scaffolds for controlled three-dimensional cell culture," Advanced Materials **23**, 1341–1345 (2011).
http://dx.doi.org/10.1002/adma.201004060 (p. 15, 42)

[44] F. Claeyssens, E. A. Hasan, A. Gaidukeviciute, D. S. Achilleos, A. Ranella, C. Reinhardt, A. Ovsianikov, X. Shizhou, C. Fotakis, M. Vamvakaki, B. N. Chichkov, and M. Farsari, "Three-dimensional biodegradable structures fabricated by two-photon polymerization," Langmuir **25**, 3219–3223 (2009).
http://dx.doi.org/10.1021/la803803m (p. 15)

[45] M. Röhrig, M. Thiel, M. Worgull, and H. Hölscher, "3D direct laser writing of nano- and microstructured hierarchical gecko-mimicking surfaces," Small (submitted). (p. 15)

[46] S. Maruo and K. Ikuta, "Three-dimensional microfabrication by use of single-photon-absorbed polymerization," Applied Physics Letters **76**, 2656–2658 (2000).
http://dx.doi.org/10.1063/1.126742 (p. 19)

[47] A. Van De Nes, L. Billy, S. Pereira, and J. Braat, "Calculation of the vectorial field distribution in a stratified focal region of a high numerical aperture imaging system," Optics Express **12**, 1281–1293 (2004).
http://dx.doi.org/10.1364/OPEX.12.001281 (p. 20, 21, 22, 23)

[48] E. Wolf, "Electromagnetic diffraction in optical systems. I. An integral representation of the image field," Proceedings of the Royal Society of London. Series A. Mathematical and Physical Sciences **253**, 349–357 (1959).
http://dx.doi.org/10.1098/rspa.1959.0199 (p. 20)

[49] B. Richards and E. Wolf, "Electromagnetic diffraction in optical systems. II. Structure of the image field in an aplanatic system," Proceedings of the Royal Society of London. Series A. Mathematical and Physical Sciences **253**, 358–379 (1959).
http://dx.doi.org/10.1098/rspa.1959.0200 (p. 20, 22)

[50] S. Quabis, R. Dorn, M. Eberler, O. Glöckl, and G. Leuchs, "Focusing light to a tighter spot," Optics Communications **179**, 1–7 (2000).
http://dx.doi.org/10.1016/S0030-4018(99)00729-4 (p. 23)

[51] R. Dorn, S. Quabis, and G. Leuchs, "Sharper focus for a radially polarized light beam," Physical Review Letters **91**, 233 901 (2003).
http://dx.doi.org/10.1103/PhysRevLett.91.233901 (p. 23, 24)

[52] T. Grosjean and D. Courjon, "Smallest focal spots," Optics Communications **272**, 314–319 (2007).
http://dx.doi.org/10.1016/j.optcom.2006.11.043 (p. 23)

[53] B. Jia, H. Kang, J. Li, and M. Gu, "Use of radially polarized beams in three-dimensional photonic crystal fabrication with the two-photon polymerization method," Optics Letters **34**, 1918–1920 (2009).
http://dx.doi.org/10.1364/OL.34.001918 (p. 23)

[54] "Oxford Dictionary Online," .
http://www.oxforddictionaries.com (p. 26)

[55] J. Fischer and M. Wegener, "Three-dimensional optical laser lithography beyond the diffraction limit," Laser & Photonics Reviews (2012).
http://dx.doi.org/10.1002/lpor.201100046
(p. 26, 27, 30, 31, 33, 38, 41, 47, 49, 94, 97, 106)

[56] E. Abbe, "Beiträge zur Theorie des Mikroskops und der mikroskopischen Wahrnehmung," Archiv für mikroskopische Anatomie **9**, 413–468 (1873).
http://dx.doi.org/10.1007/BF02956173
http://dx.doi.org/10.1007/BF02956174
http://dx.doi.org/10.1007/BF02956175
http://dx.doi.org/10.1007/BF02956176 (p. 26)

[57] M. Campbell, D. N. Sharp, M. T. Harrison, R. G. Denning, and A. J. Turberfield, "Fabrication of photonic crystals for the visible spectrum by holographic lithography," Nature **404**, 53–56 (2000).
http://dx.doi.org/doi:10.1038/35003523 (p. 28)

[58] D. C. Meisel, M. Wegener, and K. Busch, "Three-dimensional photonic crystals by holographic lithography using the umbrella configuration: Symmetries and complete photonic band gaps," Physical Review B **70**, 165 104 (2004).
http://dx.doi.org/10.1103/PhysRevB.70.165104 (p. 28)

[59] C. M. Sparrow, "On spectroscopic resolving power," The Astrophysical Journal **44**, 76–86 (1916).
http://dx.doi.org/10.1086%2F142271 (p. 30)

[60] T. A. Klar, S. Jakobs, M. Dyba, A. Egner, and S. W. Hell, "Fluorescence microscopy with diffraction resolution barrier broken by stimulated emission," Proceedings of the National Academy of Sciences **97**, 8206–8210 (2000).
http://dx.doi.org/10.1073/pnas.97.15.8206 (p. 33, 35, 45, 46, 48)

[61] V. Westphal and S. W. Hell, "Nanoscale resolution in the focal plane of an optical microscope," Physical Review Letters **94**, 143 903 (2005).
http://dx.doi.org/10.1103/PhysRevLett.94.143903 (p. 33, 48, 51, 67)

[62] K. I. Willig, S. O. Rizzoli, V. Westphal, R. Jahn, and S. W. Hell, "STED microscopy reveals that synaptotagmin remains clustered after synaptic vesicle exocytosis," Nature **440**, 935–939 (2006).
http://dx.doi.org/10.1038/nature04592 (p. 33)

[63] S. W. Hell, "Far-field optical nanoscopy," Science **316**, 1153–1158 (2007).
http://dx.doi.org/10.1126/science.1137395 (p. 33, 123)

[64] S. W. Hell, "Microscopy and its focal switch," Nature Methods **6**, 24–32 (2008).
http://dx.doi.org/10.1038/nmeth.1291 (p. 33)

[65] S. W. Hell, R. Schmidt, and A. Egner, "Diffraction-unlimited three-dimensional optical nanoscopy with opposing lenses," Nature Photonics **3**, 381–387 (2009).
http://dx.doi.org/10.1038/nphoton.2009.112 (p. 33)

[66] L. Li, R. R. Gattass, E. Gershgoren, H. Hwang, and J. T. Fourkas, "Achieving $\lambda/20$ resolution by one-color initiation and deactivation of polymerization," Science **324**, 910–913 (2009).
http://dx.doi.org/10.1126/science.1168996 (p. 36, 46, 49, 50, 51, 68, 96)

[67] T. F. Scott, B. A. Kowalski, A. C. Sullivan, C. N. Bowman, and R. R. McLeod, "Two-color single-photon photoinitiation and photoinhibition for subdiffraction photolithography," Science **324**, 913–917 (2009).
http://dx.doi.org/10.1126/science.1167610 (p. 36, 46, 49, 51)

[68] J. Keller, A. Schönle, and S. W. Hell, "Efficient fluorescence inhibition patterns for RESOLFT microscopy," Optics Express **15**, 3361–3371 (2007).
http://dx.doi.org/10.1364/OE.15.003361 (p. 37)

[69] D. Wildanger, R. Medda, L. Kastrup, and S. W. Hell, "A compact STED microscope providing 3D nanoscale resolution," Journal of Microscopy **236**, 35–43 (2009).
http://dx.doi.org/10.1111/j.1365-2818.2009.03188.x (p. 38)

[70] A. Pikulin and N. Bityurin, "Spatial confinement of percolation: Monte Carlo modeling and nanoscale laser polymerization," Physical Review B **82**, 085 406 (2010).
http://dx.doi.org/10.1103/PhysRevB.82.085406 (p. 41)

[71] S. A. Pruzinsky and P. V. Braun, "Fabrication and characterization of two-photon polymerized features in colloidal crystals," Advanced Functional Materials **15**, 1995–2004 (2005).
http://dx.doi.org/10.1002/adfm.200500345 (p. 44)

[72] M. P. Stocker, L. Li, R. R. Gattass, and J. T. Fourkas, "Multiphoton photoresists giving nanoscale resolution that is inversely dependent on exposure time," Nature Chemistry **3**, 225–229 (2011).
http://dx.doi.org/10.1038/nchem.965 (p. 49, 50, 51)

[73] R. R. McLeod, B. A. Kowalski, and M. C. Cole, "Two-color photoinitiation/inhibition lithography," in *Proceedings of SPIE* **7591**, 759 102 (2010).
http://dx.doi.org/10.1117/12.845850 (p. 51)

[74] V. F. Plyusnin, E. P. Kuznetzova, G. A. Bogdanchikov, V. P. Grivin, V. N. Kirichenko, and S. V. Larionov, "Dithiocarbamate radicals in laser flash photolysis of thiuram disulphide and dithiocarbamate anion: Calculation of optical spectra," Journal of Photochemistry and Photobiology A: Chemistry **68**, 299–308 (1992).
http://dx.doi.org/10.1016/1010-6030(92)85239-Q (p. 52)

[75] B. A. Kowalski, T. F. Scott, C. N. Bowman, A. C. Sullivan, and R. R. McLeod, "Exceeding the diffraction limit with single-photon photopolymerization and photoinduced termination," in *Proceedings of SPIE* **7053**, 70 530E (2008).
http://dx.doi.org/10.1117/12.796978 (p. 52)

[76] E. Rittweger, B. R. Rankin, V. Westphal, and S. W. Hell, "Fluorescence depletion mechanisms in super-resolving STED microscopy," Chemical Physics Letters **442**, 483–487 (2007).
http://dx.doi.org/10.1016/j.cplett.2007.06.017 (p. 53, 84)

[77] L. De Boni, E. Piovesan, L. Misoguti, S. C. Zilio, and C. Mendonca, "Two-photon absorption dependence on the temperature for azoaromatic compounds: Effect of molecular conformation," The Journal of Physical Chemistry A **111**, 6222–6224 (2007).
http://dx.doi.org/10.1021/jp0716684 (p. 53)

[78] Y. J. Liu, X. W. Sun, H. T. Dai, J. H. Liu, and K. S. Xu, "Effect of surfactant on the electro-optical properties of holographic polymer dispersed liquid crystal Bragg gratings," Optical Materials **27**, 1451–1455 (2005).
http://dx.doi.org/10.1016/j.optmat.2004.10.010 (p. 58, 100)

[79] M. Thiel, J. Fischer, G. von Freymann, and M. Wegener, "Direct laser writing of three-dimensional submicron structures using a continuous-wave laser at 532 nm," Applied Physics Letters **97**, 221 102 (2010).
http://dx.doi.org/10.1063/1.3521464 (p. 65, 92, 97, 102)

[80] F. Morlet-Savary, X. Allonas, C. Dietlin, J. P. Malval, and J. P. Fouassier, "Photochemistry and photophysics of a morpholino methylthio phenyl ketone: A steady-state, picosecond pump-probe laser spectroscopy and molecular modeling investigation," Journal of Photochemistry and Photobiology A: Chemistry **197**, 342–350 (2008).
http://dx.doi.org/10.1016/j.jphotochem.2008.01.013 (p. 67)

[81] "ATTO-TEC GmbH," .
http://www.atto-tec.com (p. 67, 72)

[82] C. S. Colley, C. David, N. A. Besley, S. Jockusch, P. Matousek, A. W. Parker, M. Towrie, N. J. Turro, P. M. W. Gill, and M. W. George, "Probing the reactivity of photoinitiators for free radical polymerization: Time-resolved infrared spectroscopic study of benzoyl radicals," Journal of the American Chemical Society **124**, 14 952–14 958 (2002).
http://dx.doi.org/10.1021/ja026099m (p. 67)

[83] M. Kasha, "Characterization of electronic transitions in complex molecules," Discussions of the Faraday Society **9**, 14–19 (1950).
http://dx.doi.org/10.1039/DF9500900014 (p. 68)

[84] J. V. Morris, M. A. Mahaney, and J. R. Huber, "Fluorescence quantum yield determinations. 9,10-Diphenylanthracene as a reference standard in different solvents," The Journal of Physical Chemistry **80**, 969–974 (1976).
http://dx.doi.org/10.1021/j100550a010 (p. 69)

[85] M. Mardelli and J. Olmsted, "Calorimetric determination of the 9, 10-diphenylanthracene fluorescence quantum yield," Journal of Photochemistry **7**, 277–285 (1977).
http://dx.doi.org/10.1016/0047-2670(77)85005-3 (p. 69)

[86] S. Dhami, A. J. D. Mello, G. Rumbles, S. M. Bishop, D. Phillips, and A. Beeby, "Phthalocyanine fluorescence at high concentration: dimers or reabsorption effect?" Photochemistry and Photobiology **61**, 341–346 (1995).
http://dx.doi.org/10.1111/j.1751-1097.1995.tb08619.x (p. 70)

[87] D. P. Specht, P. A. Martic, and S. Farid, "Ketocoumarins: A new class of triplet sensitizers," Tetrahedron **38**, 1203–1211 (1982).
http://dx.doi.org/10.1016/0040-4020(82)85104-1 (p. 71)

[88] J. Fischer, G. von Freymann, and M. Wegener, "The materials challenge in diffraction-unlimited direct-laser-writing optical lithography," Advanced Materials **22**, 3578–3582 (2010).
http://dx.doi.org/10.1002/adma.201000892 (p. 71, 73, 87, 89, 90, 120)

[89] T. J. A. Wolf, J. Fischer, M. Wegener, and A. N. Unterreiner, "Pump-probe spectroscopy on photoinitiators for stimulated-emission-depletion optical lithography," Optics Letters **36**, 3188–3190 (2011).
http://dx.doi.org/10.1364/OL.36.003188 (p. 72, 75, 76, 77, 82)

[90] J. Fischer and M. Wegener, "Ultrafast polymerization inhibition by stimulated emission depletion for three-dimensional nano lithography," Advanced Materials **24**, OP65–OP69 (2012).
http://dx.doi.org/10.1002/adma.201103758 (p. 75, 78, 79, 80, 83, 122)

[91] J. Fischer and M. Wegener, "Three-dimensional direct laser writing inspired by stimulated-emission-depletion microscopy," Optical Materials Express **1**, 614–624 (2011).
http://dx.doi.org/10.1364/OME.1.000614 (p. 87, 92, 93, 94, 99, 101, 103)

[92] S. Juodkazis, V. Mizeikis, K. K. Seet, M. Miwa, and H. Misawa, "Two-photon lithography of nanorods in SU-8 photoresist," Nanotechnology **16**, 846–849 (2005).
http://dx.doi.org/10.1088/0957-4484/16/6/039 (p. 89)

[93] D. Tan, Y. Li, F. Qi, H. Yang, Q. Gong, X. Dong, and X. Duan, "Reduction in feature size of two-photon polymerization using SCR500," Applied Physics Letters **90**, 071 106 (2007).
http://dx.doi.org/10.1063/1.2535504 (p. 89)

[94] J. Fischer, T. Ergin, and M. Wegener, "Towards diffraction-unlimited three-dimensional laser lithography," in *Proceedings of High Power Laser Ablation* (2012), accepted. (p. 91)

[95] S. H. Park, T. W. Lim, D. Y. Yang, R. H. Kim, and K. S. Lee, "Improvement of spatial resolution in nano-stereolithography using radical quencher," Macromolecular Research **14**, 559–564 (2006).
http://dx.doi.org/10.1007/BF03218724 (p. 91, 92)

[96] J. F. Xing, X. Z. Dong, W. Q. Chen, X. M. Duan, N. Takeyasu, T. Tanaka, and S. Kawata, "Improving spatial resolution of two-photon microfabrication by using photoinitiator with high initiating efficiency," Applied Physics Letters **90**, 131 106 (2007).
http://dx.doi.org/10.1063/1.2717532 (p. 91)

[97] H. Sun, K. Takada, M. Kim, K. Lee, and S. Kawata, "Scaling laws of voxels in two-photon photopolymerization nanofabrication," Applied Physics Letters **83**, 1104 (2003).
http://dx.doi.org/10.1063/1.1599968 (p. 96)

[98] H. B. Sun, T. Tanaka, and S. Kawata, "Three-dimensional focal spots related to two-photon excitation," Applied Physics Letters **80**, 3673–3675 (2002).
http://dx.doi.org/10.1063/1.1478128 (p. 96)

[99] M. M. Sigalas, C. M. Soukoulis, C. T. Chan, and K. M. Ho, "Electromagnetic-wave propagation through dispersive and absorptive photonic-band-gap materials," Physical Review B **49**, 11 080–11 087 (1994).
http://dx.doi.org/10.1103/PhysRevB.49.11080 (p. 97)

[100] K. M. Ho, C. T. Chan, C. M. Soukoulis, R. Biswas, and M. Sigalas, "Photonic band gaps in three dimensions: new layer-by-layer periodic structures," Solid State Communications **89**, 413–416 (1994).
http://dx.doi.org/10.1016/0038-1098(94)90202-X (p. 97)

[101] M. Deubel, M. Wegener, S. Linden, and G. von Freymann, "Angle-resolved transmission spectroscopy of three-dimensional photonic crystals fabricated by direct laser writing," Applied Physics Letters **87**, 221 104 (2005).
http://dx.doi.org/10.1063/1.2137899 (p. 97)

[102] W. Haske, V. Chen, J. M. Hales, W. Dong, S. Barlow, S. R. Marder, and J. W. Perry, "65 nm feature sizes using visible wavelength 3-D multiphoton lithography," Optics Express **15**, 3426–3436 (2007).
http://dx.doi.org/10.1364/OE.15.003426 (p. 97, 102)

[103] A. Jesacher, G. Marshall, T. Wilson, and M. Booth, "Adaptive optics for direct laser writing with plasma emission aberration sensing," Optics Express **18**, 656–661 (2010).
http://dx.doi.org/10.1364/OE.18.000656 (p. 101)

[104] I. Sakellari, E. Kabouraki, D. Gray, V. Purlys, C. Fotakis, A. Pikulin, N. Bityurin, M. Vamvakaki, and M. Farsari, "Diffusion-assisted high resolution direct femtosecond laser writing," ACS Nano .
http://dx.doi.org/10.1021/nn204454c (p. 102)

[105] E. Yablonovitch, "Inhibited spontaneous emission in solid-state physics and electronics," Physical Review Letters **58**, 2059–2062 (1987).
http://dx.doi.org/10.1103/PhysRevLett.58.2059 (p. 106)

[106] J. Fischer, T. Ergin, and M. Wegener, "Three-dimensional polarization-independent visible-frequency carpet invisibility cloak," Optics Letters **36**, 2059–2061 (2011).
http://dx.doi.org/10.1364/OL.36.002059 (p. 106, 108, 113, 114)

[107] T. Ergin, *Photonic Metamaterials for Transformation Optics*, Ph.D. thesis, Karlsruhe Institute of Technology (KIT) (2012).
http://digbib.ubka.uni-karlsruhe.de/volltexte/1000026037 (p. 106, 108, 114)

[108] T. Ergin, J. Fischer, and M. Wegener, "Optical phase cloaking of 700 nm light waves in the far field by a three-dimensional carpet cloak," Physical Review Letters **107**, 173 901 (2011).
http://dx.doi.org/10.1103/PhysRevLett.107.173901 (p. 106, 112, 114)

[109] T. Ergin, J. Fischer, and M. Wegener, "Detailed optical characterization of three-dimensional visible-frequency polarization-independent carpet invisibility cloak," Physica B: Condensed Matter (2011).
http://dx.doi.org/10.1016/j.physb.2011.11.035 (p. 106, 114)

[110] U. Leonhardt, "Optical conformal mapping," Science **312**, 1777 (2006).
http://dx.doi.org/10.1126/science.1126493 (p. 107)

[111] J. B. Pendry, D. Schurig, and D. R. Smith, "Controlling electromagnetic fields," Science **312**, 1780–1782 (2006).
http://dx.doi.org/10.1126/science.1125907 (p. 107)

[112] V. M. Shalaev, "Transforming light," Science **322**, 384–386 (2008).
http://dx.doi.org/10.1126/science.1166079 (p. 107)

[113] H. Chen, C. T. Chan, and P. Sheng, "Transformation optics and metamaterials," Nature Materials **9**, 387–396 (2010).
http://dx.doi.org/10.1038/nmat2743 (p. 107)

[114] J. Li and J. B. Pendry, "Hiding under the carpet: A new strategy for cloaking," Physical Review Letters **101**, 203 901 (2008).
http://dx.doi.org/10.1103/PhysRevLett.101.203901 (p. 107)

[115] R. Liu, C. Ji, J. J. Mock, J. Y. Chin, T. J. Cui, and D. R. Smith, "Broadband ground-plane cloak," Science **323**, 366–369 (2009).
http://dx.doi.org/10.1126/science.1166949 (p. 107)

[116] J. Valentine, J. Li, T. Zentgraf, G. Bartal, and X. Zhang, "An optical cloak made of dielectrics," Nature Materials **8**, 568–571 (2009).
http://dx.doi.org/10.1038/nmat2461 (p. 107)

[117] J. H. Lee, J. Blair, V. A. Tamma, Q. Wu, S. J. Rhee, C. J. Summers, and W. Park, "Direct visualization of optical frequency invisibility cloak based on silicon nanorod array," Optics Express **17**, 12 922–12 928 (2009).
http://dx.doi.org/10.1364/OE.17.012922 (p. 107)

[118] H. F. Ma and T. J. Cui, "Three-dimensional broadband ground-plane cloak made of metamaterials," Nature Communications **1**, 21 (2010).
http://dx.doi.org/10.1038/ncomms1023 (p. 107)

[119] B. Zhang, Y. Luo, X. Liu, and G. Barbastathis, "Macroscopic invisibility cloak for visible light," Physical Review Letters **106**, 33 901 (2011).
http://dx.doi.org/10.1103/PhysRevLett.106.033901 (p. 107)

[120] X. Chen, Y. Luo, J. Zhang, K. Jiang, J. B. Pendry, and S. Zhang, "Macroscopic invisibility cloaking of visible light," Nature Communications **2**, 176 (2011).
http://dx.doi.org/10.1038/ncomms1176 (p. 107)

[121] S. G. Johnson and J. D. Joannopoulos, "Block-iterative frequency-domain methods for Maxwell's equations in a planewave basis," Optics Express **8**, 173–190 (2001). http://dx.doi.org/10.1364/OE.8.000173 (p. 108)

[122] W. Martienssen and E. Spiller, "Coherence and fluctuations in light beams," American Journal of Physics **32**, 919–926 (1964). http://dx.doi.org/10.1119/1.1970023 (p. 112)

[123] W. Martienssen and E. Spiller, "Intensity fluctuations in light beams with several degrees of freedom," Physical Review Letters **16**, 531–533 (1966). http://dx.doi.org/10.1103/PhysRevLett.16.531 (p. 112)

[124] B. Harke, P. Bianchini, F. Brandi, and A. Diaspro, "Photopolymerization inhibition dynamics for sub-diffraction direct laser writing lithography," ChemPhysChem **13**, 1429–1434 (2012). http://dx.doi.org/10.1002/cphc.201200006 (p. 120, 121)

Acknowledgments

At the end of this thesis, I want to thank all the people who enabled this work. I can state that the last 3.5 years were the most interesting ones in my life so far. I think that doing research on a novel (and potentially important) topic in a friendly and cooperative atmosphere is far from ordinary and I'm very grateful for this time.

First and most of all, I want to thank my supervisor Prof. Dr. Martin Wegener for giving me the opportunity to work on this exciting new topic in such a positive environment. He always shared my excitement about experimental news and brought in many new ideas. Yet, he gave me enough space to act on my own and supported all my ideas.

Next, I would like to acknowledge Prof. Dr. Kurt Busch for co-refereeing my thesis. Given the considerable spatial distance between Karlsruhe and his new professorship in Berlin, I especially appreciate this effort.

My special thanks go to Prof. Dr. Georg von Freymann. He already supervised me during my Diploma thesis and continued supervising me during the first part of my PhD thesis until he followed a call for a professorship in Kaiserslautern. Besides his practical and theoretical know-how in optics and software development, I really did appreciate his quick-mindedness in understanding and solving my problems.

I also want to express my gratitude to Tolga Ergin. We shared an office space, had many fruitful discussions and also a pleasant cooperation on the carpet cloak. Moreover, I thank Andreas Frölich for preparing ALD films and fruitful cooperation. Clemens Franz somehow accompanies me since the beginning of my Diploma thesis. In particular, I want to thank him and Andrea Scheiwe for their help on preparing the paint-brush pictures that preface all sections of this thesis.

During the last years, I had many fruitful discussions with virtually all members of the Wegener group. I want to especially thank Nils Feth, Fabian Niesler, Nicolas Stenger, and Michael Thiel at this point. Moreover, I want to thank all the proofreaders of this document, namely Tolga Ergin, Martin Husnik, Johannes Kaschke, Jonathan Müller, Andreas Schell, Andrea Scheiwe, Michael Thiel, Frank Wirner, and Thomas Wolf.

I am especially indebted to the institute's secretaries, to the mechanical workshops, and to the electronics workshop for doing all the things I can not do. I want to especially thank Werner Gilde, Renate Helfen, Heinz Hoffmann, Helmuth Lay, and Johann Westhauser.

In this last sentence, I want to thank my parents Gebhard and Irma, my sister Simone, my lovely girlfriend Andrea, and all my friends, that have supported me during my entire life and especially during the last months.

I thank you all.